HUMAN BRAIN WHITE MATTER ANALYSIS USING TRACTOGRAPHY —AN ATLAS-BASED APPROACH

by
Kegang Hua

A dissertation submitted to Johns Hopkins University in conformity with the requirements for the degree of Doctor of Philosophy

Baltimore, Maryland
March, 2013

Abstract

The human brain is connected via a vastly complex network of white matter fiber pathways. However, this structural connectivity information cannot be obtained from conventional MRI, in which much of white matter appears homogeneous. Diffusion tensor imaging can estimate fiber orientation by measuring the anisotropy of water diffusion. Using tractography, the brain connectivity can be studied non-invasively.

Past tractography studies have shown that the cores of prominent white matter tracts can be faithfully reconstructed. Superimposing the tract coordinates on various MR images, MR metrics can be quantified in a tract-specific manner. However, tractography results are often contaminated by partial volume effect and imaging noise. Particularly, tractography often fails under white matter pathological conditions, which render tract-specific analysis impractical.

In order to address these issues, we introduced an atlas-based approach. Four novel atlas-based approaches were included in this data analysis framework. First, statistical templates of major white matter tracts were created using a DTI database of normal subjects. The statistical white matter tract templates can serve two purposes. First, the statistical template can be used as a reference to detect abnormal white matter anatomy in neurodegenerative diseases. Second, the statistical template can be applied to individual patient data for automated white matter parcellation and tract-specific quantification.

In the second approach, the trajectory of white matter fiber bundles was used to estimate the cortical regions associated with specific tracts of interest. Using this approach, cortical regions were reproducibly identified on the population-averaged cortical maps of brain connectivity.

Third, we improved the accuracy of the population-based tract analysis by incorporating a highly elastic image transformation technique, called Large Deformation Diffeomorphic Metric Mapping (LDDMM). As a testament to the power of this algorithm, we successfully applied tract-specific analysis on Alzheimer's patients.

The last approach was to analyze the brain cortical connection networks using automatic fiber tracking. A tracking pipeline was built by combining White Matter Parcellation Map (WMPM), brute-force tractography and topology-preserving image transformation LDDMM. This novel tracking pipeline was applied on patient group with Alzheimer's disease. The connectivity networks of Alzheimer's patients were compared with age-matched controls using multivariate pattern classification.

Acknowledgements

I was very fortunate to have the privilege to work at Department of Radiology and Center for Imaging Science in the Johns Hopkins University. When I first started my work, I was excited to see the state-of-the-art MRI facilities in the imaging center and was impressed by the caliber of research at center for imaging science. Nevertheless, what I consider the most fortunate for me is that I had the opportunity to work with many brilliant people, who are highly-regarded experts in their respective fields. I consider many of them not only my mentors but also my inspirations. Indeed, without their unselfish help and contributions, this thesis work would not be possible.

First and foremost, I would like to extend my great gratitude to my advisors, Dr. Susumu Mori and Dr. Michael I. Miller. I feel grateful for their efforts and dedications for my research. I appreciate their willingness to share their vision and insight with me and allow me to pursue the subjects I am interested in. Specifically, I would like to thank Dr. Susumu and Dr. Miller for introducing me to the fascinating field of MR imaging and Computational Anatomy. I often benefit from their technical insights. I particularly want to thank Dr. Miller for his advices on my brain connectivity study.

I am also grateful for the scientific guidance and support from Dr. Mounya Elhilali, Dr. John I. Goutsias and Dr. Trac Tran. I appreciate their tutelage, especially their invaluable advices on signal processing and statistical learning. Furthermore, I thank Dr. Peter van zijl for his support for our atlas studies and serving on my GBO. I would also like to thank Dr. Carey Priebe for the discussion about feature selection and statistical learning algorithms.

I enjoy working with faculty members and my colleagues. I enjoy my collaborations with Dr. Tilak Ratnanather and Dr. Laurent Younes on several projects. I am grateful to Jiangyang

Zhang, Hao Huang, Rong Xue, and Dr. Chacko for teaching me how to operate MR scanners. I thank Kenichi Oishi, Andreia Faria, and Setsu Wakana for answering my questions about human brain anatomy without reservations. Also, I appreciate the help from Yajing, Zhipeng and Kazi on data processing and analysis.

Lastly, I would like to dedicate my dissertation to my parents, who have sustained me through the years. Without their unconditional love and support, I wouldn't have gone this far.

Table of Contents

List of Figures

List of Tables

Chapter 1

Introduction

1.1 Diffusion MRI

Beginning with the seminal work of Sir Peter Mansfield and Paul Lauterbur [1, 2], Magnetic Resonance Imaging (MRI) has brought many innovations into clinical medicine. The realization of Diffusion MR imaging in the late 1980s [3-5] is a cornerstone in MRI development. Non-invasive imaging of human brain structure networks is arguably the fairest fruit of this innovation [6].

The molecular diffusion, or Brownian motion of molecules, is a classic phenomenon [7]. The macroscopic diffusion that is originated from Brownian motion can be observed by simply pour small amount of dye into a beaker filled with water. The flux of diffusion between high concentration and low concentration regions is dictated by Fick's first law [8]:

$$\bar{\boldsymbol{J}} = -D\nabla C \tag{1.1}$$

where $\bar{\boldsymbol{J}}$ is flux density, D is the diffusion coefficient and ∇C is the concentration gradient. When the medium concentration is uniform, i.e. there is no macroscopic diffusion, the water molecule diffusion, originated from location $\overline{r_0}$, follows the Gaussian diffusion model and the root mean square of diffusion distance λ in time t can be described by Einstein's equation:

$$\lambda = |\overline{r_t} - \overline{r_0}| = \sqrt{6Dt} \tag{1.2}$$

where D is the diffusion coefficient and $\overline{r_t}$ is the new location at time t.

The effects of water diffusion on signals of magnetic resonance experiment were considered in the early days of NMR development [9-11]. These effects, which originally were

considered as confounding factors, were later used to measure water diffusion constant. NMR has since become the standard modality to measure diffusion non-invasively.

1.2 Magnetic Resonance Image Formation

If were subjected to an external static magnetic field B_0, the water protons, which possess an angular momentum of ½, will precess around the axis of B_0 at Larmor frequency:

$$f = \frac{\omega}{2\pi} = \frac{\gamma B_0}{2\pi} \tag{1.3}$$

where f is the Larmor frequency and γ is the gyromagnetic ratio.

In the presence of an external static magnetic field, water protons can have two quantum spin states, the "parallel" (low energy state) and the "anti-parallel" (high energy state) alignment to the applied magnetic field. Because the thermal energy associated with ambient temperature T is millions of times larger than the quantum energy difference between the two energy states, the number of water protons $\boldsymbol{N^+}$ in low energy state is only fractionally larger than the number of water protons $\boldsymbol{N^-}$ in high energy state [12]. And the ratio of these two populations is dictated by Boltzmann distribution:

$$\frac{\boldsymbol{N^-}}{\boldsymbol{N^+}} = \exp(\frac{\Delta E}{kT}) \tag{1.4}$$

where ΔE is the energy difference between the two state, k is Boltzmann constant and T is the absolute temperature.

Each proton can be regarded as a magnetic dipole. The excess in lower energy state dipoles leads to a net magnetization along the direction of the external static magnetic field. The magnetization can be tipped away from the equilibrium state by subjecting it to a radiofrequency

field applied perpendicular to the static magnetic field. The transverse component of the precessing magnetization can induce a voltage in a receiver coil [13-15].

In the absence of magnetic field gradient, the transverse component of the magnetization will decay with the transverse relaxation time constant T_2. This phenomenon is called Free Induction Decay (FID) and the signal $s(t)$ equation is:

$$s(t) = \int\int \rho(x,y) \cdot e^{-\frac{t}{T_2}} dxdy \tag{1.5}$$

where $\rho(x,y)$ denotes the water proton density. Sir Mansfield and Paul Lauterbur proposed [1, 2] that, by applying a magnetic field gradient to the static magnetic field, the magnetic dipoles will precess at different frequencies depending on their respective spatial locations. Thus, individual proton's location can be spatially encoded and the signal equation is:

$$s(t) = \int\int \rho(x,y) \cdot e^{-i\gamma x \int_0^t G_x(\tau)d\tau} \cdot e^{i\gamma y \int_0^t G_y(\tau)d\tau} \cdot e^{-\frac{t}{T_2}} dxdy \tag{1.6}$$

where G_x and G_y are gradients applied along x and y direction, respectively.

Define $k_x = \gamma \int_0^t G_x(\tau)d\tau$ and $k_y = \gamma \int_0^t G_y(\tau)d\tau$. The signal equation, ignoring the T_2 decay, is the Fourier transform of the proton density:

$$s(t) = \int\int \rho(x,y) \cdot e^{-i(k_x x + k_y y)} \cdot e^{-\frac{t}{T_2}} dxdy \tag{1.7}$$

Hence, by applying the inverse Fourier transform to the signal equation, an image of proton density can be reconstructed. The raw data space image is called k-space image [16, 17].

The MR proton imaging is now an essential imaging modality in clinical medicine. The human body contains 60% to 80% of water. This abundance in water, especially in the soft tissue, renders magnetic resonance imaging ideal for imaging human body. In fact, magnetic resonance

imaging (MRI) has superior soft-tissue contrast. Especially, it is sensitive to pathological conditions, such as neoplasm [18], which may otherwise be permeable to X-Ray and CT.

1.3 Diffusion MR Sequence Development

When Hahn first invented the spin echo sequence [9], he found that random motion of spins in a inhomogeneous magnetic field will lead to dispersion of phase and loss of signals. Carr and Purcell [10] studied the diffusion effects and started to use spin echo sequence to measure diffusion constant. However, their method requires a constant gradient to be presented at all times. This constant gradient interferes with the RF pulses and signal acquisition. The problem is exacerbated when the gradient must be increased to measure smaller and smaller diffusion constant. In 1965, Stejskal and Tanner [19, 20] introduced the Pulsed Gradient Spin Echo (PGSE) sequence. This sequence separates the diffusion time from the encoding time (the RF pulse duration) and the data acquisition time. The introduction of Stejskal-Tanner pulsed-gradient-spin-echo (PGSE) imaging sequence makes measurement of diffusion constant of complex biological samples practical.

In the 1980s, the diffusion encoding gradient was combined with MR imaging sequence [3-5] to acquire diffusion-weighted image (DWI), where diffusion constant, along any desired orientation, can be measured for every voxel. Although this endeavor sounds relatively simple, it was indeed a remarkable technological breakthrough in the MRI field.

The early diffusion MR imaging suffers from long scanning time and associated artifacts. The introduction of single-short echo-planar-imaging (EPI) [21-23] to measure intravoxel incoherent motion (IVIM) made the diffusion measurement practical for clinical applications [24]. In 1990, Moseley et al. [25] found that diffusion-weighted image is superior to other

modalities, such as T2-weighted image and CT, in detecting early stage of regional cerebral ischemia. Since the first few hours of stroke onset presents the greatest therapeutic opportunities [26, 27], diffusion weighted imaging has become the standard modality to monitor the early phase of ischemia and for treatment planning.

1.4 The Diffusion Measurement

The Stejskal-Tanner pulsed gradient spin-echo sequence (PGSE) as shown in Figure 1.1A consists of a pair of diffusion pulse gradients, one before and another after a 180° RF pulse. In the presence of a pulsed gradient, the water molecules would acquire a phase shift $\phi_1(x)$:

$$\phi_1(x_1) = \gamma \int_0^{\delta} G x_1 dt = \gamma G \delta x_1 \tag{1.8}$$

where G is gradient magnitude, δ is gradient duration, γ is the gyromagnetic ratio and x_1 is water molecule position along the gradient direction. The effect of 180° RF pulse is to invert the phase $\phi_1(x_1)$ to $-\phi_1(x_1)$.

Suppose after the onset of the first PGSE gradient pulse, second gradient pulse is applied at time Δ with the same duration δ and magnitude G. The water molecules would then acquire an additional phase shift $\phi_2(x)$:

$$\phi_2(x_2) = \gamma \int_0^{\delta} G x_2 dt = \gamma G \delta x_2 \tag{1.9}$$

Therefore, the net phase shift of water molecule $\Delta\phi$, after the two diffusion pulse gradient, is:

$$\Delta\phi = \big(-\phi_1(x_1)\big) + \phi_2(x_2) = -\gamma G \delta x_1 + \gamma G \delta x_2 \tag{1.10}$$

If there is no diffusion and the water molecule is static (i.e. $x_1 = x_2$), the net phase shift is $\Delta\phi = \gamma G \delta(-x_1 + x_2) = 0$.

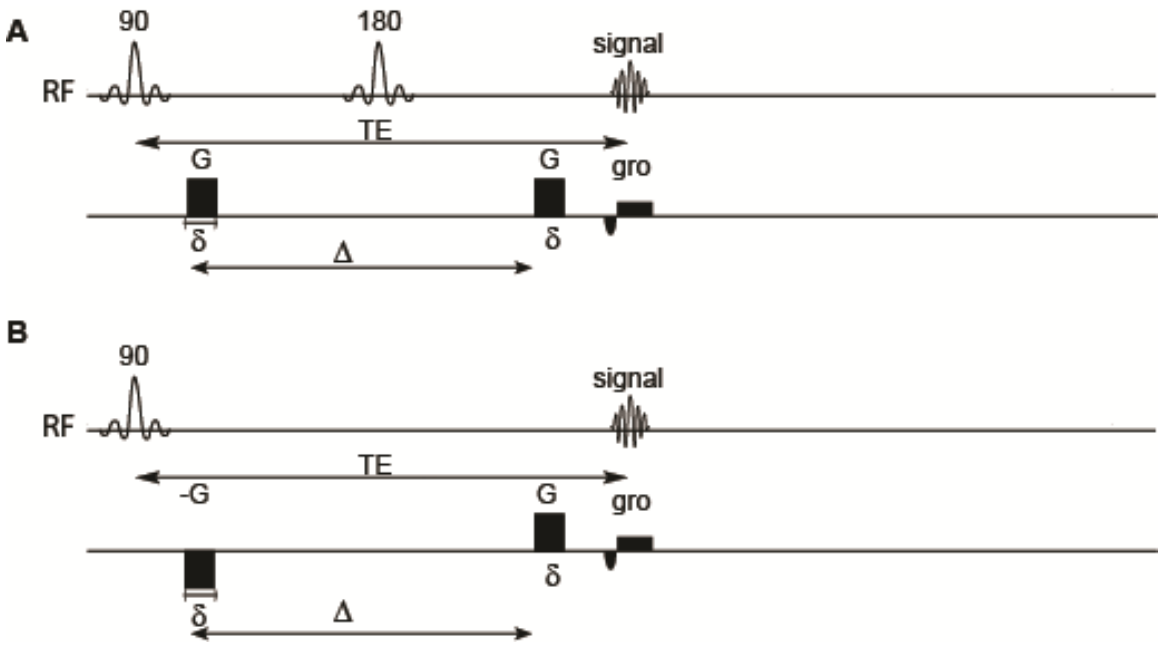

Figure 1.1: A) A modified Stejskal and Tanner pulsed-gradient spin-echo sequence for diffusion weighted imaging. B) A gradient echo sequence that is equivalent to the pulsed-gradient spin-echo sequence. For both sequences, $b = \gamma^2 G^2 \delta^2 \left(\Delta - \frac{\delta}{3}\right)$.

With self-diffusion, however, the root-mean-square (rms) of net phase shift is not zero. This non-zero root-mean-square phase shift can be described with a random walk model of diffusion [10, 28]. Suppose a water molecule, after undergo series of abrupt random discrete movement, jumps, along the gradient direction, from position x_0 to position x_N, the molecule movement can be expressed as following:

$$x_N = x_{N-1} + \alpha_N \xi = x_{N-2} + \alpha_{N-1}\xi + \alpha_N \xi = \cdots = x_0 + \xi \sum_{i=1}^{N} \alpha_i \qquad (1.11)$$

where ξ is the discrete distance that the water molecule abruptly jumped after stayed at previous position for time τ, and α_i is a random variable with value either $+1$ or -1.

Assuming the initial phase for the water molecule is zero, after time $t = N\tau$, i.e. N discrete random jumps in a time varying gradient field $G(t)$, the phase increment of the water molecule is:

$$\begin{aligned}\phi_N &= \gamma\tau\sum_{k=1}^{N}(G_k x_k) = \gamma\tau\xi\sum_{k=1}^{N}\left[G_k\left(\sum_{i=1}^{k}\alpha_i\right)\right] \\ &= \gamma\tau\xi\sum_{k=1}^{N}\left[\alpha_k\left(\sum_{i=k}^{N}G_i\right)\right]\end{aligned} \tag{1.12}$$

where G_k is the gradient at time $t = k\tau$. Therefore, for an ensemble of water molecules, supposing the mean phase shift is zero, the variance of the phase shift is:

$$\sigma_\phi^2(t = N\tau) = E[\phi_N^2] = \gamma^2\tau^2\xi^2 E\left\{\left[\sum_{k=1}^{N}\alpha_k\left(\sum_{i=k}^{N}G_i\right)\right]^2\right\} \tag{1.13}$$

Since α_k is the only random variable and can be either $+1$ or -1, and α_n and $\alpha_{\ m}$ are independent of each other, i.e. $E(\alpha_n\alpha_m) = 0$ for $n \neq m$ and $E(\alpha_n^2) = 1$ for all $n = 1,2,\dots,N$, the variance of phase shift can be written as:

$$\sigma_\phi^2(t = N\tau) = \gamma^2\tau^2\xi^2\sum_{k=1}^{N}\left(\sum_{i=k}^{N}G_i\right)^2 \tag{1.14}$$

For sufficiently small time interval τ, the equation can be written in the integral form:

$$\sigma_\phi^2(t = N\epsilon) = 2\gamma^2 D\int_0^t\left[\int_t^{t'}G(t'')dt''\right]^2 dt' \tag{1.15}$$

where $D = \frac{\xi^2}{2\tau}$.

Suppose diffusion is not restricted. The water molecule movement distribution is Gaussian and the phase shift is also Gaussian. The signal intensity is the integration of product of signal phase and the population distribution, i.e.:

$$S(t) = \int_{-\infty}^{\infty} S(0)\exp(i\phi) \times \frac{1}{\sqrt{2\pi\sigma_\phi^2}} \exp\left(-\frac{\phi^2}{2\sigma_\phi^2}\right) d\phi$$
$$= S(0)\exp\left[-\frac{\sigma_\phi^2(t)}{2}\right] \tag{1.16}$$

where $S(0)$ is the signal intensity without diffusion attenuation. Bringing the phase shift variance into above equation, we get the signal equation:

$$S(t) = S(0)\exp\left[-\gamma^2 D \int_0^t \left[\int_{t'}^t G(t'')dt''\right]^2 dt'\right] \tag{1.17}$$

As the effect of 180° pulse is to inverse the previous phase accumulation, which is equivalent to change the sign of the gradient following it, the pulsed gradient spin echo (PGSE) sequence is equivalent to a gradient-echo sequence with the 180° omitted and the sign of the gradient following it changed [29], as shown in Figure 1.1B. For this sequence, $\int_0^{t_e} G(t')dt' = 0$, where t_e is echo time. Hence, $\int_{t'}^{t_e} G(t'')dt'' = \int_{t'}^{0} G(t'')dt'' + \int_0^{t_e} G(t'')dt'' = -\int_0^{t'} G(t'')dt''$. Therefore, the relation between signal $S(t_e)$ at echo time and $S(0)$ can be written as [29]:

$$\ln\left[\frac{S(t_e)}{S(0)}\right] = -\gamma^2 D \int_0^{t_e} \left[\int_0^{t'} G(t'')dt''\right]^2 dt' \tag{1.18}$$

With some algebra, we can get the signal attenuation equation for the pulsed-gradient spin-echo (PGSE) sequence [19, 30]:

$$\ln\left[\frac{S(t_e)}{S(0)}\right] = -\gamma^2 G^2 \delta^2 \left(\Delta - \frac{\delta}{3}\right) D = -bD \tag{1.19}$$

where G and δ are the diffusion gradient strength and length, respectively, and Δ is the time interval between the two starting edges of the diffusion gradients. The new term b, where $b = \gamma^2 G^2 \delta^2 \left(\Delta - \frac{\delta}{3}\right)$, is the gradient factor [3, 31] and it describes the amount of diffusion

weighting. We can change b value by varying G, Δ or δ. High b value indicates more signal attenuation.

1.5 Diffusion Anisotropy in White Matter

Suppose water molecule is in a homogenous environment. The possibility that it will move in any direction is the same. Hence, water diffusion appears isotropic in unbounded homogenous spaces. Nevertheless, in biological systems, cellular and anatomical structures may be spatially ordered and can act as physical barriers to the random Brownian motion of water molecules. Since the physical barriers retard perpendicular movements of water molecules, the measured water diffusion coefficient may vary depending on the angle between measurement orientation and the surface norm of the physical barriers. Therefore, water diffusion in the restricted or hindered spaces is anisotropic and the measured diffusion coefficient in any predetermined direction is called apparent diffusion coefficient (ADC).

Early observations of anisotropic diffusion were made in bounded media and colloidal systems by Woessner [32], Stejskal and Tanner [20, 33], and Cotts [34], respectively. Cleveland [35] was the first to show anisotropic diffusion in biological samples. So far, anisotropic diffusion had been observed in many critical biological systems, e.g. muscle [35, 36], myocardium [37, 38], kidney [39], and brain white matter [40-43]. Among these, anisotropy in brain white matter was found to be the most prominent.

Until now, the origin of anisotropy in biological systems is still not fully understood. Two mechanisms could contribute to this phenomenon. First, water diffusion could be hindered by physical barriers, which may constitute cell membranes, subcellular organelles or myelin sheath.

Second, water molecules may partially bind to macromolecules or subcellular membrane such that their movements are restricted.

The effect of restricted diffusion can be observed by varying diffusion duration [32, 44-47]. If the diffusion duration is increased, water molecules will experience more and more physical barriers and the diffusion weighting will increase until an asymptotic value is reached. If the diffusion duration is decreased, less water molecules will reach the physical barriers and the diffusion weighting will decrease, until it is close to that of free diffusion.

Studies have suggested that, in the nervous systems, the axonal membrane and myelin sheath are the main structures responsible for water diffusion anisotropy [48, 49]. And the spatial ordering of these structures also plays an important role. Since the neuronal structures in human gray matter are randomly ordered, the water diffusion in this tissue appears isotropic as the restriction to water diffusion is approximately the same in every direction. On the other hand, the anisotropy observed in brain white matter can be ascribed to the ordered arrangement of myelinated fibers that act as physical barriers to water molecule movements.

The study of human brain white matter anisotropy is an extremely attractive field for brain researchers. As it is correlated with the arrangement and integrity of axonal membrane and myelin sheaths, diffusion anisotropy is expected to be more sensitive to white matter pathological changes than other modalities. So far, diffusion MRI is the only modality that can measure water anisotropy noninvasively within a clinically feasible time frame.

The relationships between water diffusion anisotropy and whiter matter structural alterations have been studied in several model systems, including ischemia, Wallerian degeneration and myelination/demylination.

Wallerian degeneration is the secondary white matter degeneration that occurs distal to the primary lesion. Water diffusion anisotropy was found significantly decreased on both primary lesion and distal sites [49, 50], which indicate a correlation between anisotropy variation and Wallerian degeneration.

The diffusion anisotropy is unchanged before and after induced ischemia [51] and sometimes was treated as a confounding factor in stroke studies [52]. However, anisotropy has proved to be useful in monitoring the temporal evolution of structural alteration after stroke [50, 53].

Anisotropy is also of much interest to the study of development and aging. Since the hypothesis is that myelin sheaths play a crucial role in the retardation of the water diffusion, it has postulated that the variation of anisotropy may reflect the myelination process during brain development [54]. It is expected that the study of anisotropy variation during development may facilitate the detection of early onset of neurological disease in infant. Furthermore, anisotropy also changes during aging and neurodegenerative disease. Anisotropy variation in the Alzheimer's disease is particularly of interest and was studied in this thesis work.

1.6 References

1. Lauterbur, P.C., *IMAGE FORMATION BY INDUCED LOCAL INTERACTIONS - EXAMPLES EMPLOYING NUCLEAR MAGNETIC-RESONANCE.* Nature, 1973. **242**(5394): p. 190-191.

2. Mansfield, P. and P.K. Grannell, *NMR DIFFRACTION IN SOLIDS.* Journal of Physics C-Solid State Physics, 1973. **6**(22): p. L422-L426.

3. Lebihan, D., et al., *MR IMAGING OF INTRAVOXEL INCOHERENT MOTIONS - APPLICATION TO DIFFUSION AND PERFUSION IN NEUROLOGIC DISORDERS.* Radiology, 1986. **161**(2): p. 401-407.

4. Taylor, D.G. and M.C. Bushell, *THE SPATIAL-MAPPING OF TRANSLATIONAL DIFFUSION-COEFFICIENTS BY THE NMR IMAGING TECHNIQUE.* Physics in Medicine and Biology, 1985. **30**(4): p. 345-349.

5. Merboldt, K.D., W. Hanicke, and J. Frahm, *SELF-DIFFUSION NMR IMAGING USING STIMULATED ECHOES.* Journal of Magnetic Resonance, 1985. **64**(3): p. 479-486.

6. Le Bihan, D. and H. Johansen-Berg, *Diffusion MRI at 25: Exploring brain tissue structure and function.* Neuroimage, 2012. **61**(2): p. 324-341.

7. Einstein, A., *The motion of elements suspended in static liquids as claimed in the molecular kinetic theory of heat.* Annalen Der Physik, 1905. **17**(8): p. 549-560.

8. Crank, J., *The mathematics of diffusion*. 2d ed. 1975, Oxford, Eng: Clarendon Press. viii, 414 p.

9. Hahn, E.L., *SPIN ECHOES.* Physical Review, 1950. **80**(4): p. 580-594.

10. Carr, H.Y. and E.M. Purcell, *EFFECTS OF DIFFUSION ON FREE PRECESSION IN NUCLEAR MAGNETIC RESONANCE EXPERIMENTS.* Physical Review, 1954. **94**(3): p. 630-638.

11. Torrey, H.C., *BLOCH EQUATIONS WITH DIFFUSION TERMS.* Physical Review, 1956. **104**(3): p. 563-565.

12. Haacke, E.M., *Magnetic resonance imaging : physical principles and sequence design*. 1999, New York: Wiley. xxvii, 914 p.

13. Bloch, F., *NUCLEAR INDUCTION.* Physical Review, 1946. **70**(7-8): p. 460-474.

14. Rabi, II, N.F. Ramsey, and J. Schwinger, *USE OF ROTATING COORDINATES IN MAGNETIC RESONANCE PROBLEMS.* Reviews of Modern Physics, 1954. **26**(2): p. 167-171.

15. Purcell, E.M., H.C. Torrey, and R.V. Pound, *RESONANCE ABSORPTION BY NUCLEAR MAGNETIC MOMENTS IN A SOLID.* Physical Review, 1946. **69**(1-2): p. 37-38.

16. Ljunggren, S., *A SIMPLE GRAPHICAL REPRESENTATION OF FOURIER-BASED IMAGING METHODS.* Journal of Magnetic Resonance, 1983. **54**(2): p. 338-343.

17. Twieg, D.B., *THE K-TRAJECTORY FORMULATION OF THE NMR IMAGING PROCESS WITH APPLICATIONS IN ANALYSIS AND SYNTHESIS OF IMAGING METHODS.* Medical Physics, 1983. **10**(5): p. 610-621.

18. Damadian, R., *TUMOR DETECTION BY NUCLEAR MAGNETIC RESONANCE.* Science, 1971. **171**(3976): p. 1151-&.

19. Stejskal, E.O. and J.E. Tanner, *SPIN DIFFUSION MEASUREMENTS: SPIN ECHOES IN THE PRESENCE OF A TIME-DEPENDENT FIELD GRADIENT.* Journal of Chemical Physics, 1965. **42**(1): p. 288-+.

20. Stejskal, E.O., *USE OF SPIN ECHOES IN A PULSED MAGNETIC-FIELD GRADIENT TO STUDY ANISOTROPIC RESTRICTED DIFFUSION AND FLOW.* Journal of Chemical Physics, 1965. **43**(10P1): p. 3597-&.

21. Mansfield, P., *MULTI-PLANAR IMAGE-FORMATION USING NMR SPIN ECHOES.* Journal of Physics C-Solid State Physics, 1977. **10**(3): p. L55-L58.

22. Mansfield, P., *REAL-TIME ECHO-PLANAR IMAGING BY NMR.* British Medical Bulletin, 1984. **40**(2): p. 187-&.

23. Rzedzian, R.R. and I.L. Pykett, *INSTANT IMAGES OF THE HUMAN-HEART USING A NEW, WHOLE-BODY MR IMAGING-SYSTEM.* American Journal of Roentgenology, 1987. **149**(2): p. 245-250.

24. Turner, R., et al., *ECHO-PLANAR IMAGING OF INTRAVOXEL INCOHERENT MOTION.* Radiology, 1990. **177**(2): p. 407-414.

25. Moseley, M.E., et al., *EARLY DETECTION OF REGIONAL CEREBRAL-ISCHEMIA IN CATS - COMPARISON OF DIFFUSION-WEIGHTED AND T2-WEIGHTED MRI AND SPECTROSCOPY.* Magnetic Resonance in Medicine, 1990. **14**(2): p. 330-346.

26. Baird, A.E. and S. Warach, *Magnetic resonance imaging of acute stroke.* Journal of Cerebral Blood Flow and Metabolism, 1998. **18**(6): p. 583-609.

27. Mintorovitch, J., et al., *COMPARISON OF DIFFUSION-WEIGHTED AND T2-WEIGHTED MRI FOR THE EARLY DETECTION OF CEREBRAL-ISCHEMIA AND REPERFUSION IN RATS.* Magnetic Resonance in Medicine, 1991. **18**(1): p. 39-50.

28. Ahn, C.B. and Z.H. Cho, *A GENERALIZED FORMULATION OF DIFFUSION EFFECTS IN MU-M RESOLUTION NUCLEAR MAGNETIC-RESONANCE IMAGING.* Medical Physics, 1989. **16**(1): p. 22-28.

29. Karlicek, R.F. and I.J. Lowe, *MODIFIED PULSED GRADIENT TECHNIQUE FOR MEASURING DIFFUSION IN THE PRESENCE OF LARGE BACKGROUND GRADIENTS.* Journal of Magnetic Resonance, 1980. **37**(1): p. 75-91.

30. Mori, S., *Introduction to diffusion tensor imaging*. 2006, Amsterdam ; Boston, MA: Elsevier.

31. Le Bihan, D., *Molecular diffusion nuclear magnetic resonance imaging.* Magnetic resonance quarterly, 1991. **7**(1): p. 1-30.

32. Woessner, D.E., *NMR SPIN-ECHO SELF-DIFFUSION MEASUREMENTS ON FLUIDS UNDERGOING RESTRICTED DIFFUSION.* Journal of Physical Chemistry, 1963. **67**(6): p. 1365-&.

33. Tanner, J.E. and E.O. Stejskal, *RESTRICTED SELF-DIFFUSION OF PROTONS IN COLLOIDAL SYSTEMS BY PULSED-GRADIENT SPIN-ECHO METHOD.* Journal of Chemical Physics, 1968. **49**(4): p. 1768-&.

34. Wayne, R.C. and R.M. Cotts, *NUCLEAR-MAGNETIC-RESONANCE STUDY OF SELF-DIFFUSION IN A BOUNDED MEDIUM.* Physical Review, 1966. **151**(1): p. 264-&.

35. Cleveland, G.G., et al., *NUCLEAR MAGNETIC-RESONANCE MEASUREMENT OF SKELETAL-MUSCLE - ANISOTROPY OF DIFFUSION-COEFFICIENT OF INTRACELLULAR WATER.* Biophysical Journal, 1976. **16**(9): p. 1043-1053.

36. Tanner, J.E., *SELF-DIFFUSION OF WATER IN FROG-MUSCLE.* Biophysical Journal, 1979. **28**(1): p. 107-116.

37. Garrido, L., et al., *ANISOTROPY OF WATER DIFFUSION IN THE MYOCARDIUM OF THE RAT.* Circulation Research, 1994. **74**(5): p. 789-793.

38. Reese, T.G., et al., *IMAGING MYOCARDIAL FIBER ARCHITECTURE IN-VIVO WITH MAGNETIC-RESONANCE.* Magnetic Resonance in Medicine, 1995. **34**(6): p. 786-791.

39. Henkelman, R.M., et al., *ANISOTROPY OF NMR PROPERTIES OF TISSUES.* Magnetic Resonance in Medicine, 1994. **32**(5): p. 592-601.

40. Chenevert, T.L., J.A. Brunberg, and J.G. Pipe, *ANISOTROPIC DIFFUSION IN HUMAN WHITE MATTER - DEMONSTRATION WITH MR TECHNIQUES INVIVO.* Radiology, 1990. **177**(2): p. 401-405.

41. Moseley, M.E., et al., *DIFFUSION-WEIGHTED MR IMAGING OF ANISOTROPIC WATER DIFFUSION IN CAT CENTRAL-NERVOUS-SYSTEM.* Radiology, 1990. **176**(2): p. 439-445.

42. Doran, M., et al., *NORMAL AND ABNORMAL WHITE MATTER TRACTS SHOWN BY MR IMAGING USING DIRECTIONAL DIFFUSION WEIGHTED SEQUENCES.* Journal of Computer Assisted Tomography, 1990. **14**(6): p. 865-873.

43. Moonen, C.T.W., et al., *RESTRICTED AND ANISOTROPIC DISPLACEMENT OF WATER IN HEALTHY CAT BRAIN AND IN STROKE STUDIED BY NMR DIFFUSION IMAGING.* Magnetic Resonance in Medicine, 1991. **19**(2): p. 327-332.

44. Beaulieu, C., *The basis of anisotropic water diffusion in the nervous system - a technical review.* Nmr in Biomedicine, 2002. **15**(7-8): p. 435-455.

45. Cooper, R.L., et al., *RESTRICTED DIFFUSION IN BIOPHYSICAL SYSTEMS - EXPERIMENT.* Biophysical Journal, 1974. **14**(3): p. 161-177.

46. Tanner, J.E., *TRANSIENT DIFFUSION IN A SYSTEM PARTITIONED BY PERMEABLE BARRIERS - APPLICATION TO NMR MEASUREMENTS WITH A PULSED FIELD GRADIENT.* Journal of Chemical Physics, 1978. **69**(4): p. 1748-1754.

47. Lebihan, D., R. Turner, and P. Douek, *IS WATER DIFFUSION RESTRICTED IN HUMAN BRAIN WHITE-MATTER - AN ECHO-PLANAR NMR IMAGING STUDY.* Neuroreport, 1993. **4**(7): p. 887-890.

48. Beaulieu, C. and P.S. Allen, *DETERMINANTS OF ANISOTROPIC WATER DIFFUSION IN NERVES.* Magnetic Resonance in Medicine, 1994. **31**(4): p. 394-400.

49. Beaulieu, C., et al., *Changes in water diffusion due to wallerian degeneration in peripheral nerve.* Magnetic Resonance in Medicine, 1996. **36**(4): p. 627-631.

50. Pierpaoli, C., et al., *Water diffusion changes in Wallerian degeneration and their dependence on white matter architecture.* Neuroimage, 2001. **13**(6): p. 1174-1185.

51. Vangelderen, P., et al., *WATER DIFFUSION AND ACUTE STROKE.* Magnetic Resonance in Medicine, 1994. **31**(2): p. 154-163.

52. Mori, S. and P.C.M. Vanzijl, *DIFFUSION WEIGHTING BY THE TRACE OF THE DIFFUSION TENSOR WITHIN A SINGLE SCAN.* Magnetic Resonance in Medicine, 1995. **33**(1): p. 41-52.

53. Werring, D.J., et al., *Diffusion tensor imaging can detect and quantify corticospinal tract degeneration after stroke.* Journal of Neurology Neurosurgery and Psychiatry, 2000. **69**(2): p. 269-272.

54. Neil, J., et al., *Diffusion tensor imaging of normal and injured developing human brain - a technical review.* Nmr in Biomedicine, 2002. **15**(7-8): p. 543-552.

Chapter 2

Diffusion Tensor Imaging and Tractography

2.1 Diffusion Tensor Imaging and Reconstruction

As shown in previous chapter, diffusion-weighted image measures diffusion coefficient on every voxel. This scalar diffusion coefficient is called apparent diffusion coefficient (ADC), as it reflects water diffusion along a predefined direction.

For anisotropic diffusion, the diffusion coefficient varies with measurement direction. Hence, a single scalar diffusion constant is not sufficient to characterize anisotropy diffusion. Several scalar indices were introduced [2-5]. These indices are mostly derived from diffusion weighted images (DWI) acquired in two or three independent directions. The main problem with these indices is that they are not independent of diffusion gradient orientations, i.e. their values vary with the body orientation with regards to the imaging hardware.

Basser et al. [6, 7] introduced effective diffusion tensor to depict anisotropic diffusion. The diffusion tensor is a 3×3 symmetric matrix that has nine elements [8]:

$$\boldsymbol{D} = \begin{bmatrix} D_{XX} & D_{XY} & D_{XZ} \\ D_{YX} & D_{YY} & D_{YZ} \\ D_{XZ} & D_{YZ} & D_{ZZ} \end{bmatrix} \tag{2.1}$$

The diagonal terms, D_{XX}, D_{YY}, D_{ZZ}, represent diffusion along the $x, y, and\ z$ directions, respectively, and the off-diagonal terms, $D_{XY}, D_{YX}, D_{YZ}, D_{XZ}, and\ D_{ZX}$, reflect correlations between water diffusion in orthogonal directions.

Using diffusion tensor, the signal attenuation equation for the pulsed-gradient spin-echo sequence (PGSE) can be written in following form [6, 8]:

$$\frac{S(TE)}{S_0} = \exp\left(-\gamma^2 \int_0^{TE} \left[\boldsymbol{F}(t') - 2H\left(t' - \frac{TE}{2}\right)\boldsymbol{f}\right]^{\boldsymbol{T}} \boldsymbol{D} \left[\boldsymbol{F}(t') - 2H\left(t' - \frac{TE}{2}\right)\boldsymbol{f}\right] dt'\right) \tag{2.2}$$

where $H(t')$ denotes the Heaviside function, and $\boldsymbol{f} = \boldsymbol{F}\left(\frac{TE}{2}\right)$, where

$$\boldsymbol{F}(t) = \int_0^t \boldsymbol{G}(t')dt' \tag{2.3}$$

and

$$\boldsymbol{G}(t) = \begin{bmatrix} G_x(t) \\ G_y(t) \\ G_z(t) \end{bmatrix} \tag{2.4}$$

If the diffusion gradient in PGSE sequence is rectangular and the interactions between imaging gradient and diffusion gradient are ignored, the above signal equation can be solved analytically:

$$\ln\left(\frac{S(TE)}{S_0}\right) = -\gamma^2\delta^2\left(\Delta - \frac{\delta}{3}\right)\sum_{i=X}^{Z}\sum_{j=X}^{Z} G_i D_{ij} G_j = -\sum_{i=X}^{Z}\sum_{j=X}^{Z} b_{ij} D_{ij} \tag{2.5}$$

where δ is the diffusion gradient length, Δ is the diffusion time between the leading edge of two diffusion gradients, and $b_{ij} = \gamma^2 G_i G_j \delta^2 \left[\Delta - \frac{\delta}{3}\right]$.

The matrix

$$\boldsymbol{b} = \begin{bmatrix} b_{XX} & b_{XY} & b_{XZ} \\ b_{XY} & b_{YY} & b_{YZ} \\ b_{XZ} & b_{YZ} & b_{ZZ} \end{bmatrix} \tag{2.6}$$

is called b matrix. For diffusion spectroscopy, where there is no imaging gradient, the elements of b matrix are determined by the scalar b value for PGSE sequence [9], i.e. $b_{ij} = \gamma^2 G_i G_j \delta^2 \left[\Delta - \frac{\delta}{3}\right]$. For diffusion tensor imaging [7], the interaction of the imaging sequence and the diffusion gradients cannot be ignored [10]. In that case, the b matrix

must be calculated using more dedicated programs for either analytical or numerical solutions [11-13].

Once the b matrix is determined, the signal attenuation is simply a sum of elements of diffusion tensor weighted by the elements of b matrix:

$$\ln\left(\frac{S(TE)}{S_0}\right) = -\sum_{j=X}^{Z}\sum_{i=X}^{Z} b_{ij}D_{ij} = -(b_{XX}D_{XX} + b_{YY}D_{YY} + b_{ZZ}D_{ZZ} + 2b_{XY}D_{XY} + 2b_{YZ}D_{YZ} + 2b_{XZ}D_{XZ}) \quad (2.7)$$

Since there are six unknown elements of diffusion tensor, at least seven images (one baseline image with minimum diffusion weighting and six diffusion weighted images acquired in six non-collinear directions) are required to solve the set of linear equations [14]. Using seven images, the exact solutions of six elements of diffusion tensor can be found. However, tensor reconstruction using only seven images is sensitive to systematic artifacts, such as motion and eddy current. In clinical practice, thirty or more images are acquired [15, 16] and multivariate linear regression is used to estimate the diffusion tensor [6, 17-19].

The diffusion tensor can be reconstructed using following simple linear model:

$$\boldsymbol{Y} = \boldsymbol{Hd} + \boldsymbol{\eta} \quad (2.8)$$

where $\boldsymbol{\eta}$ is noise and

$$\boldsymbol{Y} = \left[-\ln\left(\frac{S_1}{S_0}\right), -\ln\left(\frac{S_2}{S_0}\right), \ldots, -\ln\left(\frac{S_N}{S_0}\right)\right]^T \quad (2.9)$$

$$\boldsymbol{d} = [D_{XX}, D_{YY}, D_{ZZ}, D_{XY}, D_{XZ}, D_{YZ}]^T \quad (2.10$$

$$\boldsymbol{H} = \begin{pmatrix} g_{x1}^2 b_1 & g_{y1}^2 b_1 & g_{z1}^2 b_1 & 2g_{x1}g_{y1}b_1 & 2g_{x1}g_{z1}b_1 & 2g_{y1}g_{z1}b_1 \\ g_{x2}^2 b_2 & g_{y2}^2 b_2 & g_{z2}^2 b_2 & 2g_{x2}g_{y2}b_2 & 2g_{x2}g_{z2}b_2 & 2g_{y2}g_{z2}b_2 \\ \vdots & \vdots & \vdots & \vdots & \vdots & \vdots \\ g_{xN}^2 b_N & g_{yN}^2 b_N & g_{zN}^2 b_N & 2g_{xN}g_{yN}b_N & 2g_{xN}g_{zN}b_N & 2g_{yN}g_{zN}b_N \end{pmatrix} \quad (2.11$$

where $g_{xi}, g_{yi}\ and\ g_{zi}$ are normalized gradient components, $b_1, b_2, \dots, b_N$ are b values used for each respective diffusion image.

2.2 Anisotropic Indices and Diffusion Tensor Imaging Contrast

Diffusion tensor is a 3×3 symmetric matrix. The eigenvectors of this symmetric matrix represent three orthogonal directions along which the water diffusion is uncorrelated. The eigenvalues $\lambda_1, \lambda_2, \lambda_3$, where $\lambda_1 \geq \lambda_2 \geq \lambda_3$, are the diffusion constant along these three orthogonal directions, respectively. Since water diffusion displacement is always positive, the eigenvalues of diffusion tensor are real and positive. Hence, diffusion tensor is a positive semi-definite matrix [20].

Diffusion tensor has three principal scalar invariants that are defined as the following [21, 22]:

I. First Principal Invariant or Trace:

$$I_1 = D_{XX} + D_{YY} + D_{ZZ} = \lambda_1 + \lambda_2 + \lambda_3 \quad (2.12)$$

II. Second Principal Invariant:

$$I_2 = D_{XX}D_{YY} + D_{XX}D_{ZZ} + D_{YY}D_{ZZ} - D_{XY}D_{YX} - D_{XZ}D_{ZX} - D_{YZ}D_{ZY} = \lambda_1\lambda_2 + \lambda_1\lambda_3 + \lambda_2\lambda_3 \quad (2.13)$$

III. Third Principal Invariant or determinant:

$$I_3 = D_{XX}(D_{YY}D_{ZZ} - D_{ZY}D_{YZ}) - D_{XY}(D_{YX}D_{ZZ} - D_{ZX}D_{YZ}) + D_{XZ}(D_{YX}D_{ZY} - D_{ZX}D_{YY}) = \lambda_1\lambda_2\lambda_3 \quad (2.14)$$

There is also another often used invariant, which is called fourth invariant or square of tensor magnitude [23, 24].

IV. Fourth Invariant or square of tensor magnitude :

$$I_4 = I_1^2 - 2I_2 = D_{XX}^2 + D_{YY}^2 + D_{ZZ}^2 + 2D_{XY}D_{YX} + 2D_{XZ}D_{ZX} + 2D_{YZ}D_{ZY} = \lambda_1^2 + \lambda_2^2 + \lambda_3^2 \quad (2.15)$$

Basser et al. [23, 25] introduced several anisotropy indices that are derived directly from diffusion tensor. These anisotropy indices are defined using eigenvalues of diffusion tensor and are, therefore, rotationally invariant. Relative anisotropy (RA) and fractional anisotropy (FA) are two commonly used anisotropy indices. These two anisotropy indices can be defined using the four invariants of diffusion tensor [24, 26]. The relative anisotropy (RA) is defined as:

$$RA = \sqrt{2\left(1 - \frac{3\boldsymbol{I}_2}{\boldsymbol{I}_1^2}\right)} = \frac{\sqrt{(\lambda_1 - \lambda_2)^2 + (\lambda_2 - \lambda_3)^2 + (\lambda_1 - \lambda_3)^2}}{\lambda_1 + \lambda_2 + \lambda_3} = \frac{\sqrt{Var(\lambda)}}{\langle D \rangle} \quad (2.16)$$

where

$$\langle D \rangle = \frac{I_1}{3} = \frac{D_{XX} + D_{YY} + D_{ZZ}}{3} = \frac{\lambda_1 + \lambda_2 + \lambda_3}{3} \quad (2.17)$$

As shown in the equation, relative anisotropy is the ratio of variance of eigenvalues and the average of trace, which represent the anisotropic and isotropic part of diffusion tensor, respectively.

The fractional anisotropy (FA) is:

$$FA = \sqrt{1 - \frac{I_2}{I_4}} = \frac{\sqrt{(\lambda_1 - \lambda_2)^2 + (\lambda_2 - \lambda_3)^2 + (\lambda_1 - \lambda_3)^2}}{\sqrt{2}\sqrt{\lambda_1^2 + \lambda_2^2 + \lambda_3^2}} \quad (2.18)$$

The fractional anisotropy represents the fraction of "magnitude" of anisotropy part of diffusion tensor with respect to the "magnitude" of the whole tensor.

Both FA and RA are rotationally invariant and dimensionless. For isotropic diffusions, FA equals to zero. For anisotropic diffusion, where $\lambda_1 \gg \lambda_2 \approx \lambda_3$, FA value approaches one. Similarly, the RA value is often normalized to take values between zero and one. Comparison studies of these two indices have suggested that FA image has better signal to noise ratio (SNR) than RA images [27, 28]. Nowadays, FA images are used more frequently.

Figure 2.1 shows three diffusion tensor image contrasts. First image from the left

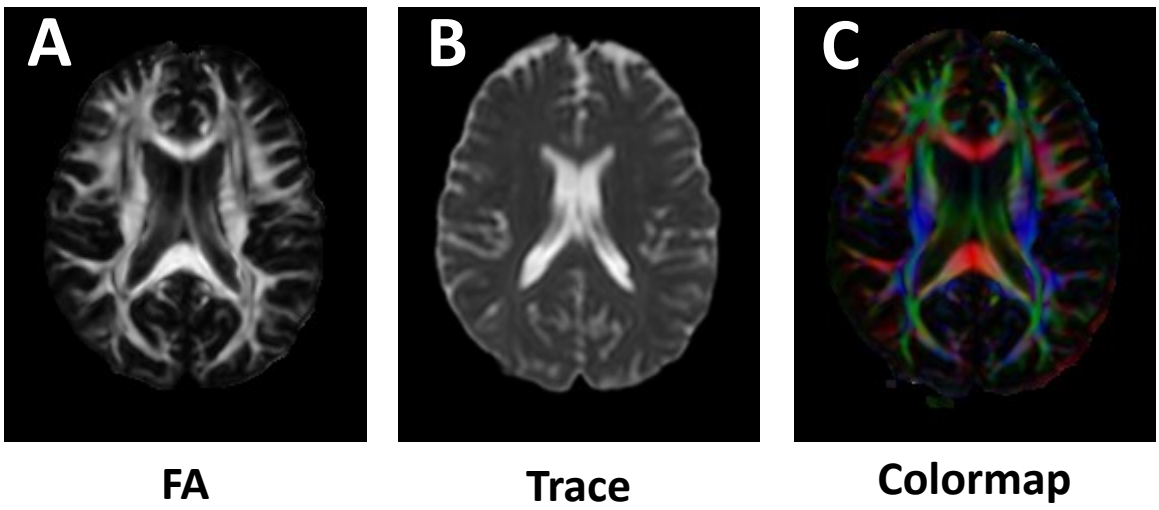

Figure 2.1: Diffusion Tensor Images. A) Fractional Anisotropy (FA) image. The areas with high intensity have high anisotropy. B) Trace image and the pixel value is $3 \times \langle D \rangle$, where $\langle D \rangle$ is the mean diffusivity. C) Direction encoded colormap. The red, blue, and green colors are representations of 3-D components of the eigenvector of diffusion tensor.

is the FA image, which represents the degree of anisotropy. White matter structures in the FA image have high intensity. The second image is the Trace image, where

$$TRACE = D_{XX} + D_{YY} + D_{ZZ} = \lambda_1 + \lambda_2 + \lambda_3 \tag{2.19}$$

Trace quantifies the isotropy part of diffusion tensor. Unlike FA, Trace value has a unit, e.g. mm^2/s. Trace image is used clinically for early detection of ischemia. The third image is color-coded image of principle eigenvector [29, 30]. In this image, the red, green, and blue color correspond to components of principle eigenvector in readout, phase encoding, and slice selection direction, respectively.

2.3 Tractography

Assuming the water diffusion is Gaussian, diffusion tensor is the covariance matrix of the Gaussian probability density function [5, 7]:

$$p(\boldsymbol{r}|\boldsymbol{r}_0, \boldsymbol{\tau}) = \frac{1}{\sqrt{(4\pi\tau)^3|\boldsymbol{D}|}} \exp\left[\frac{(\boldsymbol{r}-\boldsymbol{r_0})^{\boldsymbol{T}}\boldsymbol{D}^{-\mathbf{1}}(\boldsymbol{r}-\boldsymbol{r_0})}{4\tau}\right] \tag{2.20}$$

where $p(\boldsymbol{r}|\boldsymbol{r}_0, \tau)$ is the conditional probability that water molecules at position $\boldsymbol{r}_0$ will move to $\boldsymbol{r}$ after time τ.

The isosurface of Gaussian diffusion is an ellipsoid (see Figure 2.2). In human brain, this elongated ellipsoidal shape reflects that water molecules move more freely along the parallel direction to the fiber pathways than the perpendicular direction, and the longitudinal axis of the diffusion ellipsoid is parallel to the fiber direction. As diffusion tensor is the covariance matrix of the Gaussian probability density function, the eigenvector with the largest eigenvalue should coincide with the direction of the fiber bundle [2, 31, 32].

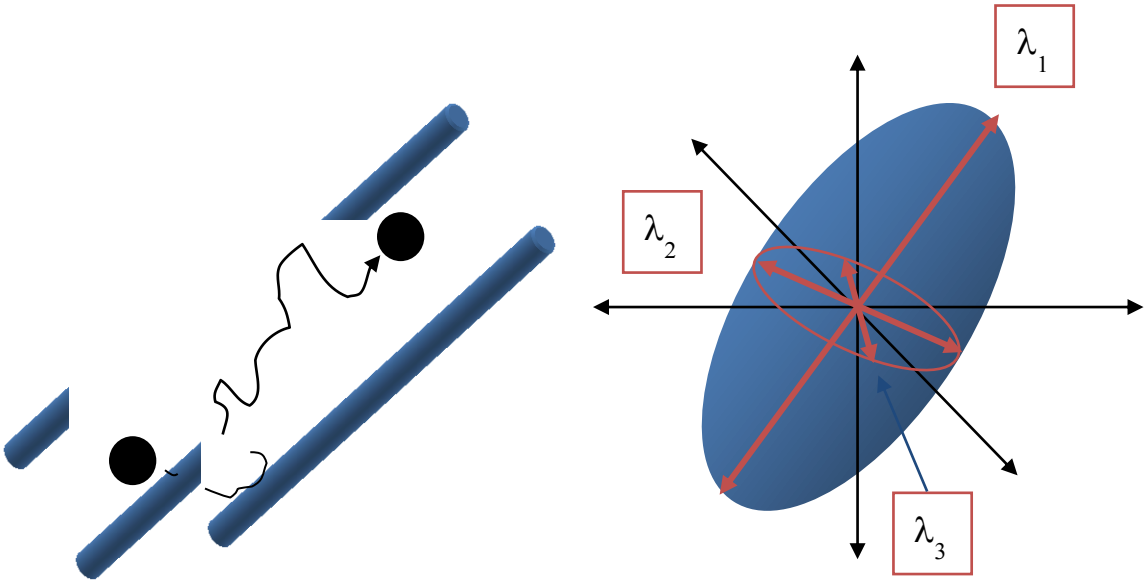

Figure 2.2: The tensor for anisotropic diffusion (Left) can be represented as an ellipsoid (Right). The longest axis of the ellipsoid, i.e. the eigenvector associated with the largest eigenvalue of the diffusion tensor, coincides with fiber direction.

Hence, diffusion tensor imaging provides a unique contrast for fiber direction. One novel application of this direction information is to non-invasively trace fiber pathways in-vivo [33-38]. Prior to diffusion tensor imaging, the fiber pathways are traced using either chemical tracer on animal samples or myelin stain on postmortem human brain [39, 40]. Both of these approaches are time consuming and invasive. They can't be applied on living human subjects.

Tractography is a technique to delineate neural fiber pathways using fiber direction information from diffusion-weighted images. As this technique is the only approach currently available to non-invasively study human brain structure connectivity, many efforts have been devoted to develop tractography algorithms [41].

The goal of tractography algorithm is to reproducibly delineate fiber connections in three-dimensional space. The eigenvectors of diffusion tensors in the white matter

constitute a 3-D vector field. Assuming these vectors' directions are indications of the fiber orientations, tractography algorithms must connect vectors in the 3-D vector field to reflect, as faithful as possible, the underline anatomical connectivity. One simple, yet very effective, algorithm developed for this purpose is linear line propagation method proposed by Mori et al.[33, 38].

Generally, there are two technical challenges for delineating fibers in three dimensional space. The first challenge is to convert discrete direction information to continuous fiber tracts in 3-D space. To track fiber pathways in 3-D, the most straightforward approach is to sequentially connect image voxels according to the vector orientations. However, this approach leads to tracking results with a zigzag pattern and, sometimes, deviating severely from the underline anatomy. Mori et. al.[33] employed a linear line-propagation approach, dubbed FACT (fiber assignment by continuous tractography), which propagates a line in the direction of the vectors in a continuous fashion. In this way, continuous fiber tracts are delineated in the discrete vector space.

The second technical challenge is the problem of crossing fibers. Intuitively, fiber tracking from one pixel of interest (POI) to another is to propagate a line, using FACT, from the first point to the second. However, because of the limited resolution of diffusion-weighted imaging, a single voxel could contain multiple populations of fiber pathways with each population heading towards different destination. Since the branching of fiber pathways is quite extensive in the human brain white matter, a simple propagation of a line from one pixel to another couldn't exhaustively delineate all the potential connections between the two points. This problem, however, can be mitigated by the so called brute force tracking [34, 42]. Namely, the brute force approach initiates

fiber tracking from all the voxels within the brain and only tracking results that pass through the two pixels of interest are kept.

Multiple pixels of interest or a region of interest (ROI) can be used to track bundles of fiber pathways. A tract of interest can be delineated using multiple ROIs [34, 42, 43] to include/exclude fibers. The sets of ROIs are usually defined based on prior anatomical knowledge. Using this multiple ROI approach, reproducible protocols have been established for several prominent white matter tracts [44-47].

2.4 Fiber Tracking Protocols

Many fiber tracking algorithms have been developed based on diffusion tensor imaging. These algorithms are currently divided into two groups. One group of approaches uses deterministic approach, such as FACT, to delineate fiber pathways. The other group of approaches employs statistical methods to estimate confidence levels of tracking results. Instead of showing streamlines in 3D, many approaches in this group assign probabilities or likelihood values to the voxels along possible connections.

a) Deterministic Fiber Tracking

In deterministic fiber tracking, tracking starts at the center of a seed voxel and the tracking line propagates along the maximum likelihood fiber directions. These directions are usually estimated using the principle eigenvector $\boldsymbol{e}_1$ of diffusion tensor. When the tracking line exits from one voxel and enters a neighboring voxel, the line continuous in the direction of eigenvector $\boldsymbol{e}_1$ of the new voxel. This tracking method is sometimes

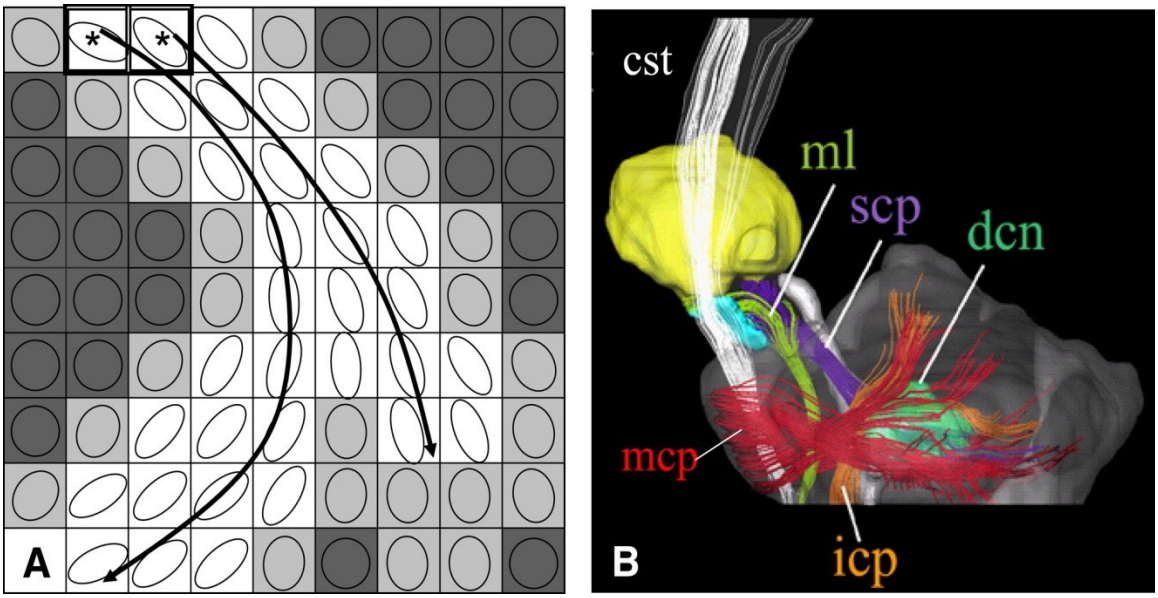

Figure 2.3 Illustration of deterministic fiber tracking algorithm (A) and example of tracking result in the human brain (B) [1].

called streamline tracking algorithm. An illustration of the deterministic tracking algorithm is shown in Fig. 2.3.

The stopping criteria for fiber tracking normally consist of curvature constraints and limits on the anisotropy. For example, we can stop fiber tracking when either the fiber turning angle is greater than 40° or FA value is less than 0.2 [48]. The fiber tracking can be initiated from all the voxels inside of the brain and multiple ROIs can be used to select fiber bundles.

Other streamline tracking methods include parametrized curve using Frenet equations [37] or linear state space models [49].

b) Probabilistic Fiber Tracking

Deterministic fiber tracking uses eigenvector of the diffusion tensor to estimate the fiber direction. However, the tracking result lacks information about the confidence level of the estimation.

Several studies have tried to put fiber tracking in a statistical framework. One statistical approach employed was the bootstrap method [50]. In this approach, subsets of diffusion measurements were randomly selected (with replacement) for multiple times. Fiber tracks were reconstructed on each dataset. Using statistics from these tracking results, probabilities were assigned to the voxels for possible connections. Regions with high probability were more consistent with known anatomy [50].

Similarly, Parker et. al. [51] employed Monte Carlo method to obtain the probability of anatomical connections, based on their model of fiber orientation distribution. Furthermore, Behrens et. al. [52, 53] used Bayesian theory to estimate multiple fiber populations. These probabilistic approaches can be used to study fiber connections in low anisotropy areas, such as thalamus [54].

2.5 Pitfalls and Limitations

The MR measurement of random motion is inherently sensitive to motion artifacts. Even very small motion artifacts such as cardiac pulsation can induce significant amount of phase shift in the diffusion-weighted images. Other factors, such as field inhomogeneity and hardware imperfections, can also affect the image quality [55, 56].

Innovative MR imaging techniques are developed/employed to ameliorate these artifacts [57, 58]. Nevertheless, more often than not, discernible imaging artifacts are presented in diffusion-weighted images. As diffusion tensors are reconstructed using

multiple diffusion-weighted images, caution has to be taken in the diffusion tensor reconstruction pipeline [59]. Visual inspection [48] or automatic outlier rejection [60] could improve the quality of tensor reconstruction.

Diffusion weighted imaging is an imaging modality that is often characterized with low SNR and low resolution. Severely low SNR could have detrimental effects on diffusion tensor reconstruction and anisotropic indices [61, 62]. The diffusion image resolution for clinical human brain scan is currently around 1-2mm, which is magnitude larger than the size of fiber fasciculus. Multiple fiber population could exist in the same voxel. Studies have shown that this fiber population inhomogeneity could result in reduction of the measured anisotropy [63, 64].

Fiber tracking is affected by these limitations of diffusion MR Imaging [65, 66]. First, the tracking results are sensitive to SNR. Huang et al.[66] studied the noise effect on tractography. They found that the number of fibers between two ROIs dropped precipitously when image SNR was too low. Secondly, crossing fiber and partial volume effect decrease voxel anisotropy, which increases the uncertainty of fiber estimation.

Besides many efforts to improve diffusion MR image quality, some other methods were introduced to improve the fiber resolution and tracking. Several groups have used probabilistic fiber tracking to estimate multiple fiber directions [50-52, 54]. Other groups have looked beyond the diffusion tensor model [67]. Among these efforts, the High Angular Resolution Diffusion Imaging (HARDI) method is briefly described below.

2.6 High Angular Resolution Diffusion Imaging (HARDI): The Promise and Challenges

Water diffusion can be described by a conditional probability $P(\boldsymbol{r_0}|\boldsymbol{r'}, \Delta)$, which is the probability that a water molecule, initially at position $\boldsymbol{r_0}$, will move to position $\boldsymbol{r'}$ after a time interval Δ [68, 69].

Consider the pulse-gradient spin echo experiment. Suppose δ is small such that the molecule displacement during this period can be ignored, the signal at echo time can be written as [70, 71]:

$$S(\boldsymbol{g}) = \int\int \rho(\boldsymbol{r_0}) P(\boldsymbol{r_0}|\boldsymbol{r'}, \Delta) \exp\big(\boldsymbol{i\gamma\delta g} \cdot (\boldsymbol{r'} - \boldsymbol{r_0})\big)\, \boldsymbol{dr'}\, d\boldsymbol{r_0} \tag{2.21}$$

where $\rho(\boldsymbol{r_0})$ is the prior probability of the molecule at position $\boldsymbol{r_0}$.

If we define $\boldsymbol{q} = \frac{1}{2\pi}\gamma\delta\boldsymbol{g}$, we can see there is a Fourier relationship between signal intensity and the displacement profile, i.e.

$$I(\boldsymbol{r}) = \mathcal{F}(S(\boldsymbol{q})) = \int \rho(\boldsymbol{r_0}) P(\boldsymbol{r_0}|\boldsymbol{r'}, \Delta) \tag{2.22}$$

where $\boldsymbol{r} = \boldsymbol{r'} - \boldsymbol{r_0}$ [71, 72]. Furthermore, if we also apply space encoding in k-space, the signal is modulated both in k-space and q-space [73, 74]

$$S(\boldsymbol{k}, \boldsymbol{q}) = \int \rho(\boldsymbol{r_0}) \exp(i2\pi\boldsymbol{k} \cdot \boldsymbol{r_0}) \int P(\boldsymbol{r_0}|\boldsymbol{r'}, \Delta) \exp\big(i2\pi\boldsymbol{q} \cdot (\boldsymbol{r'} - \boldsymbol{r_0})\big)\, d\boldsymbol{r'}\, d\boldsymbol{r_0} \tag{2.23}$$

Therefore, by acquiring diffusion MR images in both q-space and k-space, the diffusion displacement profile can be reconstructed for each voxel, without making any prior model assumptions [75].

There are, however, several limitations for the Q-space imaging. First, traversing both q-space and k-space is often too time-consuming to be practical. Alternative methods, such as using Q-Ball imaging to acquire q-space image on a sphere instead of on Cartesian grid [76] or using mixtures of Gaussian model [77], are possible ways to

reduce the scanning time. Second, the assumption for the signal equation is that δ is small. Yet, to achieve various degrees of diffusion attenuation, $\boldsymbol{q}$ value needs to be able to vary in a range of positions in q-space. Since δ has to be as small as possible, large $\boldsymbol{g}$ value is often required. However, for large $\boldsymbol{q}$ values, the required $\boldsymbol{g}$ value could go beyond the capability of the scanners. Thirdly, high diffusion attenuation is needed to differentiate multiple components in fiber populations [64]. However, SNR will drop with increasing diffusion attenuation [61]. In the end, the high angular diffusion weighted images often has worse SNR than diffusion tensor images.

These above mentioned caveats are among the reasons why it is currently difficult to introduce high angular imaging techniques to the clinical and research settings. Some advanced data processing strategies have been proposed [78]. It is currently a hot area in diffusion MR research.

All in all, although high angular and q-space imaging are still under development, they are believed to have great promise. For example, more detailed brain connectivity map is expected to be delineated by HARDI than that would by diffusion tensor imaging. Moreover, since high angular and q-space images are model free and only depend on the underline water diffusion distributions, they should be able to reveal wealth of information about physiological and pathological processes in the human brain.

2.7 Research and Clinical Applications of Diffusion Tensor Imaging and Tractography

Diffusion tensor imaging generates several new image contrasts for researchers and clinicians: Trace and FA images quantitatively measure the diffusion and anisotropy;

color map image encodes the orientation of white matter fiber tracks. Furthermore, it has been shown that the respective eigenvectors (the primary, secondary and tertiary eigenvectors) of diffusion tensor also reveal valuable information about the status of axon and myelin sheath [79, 80]. The respective applications for these new contrasts are briefly overviewed below.

a) Fractional Anisotropy as a new MR contrast to monitor myelination and axonal integrity

A number of anatomical and physiological events could lead to fractional anisotropy value change. For example, during early brain development, the white matter FA increases due to myelination and axon growth. Meanwhile, the gray matter FA contrast goes through a transition from high anisotropy to low anisotropy as the dendrite outgrowth destroys the coherence organization of axon in the cortex.

Demyelination and axonal damages will both decrease the fractional anisotropy significantly. Interestingly, there are evidences for two different mechanisms. Animal studies have suggested that demyelination often leads to increase in transverse diffusivity, while axonal injury often results in a decrease of the axial diffusivity [1, 80]. One explanation is that demyelination leads to less restriction on transverse diffusion and axonal injury leads to a disarray of axons that reduces the axial diffusion.

The variations in fractional anisotropy can be used as an indication of the status of neurological diseases. For example, Multiple Sclerosis (MS) is an inflammatory autoimmune disease that mainly affects the white matter. After an acute onset, the MS disease typically follows a relapsing-remitting disease course and the MS lesions can be

appreciated on T2-weighted image. Diffusion tensor imaging studies have shown that the fractional anisotropy is reduced on the lesion area. Particularly, when compared with the white matter in healthy controls, the normal appearing white matter (NAWI) between the lesion areas also showed lowered anisotropy [81, 82]. These findings suggests that diffusion tensor imaging not only can be used to monitor disease status, but also can reveal additional information about disease mechanisms.

Additionally, fractional anisotropy variations were observed in cerebral palsy [83, 84], HIV [85, 86], and Alzheimer's disease [87-90]. Anisotropy contrast was also observed on diffusion tensor image of premyelinated brains. This observation confirms our previous statement that anisotropy depends not only on myelination, but also on many other factors, such as axonal integrity. The conventional T1- and T2-weighted contrast depends heavily on myelination and they have poor contrast on premyelinated brains [1, 91, 92]. Therefore, fractional anisotropy can be a better and more consistent contrast to study the anatomy and development of immature brains.

b) Directional information as a powerful tool for white matter parcellation and tract-specific analysis

The color-coded fiber orientation image (the color map image) is a powerful tool to delineate fibers and locate intensity abnormality on white matter. First, white matter tract bundles can be readily appreciated on color maps. Based on this information, white matter can be parcellated into smaller anatomical unit. Tract volume can be measured by delineating the fiber boundaries on the color map images. Deformation of the fiber tracts, such as that caused by tumor growth, can be quantified.

Second, tractography groups 2D voxels of the same tract into 3D fiber bundles. Therefore, tractography can be used as an automatic 3-D parcellation tool. MR metrics, such as T1, T2, diffusion and MT transfer, can be quantified on the tract parcellation map created using tractography. Moreover, lesions with abnormal MR image intensity on white matter tracts can be identified using the parcellation map and the extent of the lesions can be quantified using tract-specific analysis.

c) Brain connectivity analysis using Tractography

An exciting application for diffusion tensor imaging is to investigate the brain connectivity using tractography. As we know, the brain is compartmented into modules. Each module is responsible for several different tasks. Nevertheless, these functional areas are interconnected by a network of white matter fiber pathways. Using tractography to reconstruct the structural connections in-vivo may shade light on how the information is relayed between different functional areas.

Several studies have used deterministic and probabilistic tractography to investigate cortico-cortical [42, 93, 94] and cortico-thalamic connectivity [54]. Good agreement with known anatomy was found. Furthermore, although considerable studies have suggested temporal correlations in spontaneous blood oxygen level-dependent (BOLD) signal, whether or not these correlations are indications of neural connectivity is still under debate. Combing the structural connectivity analysis with functional MRI can provide evidence for underline connectivity. One technical challenge of this approach is that the limited resolution of diffusion tensor imaging dictates that only large bundle of axons can be visualized. Therefore, the correspondences between structural and

functional connections are still elusive and we may rely on novel statistical analysis methods to elucidate the relationships [95-97].

Graph theory was recently introduced to characterize the brain structural networks [98-100]. These studies have found that the human brain cortical connectivity forms a small world network [101] and this network contains hub regions that connect all major structural modules. Significant correlation between structural and default network functional connectivity was also shown in several studies [96, 100, 102].

Recently, there are strong evidences suggesting that neurodegenerative diseases such as Alzheimer's affect brain functional hub regions and networks [103, 104]. An important question to ask is to what extent the neurodegenerative disease affects structural networks. Moreover, the studies of these disease models can give us more information about the relationship between functional networks and white matter connectivity networks. In this thesis work, we are going to explore these possibilities by reconstructing the white matter network using an atlas-based approach and comparing the brain networks of normal control and Alzheimer's patient using statistical learning algorithms. These studies not only could have significant scientific value, but may also have important therapeutic implications as well.

2.8 References

1. Mori, S. and J.Y. Zhang, *Principles of diffusion tensor imaging and its applications to basic neuroscience research.* Neuron, 2006. **51**(5): p. 527-539.

2. Moseley, M.E., et al., *DIFFUSION-WEIGHTED MR IMAGING OF ANISOTROPIC WATER DIFFUSION IN CAT CENTRAL-NERVOUS-SYSTEM.* Radiology, 1990. **176**(2): p. 439-445.

3. Douek, P., et al., *MR COLOR MAPPING OF MYELIN FIBER ORIENTATION.* Journal of Computer Assisted Tomography, 1991. **15**(6): p. 923-929.

4. Vangelderen, P., et al., *WATER DIFFUSION AND ACUTE STROKE.* Magnetic Resonance in Medicine, 1994. **31**(2): p. 154-163.

5. Basser, P.J., *Inferring microstructural features and the physiological state of tissues from diffusion-weighted images.* Nmr in Biomedicine, 1995. **8**(7-8): p. 333-344.

6. Basser, P.J., J. Mattiello, and D. Lebihan, *Estimation of the Effective Self-Diffusion Tensor from the Nmr Spin-Echo.* Journal of Magnetic Resonance Series B, 1994. **103**(3): p. 247-254.

7. Basser, P.J., J. Mattiello, and D. Lebihan, *Mr Diffusion Tensor Spectroscopy and Imaging.* Biophysical Journal, 1994. **66**(1): p. 259-267.

8. Stejskal, E.O., *USE OF SPIN ECHOES IN A PULSED MAGNETIC-FIELD GRADIENT TO STUDY ANISOTROPIC RESTRICTED DIFFUSION AND FLOW.* Journal of Chemical Physics, 1965. **43**(10P1): p. 3597-&.

9. Stejskal, E.O. and J.E. Tanner, *SPIN DIFFUSION MEASUREMENTS: SPIN ECHOES IN THE PRESENCE OF A TIME-DEPENDENT FIELD GRADIENT.* Journal of Chemical Physics, 1965. **42**(1): p. 288-+.

10. Neeman, M., J.P. Freyer, and L.O. Sillerud, *PULSED-GRADIENT SPIN-ECHO DIFFUSION STUDIES IN NMR IMAGING - EFFECTS OF THE IMAGING GRADIENTS ON THE DETERMINATION OF DIFFUSION-COEFFICIENTS.* Journal of Magnetic Resonance, 1990. **90**(2): p. 303-312.

11. Mattiello, J., P.J. Basser, and D. Lebihan, *ANALYTICAL EXPRESSIONS FOR THE B-MATRIX IN NMR DIFFUSION IMAGING AND SPECTROSCOPY.* Journal of Magnetic Resonance Series A, 1994. **108**(2): p. 131-141.

12. Le Bihan, D., *Diffusion and perfusion magnetic resonance imaging : applications to functional MRI.* 1995, New York: Raven Press. xxi, 374 p.

13. Mattiello, J., P.J. Basser, and D. LeBihan, *The b matrix in diffusion tensor echo-planar imaging.* Magnetic Resonance in Medicine, 1997. **37**(2): p. 292-300.

14. Basser, P.J. and C. Pierpaoli, *A simplified method to measure the diffusion tensor from seven MR images.* Magnetic Resonance in Medicine, 1998. **39**(6): p. 928-934.

15. Jones, D.K., M.A. Horsfield, and A. Simmons, *Optimal strategies for measuring diffusion in anisotropic systems by magnetic resonance imaging.* Magnetic Resonance in Medicine, 1999. **42**(3): p. 515-525.

16. Le Bihan, D., et al., *Diffusion tensor imaging: Concepts and applications.* Journal of Magnetic Resonance Imaging, 2001. **13**(4): p. 534-546.

17. Hasan, K.M., D.L. Parker, and A.L. Alexander, *Comparison of gradient encoding schemes for diffusion-tensor MRI.* Journal of Magnetic Resonance Imaging, 2001. **13**(5): p. 769-780.

18. Hasan, K.M. and P.A. Narayana, *Computation of the fractional anisotropy and mean diffusivity maps without tensor decoding and diagonalization: Theoretical analysis and validation.* Magnetic Resonance in Medicine, 2003. **50**(3): p. 589-598.

19. Kingsley, P.B., *Introduction to diffusion tensor imaging mathematics: Part III. Tensor calculation, noise, simulations, and optimization.* Concepts in Magnetic Resonance Part A, 2006. **28A**(2): p. 155-179.

20. Horn, R.A. and C.R. Johnson, *Matrix analysis*. 1985, Cambridge Cambridgeshire ; New York: Cambridge University Press. xiii, 561 p.

21. Kingsley, P.B., *Introduction to diffusion tensor imaging mathematics: Part I. Tensors, rotations, and eigenvectors.* Concepts in Magnetic Resonance Part A, 2006. **28A**(2): p. 101-122.

22. Lai, W.M., D. Rubin, and E. Krempl, *Introduction to continuum mechanics*. 4th ed. 2010, Amsterdam ; Boston: Butterworth-Heinemann/Elsevier. xiv, 520 p.

23. Basser, P.J. and C. Pierpaoli, *Microstructural and physiological features of tissues elucidated by quantitative-diffusion-tensor MRI.* Journal of Magnetic Resonance Series B, 1996. **111**(3): p. 209-219.

24. Ulug, A.M. and P.C.M. van Zijl, *Orientation-independent diffusion imaging without tensor diagonalization: Anisotropy definitions based on physical attributes of the diffusion ellipsoid.* Jmri-Journal of Magnetic Resonance Imaging, 1999. **9**(6): p. 804-813.

25. Pierpaoli, C. and P.J. Basser, *Toward a quantitative assessment of diffusion anisotropy.* Magnetic Resonance in Medicine, 1996. **36**(6): p. 893-906.

26. Kingsley, P.B., *Introduction to diffusion tensor imaging mathematics: Part II. Anisotropy, diffusion-weighting factors, and gradient encoding schemes.* Concepts in Magnetic Resonance Part A, 2006. **28A**(2): p. 123-154.

27. Papadakis, N.G., et al., *A study of rotationally invariant and symmetric indices of diffusion anisotropy.* Magnetic Resonance Imaging, 1999. **17**(6): p. 881-892.

28. Hasan, K.M., A.L. Alexander, and P.A. Narayana, *Does fractional anisotropy have better noise immunity characteristics than relative anisotropy in diffusion tensor MRI? An analytical approach.* Magnetic Resonance in Medicine, 2004. **51**(2): p. 413-417.

29. Pajevic, S. and C. Pierpaoli, *Color schemes to represent the orientation of anisotropic tissues from diffusion tensor data: Application to white matter fiber tract mapping in the human brain.* Magnetic Resonance in Medicine, 1999. **42**(3): p. 526-540.

30. Mori, S., *Introduction to diffusion tensor imaging*. 2006, Amsterdam ; Boston, MA: Elsevier.

31. Pierpaoli, C., et al., *Diffusion tensor MR imaging of the human brain.* Radiology, 1996. **201**(3): p. 637-648.

32. Doran, M., et al., *NORMAL AND ABNORMAL WHITE MATTER TRACTS SHOWN BY MR IMAGING USING DIRECTIONAL DIFFUSION WEIGHTED SEQUENCES.* Journal of Computer Assisted Tomography, 1990. **14**(6): p. 865-873.

33. Mori, S., et al., *Three-dimensional tracking of axonal projections in the brain by magnetic resonance imaging.* Annals of Neurology, 1999. **45**(2): p. 265-269.

34. Conturo, T.E., et al., *Tracking neuronal fiber pathways in the living human brain.* Proceedings of the National Academy of Sciences of the United States of America, 1999. **96**(18): p. 10422-10427.

35. Mori, S., et al., *In vivo visualization of human neural pathways by magnetic resonance imaging.* Annals of Neurology, 2000. **47**(3): p. 412-414.

36. Poupon, C., et al., *Regularization of diffusion-based direction maps for the tracking of brain white matter fascicles.* Neuroimage, 2000. **12**(2): p. 184-195.

37. Basser, P.J., et al., *In vivo fiber tractography using DT-MRI data.* Magnetic Resonance in Medicine, 2000. **44**(4): p. 625-632.

38. Xue, R., et al., *In vivo three-dimensional reconstruction of rat brain axonal projections by diffusion tensor imaging.* Magnetic Resonance in Medicine, 1999. **42**(6): p. 1123-1127.

39. Crick, F. and E. Jones, *BACKWARDNESS OF HUMAN NEUROANATOMY.* Nature, 1993. **361**(6408): p. 109-110.

40. Schmahmann, J.D. and D.N. Pandya, *Fiber pathways of the brain*. 2006, Oxford ; New York: Oxford University Press. xviii, 654 p.

41. Mori, S. and P.C.M. van Zijl, *Fiber tracking: principles and strategies - a technical review.* Nmr in Biomedicine, 2002. **15**(7-8): p. 468-480.

42. Stieltjes, B., et al., *Diffusion tensor imaging and axonal tracking in the human brainstem.* Neuroimage, 2001. **14**(3): p. 723-735.

43. Mori, S., et al., *Imaging cortical association using diffusion-tensor-based tracts in the human brain axonal tracking.* Magnetic Resonance in Medicine, 2002. **47**(2): p. 215-223.

44. Wakana, S., et al., *Fiber tract-based atlas of human white matter anatomy.* Radiology, 2004. **230**(1): p. 77-87.

45. Wakana, S., et al., *Reproducibility of quantitative tractography methods applied to cerebral white matter.* Neuroimage, 2007. **36**(3): p. 630-44.

46. Jellison, B.J., et al., *Diffusion tensor imaging of cerebral white matter: A pictorial review of physics, fiber tract anatomy, and tumor imaging patterns.* American Journal of Neuroradiology, 2004. **25**(3): p. 356-369.

47. Catani, M., et al., *Virtual in vivo interactive dissection of white matter fasciculi in the human brain.* Neuroimage, 2002. **17**(1): p. 77-94.

48. Jiang, H.Y., et al., *DtiStudio: Resource program for diffusion tensor computation and fiber bundle tracking.* Computer Methods and Programs in Biomedicine, 2006. **81**(2): p. 106-116.

49. Gossl, C., et al., *Fiber tracking from DTI using linear state space models: Detectability of the pyramidal tract.* Neuroimage, 2002. **16**(2): p. 378-388.

50. Jones, D.K. and C. Pierpaoli, *Confidence mapping in diffusion tensor magnetic resonance imaging tractography using a bootstrap approach.* Magnetic Resonance in Medicine, 2005. **53**(5): p. 1143-1149.

51. Parker, G.J.M., H.A. Haroon, and C.A.M. Wheeler-Kingshott, *A framework for a streamline-based probabilistic index of connectivity (PICo) using a structural interpretation of MRI diffusion measurements.* Journal of Magnetic Resonance Imaging, 2003. **18**(2): p. 242-254.

52. Behrens, T.E.J., et al., *Characterization and propagation of uncertainty in diffusion-weighted MR imaging.* Magnetic Resonance in Medicine, 2003. **50**(5): p. 1077-1088.

53. Behrens, T.E.J., et al., *Probabilistic diffusion tractography with multiple fibre orientations: What can we gain?* Neuroimage, 2007. **34**(1): p. 144-155.

54. Behrens, T.E., et al., *Non-invasive mapping of connections between human thalamus and cortex using diffusion imaging.* Nat Neurosci, 2003. **6**(7): p. 750-7.

55. Basser, P.J. and D.K. Jones, *Diffusion-tensor MRI: theory, experimental design and data analysis - a technical review.* Nmr in Biomedicine, 2002. **15**(7-8): p. 456-467.

56. Le Bihan, D., et al., *Artifacts and pitfalls in diffusion MRI.* Journal of Magnetic Resonance Imaging, 2006. **24**(3): p. 478-488.

57. Pruessmann, K.P., et al., *SENSE: Sensitivity encoding for fast MRI.* Magnetic Resonance in Medicine, 1999. **42**(5): p. 952-962.

58. Reese, T.G., et al., *Reduction of eddy-current-induced distortion in diffusion MRI using a twice-refocused spin echo.* Magnetic Resonance in Medicine, 2003. **49**(1): p. 177-182.

59. Jones, D.K. and M. Cercignani, *Twenty-five Pitfalls in the Analysis of Diffusion MRI Data.* Nmr in Biomedicine, 2010. **23**(7): p. 803-820.

60. Chang, L.C., D.K. Jones, and C. Pierpaoli, *RESTORE: Robust estimation of tensors by outlier rejection.* Magnetic Resonance in Medicine, 2005. **53**(5): p. 1088-1095.

61. Jones, D.K. and P.J. Basser, *"Squashing peanuts and smashing pumpkins": How noise distorts diffusion-weighted MR data.* Magnetic Resonance in Medicine, 2004. **52**(5): p. 979-993.

62. Dietrich, O., S. Heiland, and K. Sartor, *Noise correction for the exact determination of apparent diffusion coefficients at low SNR.* Magnetic Resonance in Medicine, 2001. **45**(3): p. 448-453.

63. Alexander, A.L., et al., *Analysis of partial volume effects in diffusion-tensor MRI.* Magnetic Resonance in Medicine, 2001. **45**(5): p. 770-780.

64. Frank, L.R., *Anisotropy in high angular resolution diffusion-weighted MRI.* Magnetic Resonance in Medicine, 2001. **45**(6): p. 935-939.

65. Lori, N.F., et al., *Diffusion tensor fiber tracking of human brain connectivity: aquisition methods, reliability analysis and biological results.* NMR in biomedicine, 2002. **15**(7-8): p. 494-515.

66. Huang, H., et al., *Analysis of noise effects on DTI-based tractography using the brute-force and multi-ROI approach.* Magnetic Resonance in Medicine, 2004. **52**(3): p. 559-565.

67. Tournier, J.D., S. Mori, and A. Leemans, *Diffusion Tensor Imaging and Beyond.* Magnetic Resonance in Medicine, 2011. **65**(6): p. 1532-1556.

68. Karger, J. and W. Heink, *THE PROPAGATOR REPRESENTATION OF MOLECULAR-TRANSPORT IN MICROPOROUS CRYSTALLITES.* Journal of Magnetic Resonance, 1983. **51**(1): p. 1-7.

69. Cory, D.G. and A.N. Garroway, *MEASUREMENT OF TRANSLATIONAL DISPLACEMENT PROBABILITIES BY NMR - AN INDICATOR OF COMPARTMENTATION.* Magnetic Resonance in Medicine, 1990. **14**(3): p. 435-444.

70. Tanner, J.E. and E.O. Stejskal, *RESTRICTED SELF-DIFFUSION OF PROTONS IN COLLOIDAL SYSTEMS BY PULSED-GRADIENT SPIN-ECHO METHOD.* Journal of Chemical Physics, 1968. **49**(4): p. 1768-&.

71. Callaghan, P.T., et al., *HIGH-RESOLUTION Q-SPACE IMAGING IN POROUS STRUCTURES.* Journal of Magnetic Resonance, 1990. **90**(1): p. 177-182.

72. King, M.D., et al., *Q-SPACE IMAGING OF THE BRAIN.* Magnetic Resonance in Medicine, 1994. **32**(6): p. 707-713.

73. Callaghan, P.T., C.D. Eccles, and Y. Xia, *NMR MICROSCOPY OF DYNAMIC DISPLACEMENTS - K-SPACE AND Q-SPACE IMAGING.* Journal of Physics E-Scientific Instruments, 1988. **21**(8): p. 820-822.

74. Callaghan, P.T., *Principles of nuclear magnetic resonance microscopy*. 1991, Oxford England, New York: Clarendon Press ; Oxford University Press. xvii, 492 p.

75. Wedeen, V.J., et al., *Mapping complex tissue architecture with diffusion spectrum magnetic resonance imaging.* Magnetic Resonance in Medicine, 2005. **54**(6): p. 1377-1386.

76. Tuch, D.S., *Q-Ball imaging.* Magnetic Resonance in Medicine, 2004. **52**(6): p. 1358-1372.

77. Tuch, D.S., et al., *High angular resolution diffusion imaging reveals intravoxel white matter fiber heterogeneity.* Magnetic Resonance in Medicine, 2002. **48**(4): p. 577-582.

78. Tournier, J.D., et al., *Direct estimation of the fiber orientation density function from diffusion-weighted MRI data using spherical deconvolution.* Neuroimage, 2004. **23**(3): p. 1176-1185.

79. Zhang, J.Y., P.C.M. van Zijl, and S. Mori, *Image contrast using the secondary and tertiary eigenvectors in diffusion teinsor imaging.* Magnetic Resonance in Medicine, 2006. **55**(2): p. 439-449.

80. Song, S.K., et al., *Dysmyelination revealed through MRI as increased radial (but unchanged axial) diffusion of water.* Neuroimage, 2002. **17**(3): p. 1429-1436.

81. Horsfield, M.A. and D.K. Jones, *Applications of diffusion-weighted and diffusion tensor MRI to white matter diseases - a review.* Nmr in Biomedicine, 2002. **15**(7-8): p. 570-577.

82. Miller, D.H., A.J. Thompson, and M. Filippi, *Magnetic resonance studies of abnormalities in the normal appearing white matter and grey matter in multiple sclerosis.* Journal of Neurology, 2003. **250**(12): p. 1407-1419.

83. Faria, A.V., et al., *Quantitative analysis of brain pathology based on MRI and brain atlases-Applications for cerebral palsy.* Neuroimage, 2011. **54**(3): p. 1854-1861.

84. Thomas, B., et al., *Quantitative diffusion tensor imaging in cerebral palsy due to periventricular white matter injury.* Brain, 2005. **128**: p. 2562-2577.

85. Filippi, C.G., et al., *Diffusion tensor imaging of patients with HIV and normal-appearing white matter on MR images of the brain.* American Journal of Neuroradiology, 2001. **22**(2): p. 277-283.

86. Pomara, N., et al., *White matter abnormalities in HIV-1 infection: A diffusion tensor imaging study.* Psychiatry Research-Neuroimaging, 2001. **106**(1): p. 15-24.

87. Oishi, K., et al., *The Fornix Sign: A Potential Sign for Alzheimer's Disease Based on Diffusion Tensor Imaging.* Journal of Neuroimaging, 2012. **22**(4): p. 365-374.

88. Zhang, Y., et al., *Diffusion tensor imaging of cingulum fibers in mild cognitive impairment and Alzheimer disease.* Neurology, 2007. **68**(1): p. 13-19.

89. Bozzali, M., et al., *White matter damage in Alzheimer's disease assessed in vivo using diffusion tensor magnetic resonance imaging.* Journal of Neurology Neurosurgery and Psychiatry, 2002. **72**(6): p. 742-746.

90. Medina, D., et al., *White matter changes in mild cognitive impairment and AD: A diffusion tensor imaging study.* Neurobiology of Aging, 2006. **27**(5): p. 663-672.

91. Maas, L.C., et al., *Early laminar organization of the human cerebrum demonstrated with diffusion tensor imaging in extremely premature infants.* Neuroimage, 2004. **22**(3): p. 1134-1140.

92. Hermoye, L., et al., *Pediatric diffusion tensor imaging: Normal database and observation of the white matter maturation in early childhood.* Neuroimage, 2006. **29**(2): p. 493-504.

93. Hagmann, P., et al., *DTI mapping of human brain connectivity: statistical fibre tracking and virtual dissection.* Neuroimage, 2003. **19**(3): p. 545-554.

94. Lazar, M. and A.L. Alexander, *Bootstrap white matter tractography (BOOT-TRAC).* Neuroimage, 2005. **24**(2): p. 524-532.

95. Koch, M.A., D.G. Norris, and M. Hund-Georgiadis, *An investigation of functional and anatomical connectivity using magnetic resonance imaging.* Neuroimage, 2002. **16**(1): p. 241-250.

96. Honey, C.J., et al., *Predicting human resting-state functional connectivity from structural connectivity.* Proceedings of the National Academy of Sciences of the United States of America, 2009. **106**(6): p. 2035-2040.

97. Greicius, M.D., et al., *Resting-State Functional Connectivity Reflects Structural Connectivity in the Default Mode Network.* Cerebral Cortex, 2009. **19**(1): p. 72-78.

98. Sporns, O., et al., *Organization, development and function of complex brain networks.* Trends in Cognitive Sciences, 2004. **8**(9): p. 418-425.

99. Hagmann, P., et al., *Mapping Human Whole-Brain Structural Networks with Diffusion MRI.* PLoS One, 2007. **2**(7).

100. Hagmann, P., et al., *Mapping the structural core of human cerebral cortex.* PLoS Biol, 2008. **6**(7): p. e159.

101. Watts, D.J. and S.H. Strogatz, *Collective dynamics of 'small-world' networks.* Nature, 1998. **393**(6684): p. 440-2.

102. Honey, C.J., J.P. Thivierge, and O. Sporns, *Can structure predict function in the human brain?* Neuroimage, 2010. **52**(3): p. 766-776.

103. Buckner, R.L., et al., *Cortical hubs revealed by intrinsic functional connectivity: mapping, assessment of stability, and relation to Alzheimer's disease.* J Neurosci, 2009. **29**(6): p. 1860-73.

104. Seeley, W.W., et al., *Neurodegenerative diseases target large-scale human brain networks.* Neuron, 2009. **62**(1): p. 42-52.

Chapter 3

Atlas-Based Approaches in Neuroinformatics

3.1 Atlases in Neuroinformatics

Atlas-based method has long history and widespread applications in neuroscience research. In histology studies, histology sections are often superimposed on annotated anatomical atlas to obtain important biological knowledge, e.g. patterns of gene expression. Dr. Paxinos' rat brain atlas is a popular reference for this purpose [1]. This book remains one of the most cited books in scientific research.

The first whole human brain atlas was introduced by Talairach, in order to guide deep-brain stereotactic procedures [2]. This atlas can also facilitate the estimation of functional activation foci [3]. However, for modern atlas-based analysis, the Talairach atlas has few drawbacks. First, it is a printed atlas that is based on sections from a single 60 years female. Second, the left and right asymmetry of the human brain is ignored in this atlas.

In last two decades, neuroimaging technology and computational methods had evolved tremendously. Several new whole brain atlases, such as MNI305 [4] and MNI152 [5], are now available [6]. These atlases are different from the Talairach atlas in several aspects. First, they are digitized atlases constructed using advanced neuroimaging modalities. Second, most of the atlases are population averaged such that each atlas can represent a particular population, e.g. normal young adults.

The MNI305 atlas was created at the Montreal Neurological Institute. They constructed this atlas in two steps [4, 7]. In the first step, various landmarks were defined on the Talairach atlas. The corresponding anatomical landmarks on subject image were

fitted together such that the resultant Anterior Commissure (AC)-Posterior Commissure (PC) line approximates that in the original Talairach atlas. This landmark transformation was applied on subject images and the transformed images were intensity normalized and averaged to generate the initial template. In the second step, the native subject image was mapped to the initial template using the transformation matrix obtained by maximizing the feature cross-correlation function. 305 MRI volumes were transformed and averaged to create the MNI305 atlas, which is the first atlas in MNI space.

Additionally, Colin Holmes at Montreal Neurological Institute scanned himself multiple times. Using 27 high resolution T1 images, a single subject atlas, Colin27 atlas, was created in the MNI space [8]. Compared with the MNI305 atlas, this single subject atlas has higher SNR and higher structure definition. However, like that of the Tailariach atlas, the limitation of the Colin27 atlas is that it doesn't take into account the anatomical variability of individuals.

Around year 2000, the International Consortium for Brain Mapping (ICBM) initiated a collaborative effort to create an atlas in the MNI space with advanced imaging technologies [5, 9]. Three renowned institutes, UCLA, MNI and UTHSCSA participated in this effort. Each of these three sites acquired about 150 subjects' images in high imaging resolution. After linear transformation to the MNI space, MR images from MNI were averaged to create the MNI152 (i.e. ICBM152) atlas, which has better contrast and coverage of the human brain than the MNI305 atlas. Many brain image analysis software, such as SPM [10], FSL [11-13], have included the MNI152 atlas into their data analysis packages.

3.2 Image Registration Methods

Image Registration not only plays a crucial role in atlas construction, but also is an important tool in the MR image data analysis. As briefly introduced in the construction of MNI305 and MNI152 atlas, non-rigid linear image registration methods aligned MR images to a common coordinate and removed global shape differences among inter-subject scans. In doing so, the automated linear image registration procedure ensures the constructed atlas is not affected by brain size and orientation differences and, at the same time, can capture the anatomical variability among subjects. For the image data analysis tasks, various image registration algorithms are used to map patient and normal control datasets to a standard coordinate space e.g. MNI space. This allows voxel-based statistical analysis on the standard coordinate for cross-subject studies [14-18]. Moreover, state-of-the-art image registration algorithms can enable us to analyze 4D longitudinal datasets.

It is, however, beyond the scope of this short section to review medical image registration algorithms, which would be voluminous. Instead, we only briefly describe some important image registration algorithms employed in our study, which includes linear affine registration and Large Deformation Diffeomorphic Metric Mapping (LDDMM). People who are interested should refer to several review papers [19-22] for an update of this field.

Linear affine image transformation was employed in the construction of MNI305 and MNI152 atlas. The affine image transformation, in essence, is a composition of sequence of linear operations on the images. These linear operations may include translation, rotation, scaling and shearing. Under these operations, the parallel lines in the

images remain parallel. The optimal affine transformation for image registration is determined by maximizing the voxel similarity measure between two images. Voxel similarity measures are the main difference between various linear image registration algorithms. Studies have shown that the UCLA automated image registration (AIR) [23, 24] algorithm, which use the ratio of image uniformity (RIU) measure, and the linear registration algorithms based on mutual information (MI) [25, 26] have superior performance and consistency [27-29].

Both AIR and normalized Mutual Information image registration were employed in our study. To summarize, we consider MR images as scalar functions i.e. $I(x): \Omega = [0,1]^3 \rightarrow R, x \in \Omega$. For two images I_0, I_1, the AIR algorithm seeks the minimum of $RIU(I_0, I_1)$, which is defined by [29, 30]:

$$RIU(I_0, I_1) = \frac{\sigma\left(\frac{I_1}{I_0}\right)}{\mu\left(\frac{I_1}{I_0}\right)} \tag{3.1}$$

Where N is total number of voxels,

$$\mu\left(\frac{I_1}{I_0}\right) = \frac{1}{N}\sum_{x\in\Omega}\frac{I_1(x)}{I_0(x)} \tag{3.2}$$

And

$$\sigma\left(\frac{I_1}{I_0}\right) = \frac{1}{N}\sum_{x\in\Omega}\left(\mu\left(\frac{I_1}{I_0}\right) - \frac{I_1(x)}{I_0(x)}\right)^2 \tag{3.3}$$

The Normalized Mutual Information is defined as the ratio of joint entropy and marginal entropy, i.e. [26, 29]:

$$MI(I_0, I_1) = \frac{H(I_0) + H(I_1)}{H(I_0, I_1)} \tag{3.4}$$

Where

$$H(I_0) = -\sum_{m\in I_0(x)} P(m)\log\big(P(m)\big) \tag{3.5}$$

$$H(I_1) = -\sum_{n \in I_1(x)} P(n) \log\big(P(n)\big) \tag{3.6}$$

And

$$H(I_0, I_1) = -\sum_{(m,n) \in I_0(x) \times I_1(x)} P(m,n) \log\big(P(m,n)\big) \tag{3.7}$$

For image data analysis tasks, such as intra-subject image comparison, affine image registration is often employed because the neuroanatomy of the subject is not significantly altered [31, 32]. AIR and Mutual Information based linear registration algorithms can also successfully match intra-subject scans from different modalities. However, to study inter-subject variability and 4D longitudinal dataset, high-dimensional image transformations are often needed to accommodate individual variability.

Many high-dimensional image registration algorithms are developed based on physical models. Two examples of the physical models are linear elastic-solid model and viscous-fluid model. In our study, we employed the Large Deformation Diffeomorphic Metric Mapping (LDDMM) [33, 34], which is based on the viscous-fluid model. An important property of the viscous-fluid model is that it allows for large deformations [35, 36], which is necessary for our analysis of Alzheimer's and other neurodegenerative disease image data, where the anatomical structures are often characterized with large variability.

Different from elastic-solid model, which assumes infinitesimally small deformations and penalizes large deformation by regularization, viscous-fluid model allows for large deformation by generating transformations in a velocity vector field $v_t \in V, t \in [0,1]$, where V is the space of smooth velocity vector field. This velocity vector field is governed by a differential equation [37]:

$$\dot{\phi}_t = v_t(\phi_t), t \in [0,1] \tag{3.8}$$

Where ϕ is the transformation between the two images I_0 and I_1. Upon integration, we can have the image transformation:

$$\varphi(x) = \phi_1(x) = \phi_0(x) + \int_0^1 v_t\big(\phi_t(x)\big)dt \tag{3.9}$$

Solution to the differential equation E.q. 3.8 exists in the space of diffeomorphism (see [38] for details). The diffeomorphic transformations are bijective, and continuously differentiable with differentiable inverse. After the diffeomorphic transformations, the topology of the image is still preserved, i.e. connected components remain connected and disjoint components remain disjoint. The optimal diffeomorphic transformation is estimated via the variational problem, which takes following form:

$$\hat{v} = \underset{v:\dot{\phi}_t = v_t(\phi_t)}{argmin} \left(\int_0^1 \|v_t\|_V^2 dt + \frac{1}{\sigma^2} \|I_0 \circ \varphi^{-1} - I_1\|_{L^2}^2 \right) \tag{3.10}$$

Where $\|\cdot\|_V$ is the function norm on the velocity field v_t, and the second term measures the residue of the image matching with $\|\cdot\|_{L^2}$ representing the L^2 squared-error norm.

3.3 Applications of Atlas-Based Approach in MRI

The main application of atlases in neuroimaging research has been analysis and reporting of neuroimaging findings. Nowadays, this kind of atlas-based analyses has become quite routine and efficient, as many powerful software packages, e.g. SPM, have integrated the neuroimaging atlases into their data analysis tools. Using these software packages, images from different subjects can be easily compared and studied in the standard atlas space.

In fact, by utilizing an atlas-based image analysis pipeline, both shape and neuroanatomical configuration of the brain can be studied in the same framework. Normally, at the beginning of the pipeline, images are transformed to the atlas space using image transformation algorithms. The image voxels can be compared using voxel-based morphormetry [18] and the deformation fields obtained from the nonlinear image registration can be used to estimate brain shape differences.

Volumetric parcellations of the human brain atlases are also important tools for analyzing brain image data. One well-known example of human brain parcellation is the Automatic Anatomical Labeling (AAL) atlas [39], which consists 90 anatomical ROIs (45 ROIs per hemisphere) in the MNI space. This AAL atlas has versatile applications in neuroimaging research. For instance, many fMRI studies are relying on the AAL atlas to label clusters of activation. Also, the atlas is frequently used to analyze brain functional and structural networks [40, 41].

3.4 Overview of Atlas-Based Approach using Diffusion Tensor Imaging and White Matter Tractography

Previously, MR image atlases, such as MNI152, contain limited information about white matter because this tissue appears almost homogeneous in conventional MRI. With the advent of diffusion tensor imaging, we not only obtain additional image contrasts for brain white matter, but also gain important orientation information about axonal fiber bundles. These new information give us opportunities to create atlas-based data analysis tools for human brain white matter.

a) Stereotaxic White Matter Atlas in MNI space

Creating a white matter atlas in the standard coordinate is the first step toward atlas-based analysis of white matter. Additionally, by using MNI152 as the reference template for white matter atlas, we can combine results of multi-modality studies in one coordinate system.

The procedures to build a population-averaged human brain white matter atlas in MNI space is similar to that for MNI152 i.e. linear affine image registration algorithms such as AIR and MI based linear affine image registration are used to generate the transformation matrix to bring diffusion tensor images to MNI space. However, one thing to note is that transforming diffusion tensor field is not the same as transforming scalar images, which is done via image interpolation. To apply linear affine transformations that include rotation, scaling and shearing, the diffusion tensor needs to be properly re-oriented, yet, the shape and size of the diffusion tensor should not change, i.e. the eigenvalues should remain the same [42, 43].

Suppose A is a 3×3 affine transformation matrix and v, v_2, v_3 and $\lambda_1, \lambda_2, \lambda_3$ are eigenvectors and eigenvalues of diffusion tensor D where

$$D = \lambda_1 v_1 \cdot v_1^T + \lambda_2 v_2 \cdot v_2^T + \lambda_3 v_3 \cdot v_3^T \tag{3.11}$$

To apply the transformation, we reorient each eigenvector using the affine transformation matrix, i.e.

$$u_1 = Av_1;\ u_2 = Av_2;\ u_3 = Av_3 \tag{3.12}$$

After these reorientations, we normalize the respective eigenvectors using the Gram-Schmidt process

$$e_1 = \frac{u_1}{\|u_1\|} \tag{3.13}$$

$$e_2 = \frac{u_2 - (u_2^T \cdot e_1)e_1}{\|u_2 - (u_2^T \cdot e_1)e_1\|} \tag{3.14}$$

$$e_3 = \frac{u_3 - (u_3^T \cdot e_1)e_1 - (u_3^T \cdot e_2)e_2}{\|u_3 - (u_3^T \cdot e_1)e_1 - (u_3^T \cdot e_2)e_2\|} \tag{3.15}$$

Finally, we reconstruct the diffusion tensor using

$$D = \lambda_1 e_1 \cdot e_1^T + \lambda_2 e_2 \cdot e_2^T + \lambda_3 e_3 \cdot e_3^T \tag{3.16}$$

A population-averaged stereotaxic atlas (ICBM-DTI-81) of human brain white matter was introduced by our group using diffusion tensor images from 81 subjects [44]. Particularly, based on the fiber orientation information in the atlas space, human brain white matter were divided into regions of deep white matter (DWM) and superficial white matter (SWM) [44-46]. These regions together constitute the white matter parcellation map (WMPM), which is a very useful tool for atlas-based analysis [46, 47]. Both the atlas and white matter parcellation map are shown in Figure 3.1 and are available for download from our website http://www.mristudio.org.

b) Probabilistic White Matter Tract Maps

Using white matter tractography, we can identify the coordinate of white matter fiber tracts and directly compare MR metrics on individual white matter tracking results. However, due to the limitations of diffusion tensor imaging, 3D tract reconstruction is marred by noise, partial volume effects, and complicated axonal structures. Furthermore, changes in diffusion anisotropy under pathological conditions could alter the results of 3D tract reconstruction.

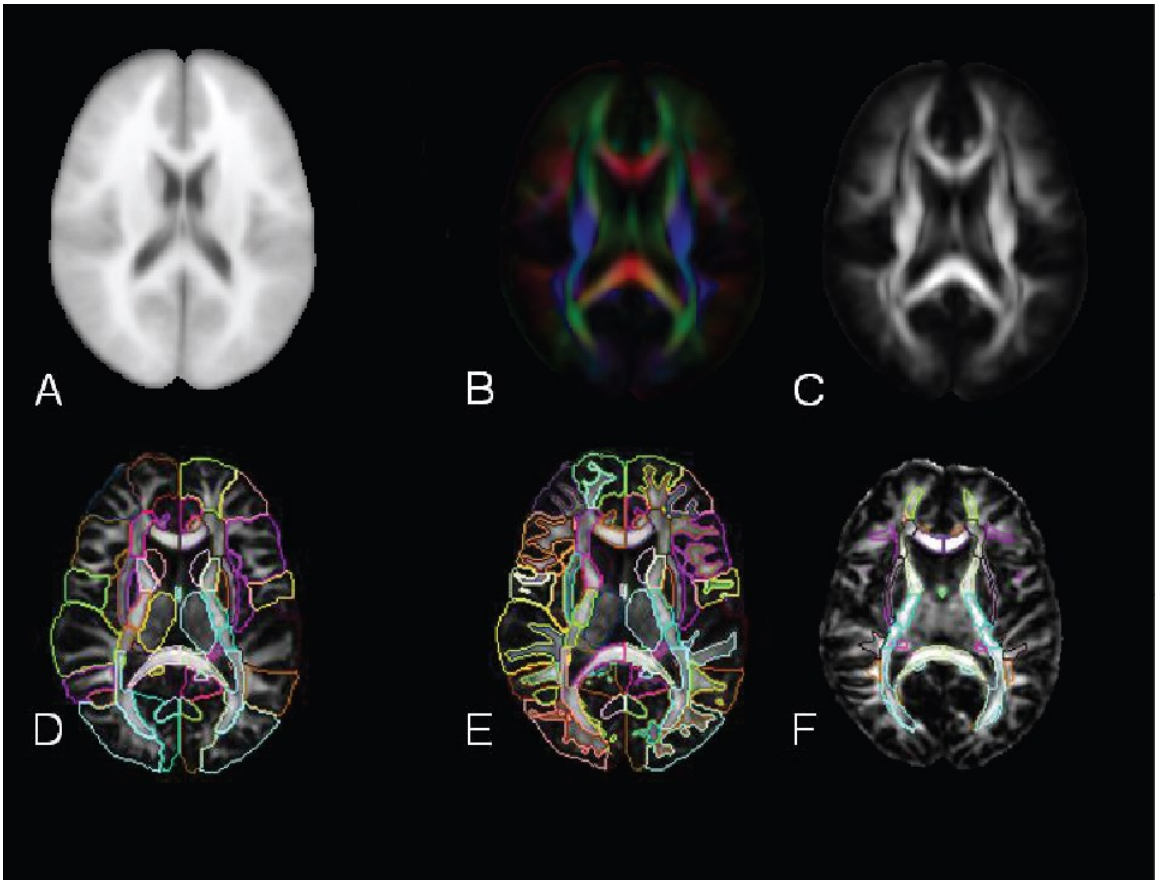

Figure 3.1: The first row shows images of MNI152 (A), averaged color map (B) and FA image (C) of ICBM-DTI-81 atlas. In the second row, image (F) shows the deep white matter regions. The image (D) is the Type II White Matter Parcellation Map, which contains deep white matter regions (DWM), peripheral white matter regions (superficial white matter region + cortex) and subcortical gray matters, hippocampi, and others. In (E), the superficial white matter and cortex are separated. The white matter parcellation maps show in (E) and (F) are called Type III and Type I White Matter Parcellation Map, respectively.

In this study, we developed a white matter parcelation atlas based on probabilistic maps of 11 major white matter tracts derived from the DTI data. Using these probabilistic maps, automated tract-specific quantification of MR metrics can be performed. This is an efficient tool for initial screening of the status of multiple white matter tracts.

c) Functional Area Mapping in the Human Cortex Based on Connectivity through Association Fibers

In the human brain, different regions of the cortex communicate via white matter tracts. Investigation of this connectivity is essential for understanding brain function. By extrapolating the fiber orientation information obtained from diffusion tensor imaging, cortical regions associated with a specific white matter tract can be estimated.

In this study, we created population-averaged cortical maps of brain connectivity for 4 major association fiber tracts, the corticospinal tract (CST), and commissural fibers. It is shown that these 4 association fibers interconnect all 4 lobes of the hemispheres. Cortical regions that were assigned based on association with the CST and the superior longitudinal fasciculus (SLF) agreed with locations of their known (CST: motor) or putative (SLF: language) functions. This approach can potentially be used for quantitative assessment of the effect of white matter abnormalities on associated cortical regions.

d) Automated Tract-Specific Quantification Using Probabilistic Atlas Based on Large Deformation Diffeomorphic Metric Mapping

The atlas-based tract-specific quantification relies on the brain registration quality. To improve the accuracy of registration, we employed Multichannel Large Deformation

Diffeomorphic Metric Mapping (LDDMM) [34]. Using this algorithm, tract-specific analysis of patient with severe brain atrophy becomes possible.

Briefly, the Multichannel LDDMM takes advantage of various contrasts available from diffusion tensor imaging. The B0 image (the minimum diffusion weighted image), has clear definition of brain boundary and ventricle surface, but this image lacks contrast in the white matter. On the other hand, the converse is true for FA image. Using these two imaging contrast as inputs to the registration algorithm, the registration accuracy is significantly improved [34].

In our implementation, FA and B0 images were used as components of vector valued images $\boldsymbol{I}_0$ and $\boldsymbol{I}_1$. The Multichannel LDDMM seeks optimal transformation by minimizing following problem:

$$\hat{v} = \underset{v:\dot{\phi}_t = v_t(\phi_t)}{argmin} \left(\int_0^1 \|v_t\|_V^2 dt + \sum_{c=1}^{C} \left\{ \frac{1}{\sigma^2} \|\boldsymbol{I_{0c}} \circ \varphi^{-1} - \boldsymbol{I_{1c}}\|_{L^2}^2 \right\} \right) \tag{3.17}$$

where c is the number of image components in the vector valued image.

e) Human Brain Network Analysis Using Automated Fiber Tracking

So far, most of human brain white matter fiber bundles have been delineated manually by labeling multiple regions of interest (ROI). This process is labor intensive and subject to operator bias. It also limits our ability to systemically analysis human brain networks.

In this study, we utilized White Matter Parcellation Map (WMPM) and multi-channel LDDMM to automatically delineate cortico-cortical connections. This method simultaneously reconstructed thousands of connections in the human brain network.

We employed statistical learning algorithms e.g. Support Vector Machine (SVM), to compare the brain networks of Alzheimer's patient and normal elderly group. Analyses result showed there are significant differences in the structural network of the two groups.

Recently, people have classified MR scans of Alzheimer's patient and normal aging using voxels in T1 images [48]. Our method classified these images using connection information obtained from diffusion tensor imaging. Compared to the voxel-based approach, our method has significantly reduced dimension. Since neuronal degeneration likely starts in the neuronal periphery and affects fiber tracts, this could potentially be an important tool to characterize the human brain and study neurodegenerative diseases.

3.5 References

1. Paxinos, G. and C. Watson, *The rat brain in stereotaxic coordinates*. 6th ed. 2007, Amsterdam ; Boston ;: Academic Press/Elsevier.

2. Talairach, J. and P. Tournoux, *Co-planar stereotaxic atlas of the human brain. 3-Dimensional proportional system: An approach to cerebral imaging*. 1988, New York, NY: Thieme Medical.

3. Fox, P.T., J.S. Perlmutter, and M.E. Raichle, *A STEREOTACTIC METHOD OF ANATOMICAL LOCALIZATION FOR POSITRON EMISSION TOMOGRAPHY.* Journal of Computer Assisted Tomography, 1985. **9**(1): p. 141-153.

4. Evans, A.C., et al., *3D STATISTICAL NEUROANATOMICAL MODELS FROM 305 MRI VOLUMES*. Nuclear Science Symposium & Medical Imaging Conference, Vols 1-3: 1993 Ieee Conference Record, ed. L.A. Klaisner. 1993, New York: I E E E. 1813-1817.

5. Mazziotta, J., et al., *A probabilistic atlas and reference system for the human brain: International Consortium for Brain Mapping (ICBM).* Philos Trans R Soc Lond B Biol Sci, 2001. **356**(1412): p. 1293-322.

6. Evans, A.C., et al., *Brain templates and atlases.* Neuroimage, 2012. **62**(2): p. 911-922.

7. Collins, D.L., et al., *AUTOMATIC 3D INTERSUBJECT REGISTRATION OF MR VOLUMETRIC DATA IN STANDARDIZED TALAIRACH SPACE.* Journal of Computer Assisted Tomography, 1994. **18**(2): p. 192-205.

8. Holmes, C.J., et al., *Enhancement of MR images using registration for signal averaging.* Journal of Computer Assisted Tomography, 1998. **22**(2): p. 324-333.

9. Mazziotta, J.C., et al., *A PROBABILISTIC ATLAS OF THE HUMAN BRAIN - THEORY AND RATIONALE FOR ITS DEVELOPMENT.* Neuroimage, 1995. **2**(2): p. 89-101.

10. Friston, K.J., *Statistical parametric mapping : the analysis of funtional brain images*. 1st ed. 2007, Amsterdam ; Boston: Elsevier/Academic Press. vii, 647 p.

11. Jenkinson, M., et al., *FSL.* Neuroimage, 2012. **62**(2): p. 782-790.

12. Woolrich, M.W., et al., *Bayesian analysis of neuroimaging data in FSL.* Neuroimage, 2009. **45**(1): p. S173-S186.

13. Smith, S.M., et al., *Advances in functional and structural MR image analysis and implementation as FSL.* Neuroimage, 2004. **23**: p. S208-S219.

14. Fox, P.T., et al., *ENHANCED DETECTION OF FOCAL BRAIN RESPONSES USING INTERSUBJECT AVERAGING AND CHANGE-DISTRIBUTION ANALYSIS OF SUBTRACTED PET IMAGES.* Journal of Cerebral Blood Flow and Metabolism, 1988. **8**(5): p. 642-653.

15. Fox, P.T. and M.A. Mintun, *NONINVASIVE FUNCTIONAL BRAIN MAPPING BY CHANGE-DISTRIBUTION ANALYSIS OF AVERAGED PET IMAGES OF (H2O)-O-15 TISSUE ACTIVITY.* Journal of Nuclear Medicine, 1989. **30**(2): p. 141-149.

16. Worsley, K.J., et al., *A 3-DIMENSIONAL STATISTICAL-ANALYSIS FOR CBF ACTIVATION STUDIES IN HUMAN BRAIN.* Journal of Cerebral Blood Flow and Metabolism, 1992. **12**(6): p. 900-918.

17. Worsley, K.J., et al., *A unified statistical approach for determining significant signals in images of cerebral activation.* Human Brain Mapping, 1996. **4**(1): p. 58-73.

18. Ashburner, J. and K.J. Friston, *Voxel-based morphometry - The methods.* Neuroimage, 2000. **11**(6): p. 805-821.

19. Maintz, J.B. and M.A. Viergever, *A survey of medical image registration.* Medical image analysis, 1998. **2**(1): p. 1-36.

20. Zitova, B. and J. Flusser, *Image registration methods: a survey.* Image and Vision Computing, 2003. **21**(11): p. 977-1000.

21. Szeliski, R., *Image alignment and stitching: a tutorial.* Foundations and Trends in Computer Graphics and Vision, 2006. **2**(1): p. 1-105.

22. Sotiras, A., C. Davatzikos, and N. Paragios, *Deformable Medical Image Registration: A Survey.* Ieee Transactions on Medical Imaging, 2013. **32**(7): p. 1153-1190.

23. Woods, R.P., et al., *Automated image registration: I. General methods and intrasubject, intramodality validation.* J Comput Assist Tomogr, 1998. **22**(1): p. 139-52.

24. Woods, R.P., et al., *Automated image registration: II. Intersubject validation of linear and nonlinear models.* Journal of Computer Assisted Tomography, 1998. **22**(1): p. 153-165.

25. Maes, F., et al., *Multimodality image registration by maximization of mutual information.* Ieee Transactions on Medical Imaging, 1997. **16**(2): p. 187-198.

26. Studholme, C., D.L.G. Hill, and D.J. Hawkes, *An overlap invariant entropy measure of 3D medical image alignment.* Pattern Recognition, 1999. **32**(1): p. 71-86.

27. Strother, S.C., et al., *QUANTITATIVE COMPARISONS OF IMAGE REGISTRATION TECHNIQUES BASED ON HIGH-RESOLUTION MRI OF THE BRAIN.* Journal of Computer Assisted Tomography, 1994. **18**(6): p. 954-962.

28. West, J., et al., *Comparison and evaluation of retrospective intermodality brain image registration techniques.* Journal of Computer Assisted Tomography, 1997. **21**(4): p. 554-566.

29. Holden, M., et al., *Voxel similarity measures for 3-D serial MR brain image registration.* Ieee Transactions on Medical Imaging, 2000. **19**(2): p. 94-102.

30. Woods, R.P., S.R. Cherry, and J.C. Mazziotta, *RAPID AUTOMATED ALGORITHM FOR ALIGNING AND RESLICING PET IMAGES.* Journal of Computer Assisted Tomography, 1992. **16**(4): p. 620-633.

31. Hajnal, J.V., et al., *DETECTION OF SUBTLE BRAIN CHANGES USING SUBVOXEL REGISTRATION AND SUBTRACTION OF SERIAL MR-IMAGES.* Journal of Computer Assisted Tomography, 1995. **19**(5): p. 677-691.

32. Hajnal, J.V., et al., *A REGISTRATION AND INTERPOLATION PROCEDURE FOR SUBVOXEL MATCHING OF SERIALLY ACQUIRED MR-IMAGES.* Journal of Computer Assisted Tomography, 1995. **19**(2): p. 289-296.

33. Beg, M.F., et al., *Computing large deformation metric mappings via geodesic flows of diffeomorphisms.* International Journal of Computer Vision, 2005. **61**(2): p. 139-157.

34. Ceritoglu, C., et al., *Multi-contrast large deformation diffeomorphic metric mapping for diffusion tensor imaging.* Neuroimage, 2009. **47**(2): p. 618-627.

35. Christensen, G.E., R.D. Rabbitt, and M.I. Miller, *3D BRAIN MAPPING USING A DEFORMABLE NEUROANATOMY.* Physics in Medicine and Biology, 1994. **39**(3): p. 609-618.

36. Christensen, G.E., R.D. Rabbitt, and M.I. Miller, *Deformable templates using large deformation kinematics.* Ieee Transactions on Image Processing, 1996. **5**(10): p. 1435-1447.

37. Arnol′d, V.I., *Ordinary differential equations*. 1973, Cambridge,: MIT Press. viii, 280 p.

38. Dupuis, P., U. Grenander, and M.I. Miller, *Variational problems on flows of diffeomorphisms for image matching.* Quarterly of Applied Mathematics, 1998. **56**(3): p. 587-600.

39. Tzourio-Mazoyer, N., et al., *Automated anatomical labeling of activations in SPM using a macroscopic anatomical parcellation of the MNI MRI single-subject brain.* Neuroimage, 2002. **15**(1): p. 273-89.

40. Achard, S., et al., *A resilient, low-frequency, small-world human brain functional network with highly connected association cortical hubs.* Journal of Neuroscience, 2006. **26**(1): p. 63-72.

41. Bullmore, E. and O. Sporns, *Complex brain networks: graph theoretical analysis of structural and functional systems.* Nat Rev Neurosci, 2009. **10**(3): p. 186-98.

42. Alexander, D.C., et al., *Spatial transformations of diffusion tensor magnetic resonance images.* Ieee Transactions on Medical Imaging, 2001. **20**(11): p. 1131-1139.

43. Xu, D.R., et al., *Spatial normalization of diffusion tensor fields.* Magnetic Resonance in Medicine, 2003. **50**(1): p. 175-182.

44. Mori, S., et al., *Stereotaxic white matter atlas based on diffusion tensor imaging in an ICBM template.* Neuroimage, 2008. **40**(2): p. 570-82.

45. Oishi, K., et al., *Human brain white matter atlas: Identification and assignment of common anatomical structures in superficial white matter.* Neuroimage, 2008. **43**(3): p. 447-457.

46. Oishi, K., et al., *Atlas-based whole brain white matter analysis using large deformation diffeomorphic metric mapping: Application to normal elderly and Alzheimer's disease participants.* Neuroimage, 2009. **46**(2): p. 486-499.

47. Mori, S., K. Oishi, and A.V. Faria, *White matter atlases based on diffusion tensor imaging.* Current Opinion in Neurology, 2009. **22**(4): p. 362-369.

48. Kloppel, S., et al., *Automatic classification of MR scans in Alzheimer's disease.* Brain, 2008. **131**(Pt 3): p. 681-9.

Chapter 4

Tract Probability Maps in Stereotaxic Space: Analyses of White Matter Anatomy and Tract-Specific Quantification

4.1 Introduction

White matter diseases are often characterized by various types of MR abnormalities, including T2-weighted hyperintensity, T1-weighted hypointensity, reduced magnetization transfer ratio (MTR), and, more recently, by decreased diffusion anisotropy or increased diffusivity. For accurate correlation of anatomic abnormalities with neurologic dysfunction, precise characterization of lesion location is of great importance. However, localization of the lesion and quantification of its severity are challenging tasks. This is especially the case for the white matter, which often appears homogeneous in conventional MRI.

Diffusion tensor imaging (DTI) has the potential to improve the localization information of white matter lesions because it can reveal detailed anatomy of the white matter [1-12]. Based on fiber orientation information obtained from DTI, we can identify the locations of various axonal bundles. By comparing this information with conventional MR parameter maps, we can identify specific white matter tracts that are affected by the lesions. We can extend this approach in a more systematic way by identifying the 3D trajectories of individual white matter tracts using 3D tract reconstruction or tractography [14-18]. Once a tract of interest is defined in three dimensions, we can superimpose its coordinates on MR parameter maps to perform quantitative tract-specific monitoring of pathological conditions [7, 19-24].

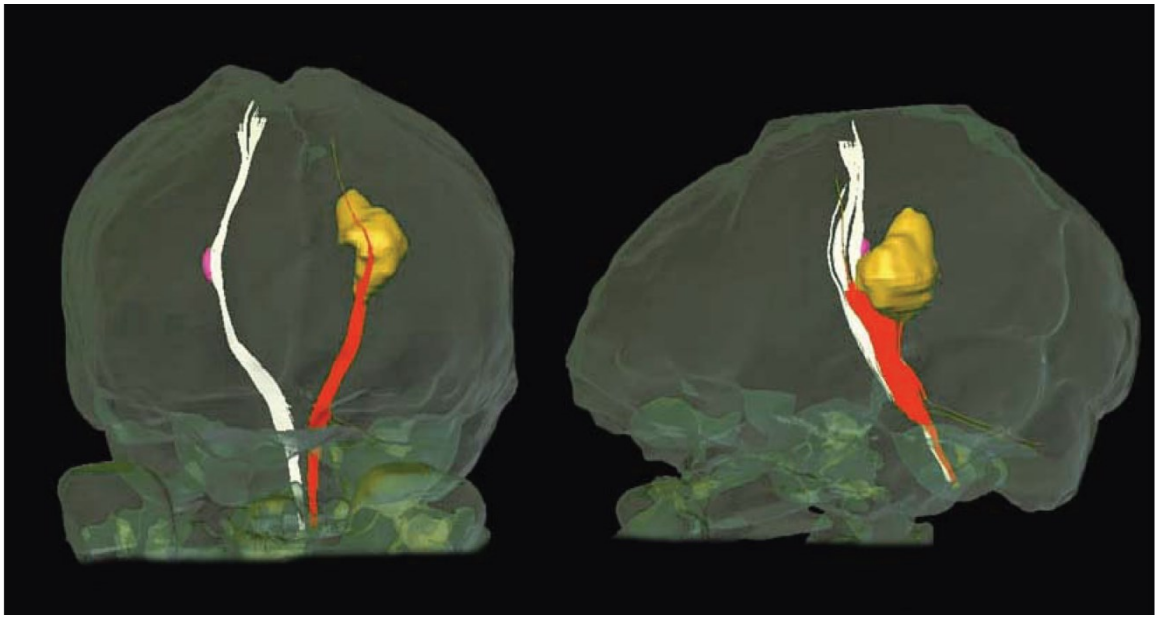

Fig. 4.1: Reconstruction of cortical spinal tract in a multiple sclerosis patient. Lesions with low diffusion anisotropy are indicated by yellow (left hemisphere) and pink (right hemisphere) colors. The corticospinal tract is successfully reconstructed in the right hemisphere but not in the left, making it difficult to measure MR

It has been shown that tractography can faithfully reconstruct the cores of prominent white matter tracts by using existing anatomical knowledge as an anatomical constraint [7-9, 12, 25]. However, the results are sensitive to noise, partial volume effects, and convolution of axonal structures with different orientations within a voxel. Furthermore, diseased brains often have altered DTI parameters that could affect the tractography results. For instance, even if a tract of interest has a normal size and 3D trajectory, tractography may fail to reveal its entire course in the presence of decreased diffusion anisotropy (Fig. 4.1).

In this work, we describe probabilistic maps of white matter tracts using a DTI database of normal adult subjects. Tractography results were transformed from individuals into a template and group-averaged trajectories were calculated. The purpose is twofold. First, the population-averaged statistical maps can define the standard coordinates of the reproducible regions (cores) of the tracts. The resultant statistical maps of the normal population can then be used as a reference for abnormal white matter anatomy in neurodegenerative diseases. Second, the statistical template can be applied to individual patient data for automated white matter parcellation and for tract-specific quantification of MR parameters. This would mean that tractography for each individual is no longer necessary and the examination of multiple tracts can be performed automatically. This approach effectively eliminates the necessity to establish tractography protocols (e.g., descriptions to reproducibly define locations and sizes of seeding pixels across subjects) and to measure the reproducibility of the protocol. Although the quality of this template-based brain parcellation is heavily influenced by registration quality, this type of template-based quantification should provide an efficient means of initial assessment of the white matter status.

We performed reconstruction of 11 major white matter tracts using DTI data from 28 normal subjects, based on strict tracking protocols [13], and registered the coordinates into a common template in the DTI-JHU space (lbam.med.jhmi.edu or ww.DtiStudio.org) [10] and the MNI-ICBM152 space (www.loni.ucla.edu/ICBM) [26]. This work explains the tracking and normalization procedures for our atlas and demonstrates how it can be used to perform lesion-tract correlation studies. The results with the automated approach

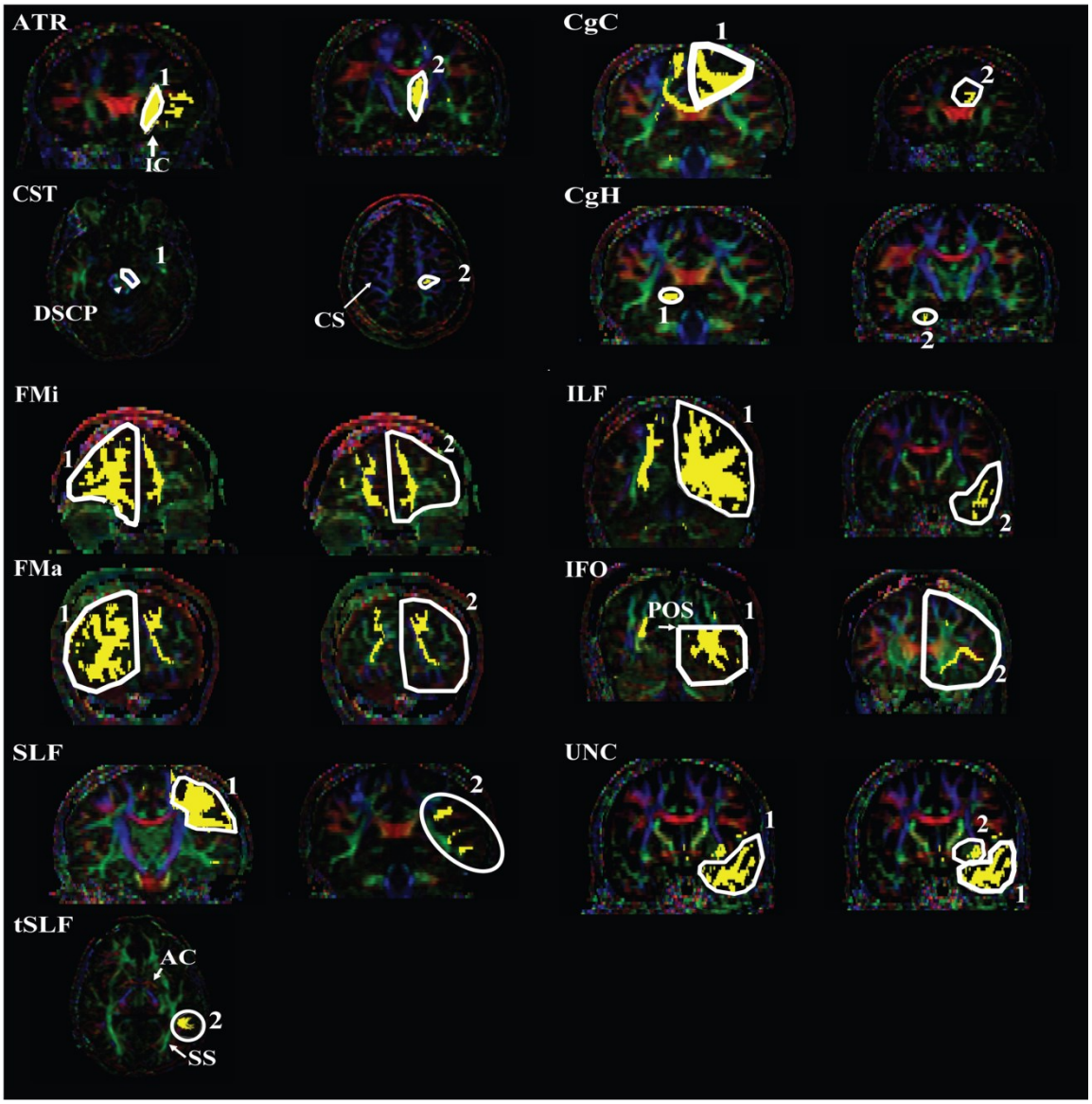

Fig. 4.2: ROI locations used for reconstructions of 11 white matter tracts in this paper. All tracts are reconstructed using a two-ROI approach, as previously published [13]. Abbreviations are: ATR: anterior thalamic radiation; CgC: cingulum in the cingulate cortex area; Cgh: cingulum in the hippocampal area; CST: cortitospinal tract; FMa: forceps major; FMi: forceps minor; IFO: inferior fronto-occipital fasciculus; SLF: superior longitudinal fasciculus; tSLF: the temporal projection of the SLF; UNC: uncinate fasciculus; DSCP: decussation of the superior cerebellar peduncle; POS: parieto-occipito sulcus. The tSLF shares the first ROI with SLF.

are then compared with a non-automated method, in which tractography is performed for individual subjects for validation.

4.2 Method

4.2.1 Subjects

Institutional Review Board approval was obtained for the study and written, informed consent, including HIPAA compliance, was obtained from all subjects. Twenty-eight healthy adults (mean 29±7.9 years old; male 17, female 11, all right-handed) participated in our study. No subject had a history of neurologic disease. For demonstration of the proposed method, a DTI dataset of a multiple sclerosis (MS) patient (32-year-old man) was used. The patient had a T2-hyperintense lesion in the left corona radiata and suffered weakness of the right arm and leg.

4.2.2 Imaging

A 1.5 T MR unit (Gyroscan NT, Philips Medical Systems) was used. DTI data were acquired with a single-shot, echo-planar imaging (EPI) sequence with sensitivity encoding (SENSE), using a parallel-imaging factor of 2.5 [27]. The imaging matrix was 96×96 with a field-of-view of 240×240 mm (nominal resolution, 2.5 mm), zero-filled to 256×256 pixels. Transverse sections of 2.5 mm thickness were acquired parallel to the anterior commissure–posterior commissure line. A total of 50-55 sections covered the entire hemisphere and brainstem without gaps. Diffusion weighting was encoded along 30 independent orientations [28], and the b-value was 700 mm^2/s. Five additional images with minimal diffusion weighting (b≅33 mm2/s) were also acquired. The scanning time

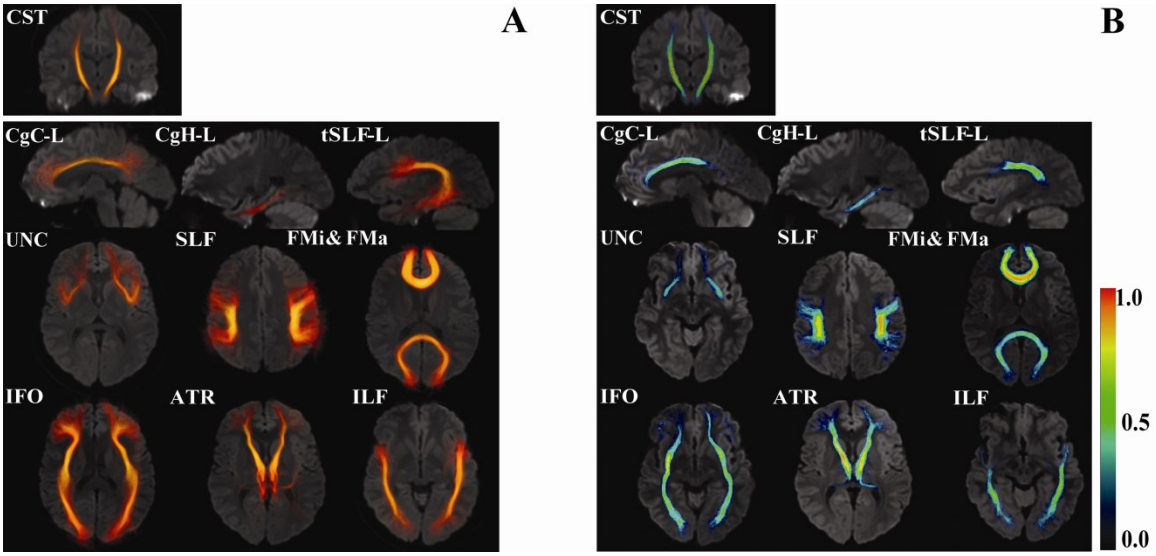

Fig. 4.3: Probabilistic maps of 11 white matter tracts. Results are superimposed on a single-subject JHU template. The 3D volume rendering of the averaged tract (A) and color-scaled probabilistic maps (B) are superimposed on 2D slices. Maximum intensity projection is used for the color intensity in (A). The color in (B) represents probability, as shown in the color bar.

per dataset was approximately 6 min. To enhance the signal-to-noise ratio, imaging was repeated 3 times (total 18 min).

Data from the MS patient were acquired using a 3.0 T MR unit (Philips Medical Systems). The imaging matrix was 112×112 with a field of view of 246×246 mm (nominal resolution, 2.2 mm), zero-filled to 256×256 pixels. Transverse sections of 2.2 mm thickness were acquired parallel to the anterior commissure-posterior commissure line. Other imaging parameters were the same as those for our normal DTI database.

4.2.3 Data processing

The DTI datasets were transferred to a personal computer running a Windows platform and were processed using DtiStudio (http://lbam.med.jhmi.edu or www.DtiStudio.org) [29]. Images were first realigned using Automatic Image Registration [30] using the first minimally diffusion-weighted image as a template in order to remove any potential small bulk motion that may have occurred during the scans. The six elements of the diffusion tensor were calculated for each pixel using multivariant linear fitting. After diagonalization, three eigenvalues and eigenvectors were obtained. For the anisotropy map, fractional anisotropy (FA) was used [4]. The eigenvector associated with the largest eigenvalue was used as an indicator of the fiber orientation. We also created an averaged diffusion-weighted image (aDWI) by adding all of the diffusion-weighted images. This image was used to drive cross-subject image registration.

4.2.4 Fiber Tracking and ROI drawing strategy

For the 3D tract reconstruction, the Fiber Assignment by Continuous Tractography (FACT) method [15, 20] was used with a fractional anisotropy threshold of 0.2 and a principal eigenvector turning angle threshold of 40° between two connected pixels. The fiber tracking based on FACT was performed by DtiStudio [29]. A multi-ROI approach was used to reconstruct tracts of interest [14, 25], exploiting existing anatomical knowledge of tract trajectories. Tracking was performed from all pixels inside the brain (the so-called brute-force approach), and fibers penetrating manually defined ROIs were assigned to the specific tracts associated with those ROIs. A description of the tracking protocol is provided in our previous papers [7, 10, 12, 13] and summarized in Fig. 4.2. In

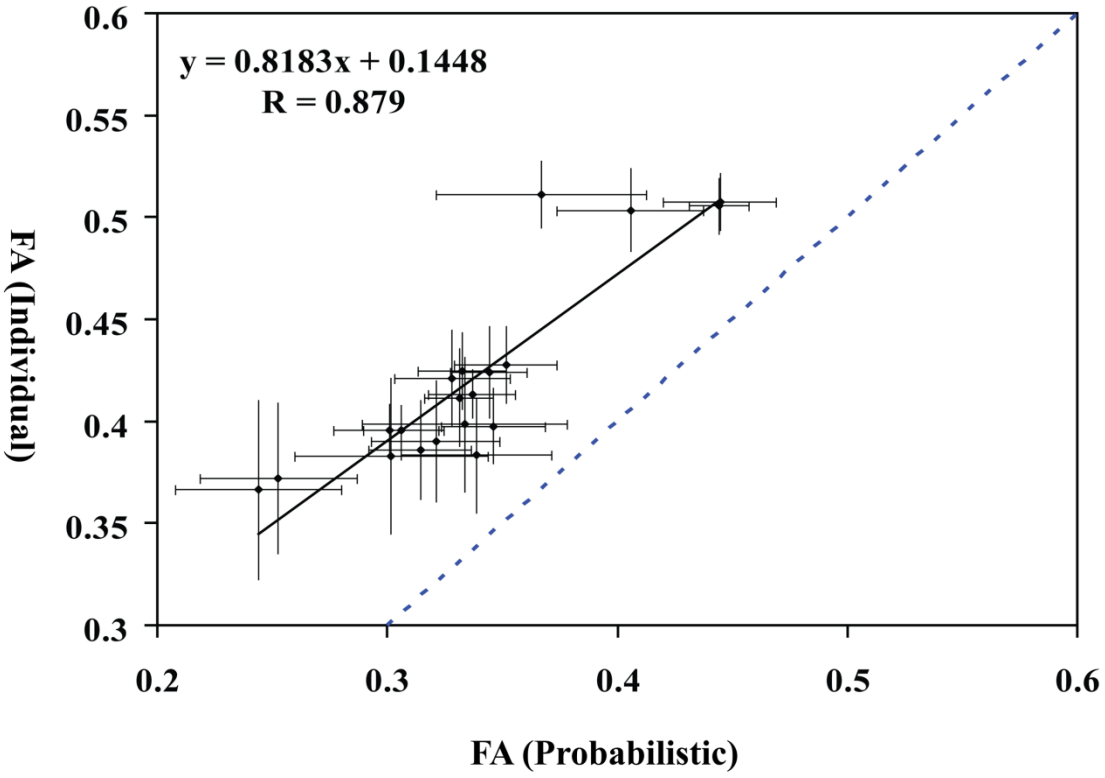

Fig. 4.4: Comparison of individual and probabilistic methods for 11 tracts. Data from the both hemisphere are plotted together. Horizontal axis is FA value measured by probabilistic method and vertical axis is FA value measured by individual method. Dashed line is the identity line. Standard deviations of both methods are also shown.

this study, we reconstructed the following 11 white matter tracts: forceps major (FMa); forceps minor (FMi); anterior thalamic radiation (ATR); cingulum of the cingulate cortex (CgC) and hippocampus (CgH); corticospinal tract (CST); inferior fronto-occipital fasciculus (IFO); inferior longitudinal fasciculus (ILF); superior longitudinal fasciculus (SLF); and uncinate fasciculus (Unc). There were two protocols for the SLF

reconstruction--one to reveal trajectories to the frontal, parietal, and temporal lobes, and the other to select only the projections to the temporal lobe (tSLF).

4.2.5 Tract probabilistic map

Two different templates were used for the spatial normalization: JHU-DTI [10, 11] and MNIICBM152 (http://www.loni.ucla.edu/ICBM/). A twelve-mode affine transformation [30] was used to co-register the 28 subjects' DTI images to these templates. For the transformation of each subject into one of the templates, the aDWI was used. The resultant affine transformation matrix was then applied to the subject's fiber tracts to transform them to the template. The binarized masks reporting on tract locations in the standard coordinates were averaged over 28 subjects to generate probabilistic maps, in which each pixel contains information about the probability. The JHU-DTI template and averaged fiber probability maps are available at http://lbam.med.jhmi.edu.

4.2.6 Atlas-based automated parcellation for tract-specific MR parameter quantification

The tract probabilistic maps were used as templates for automated parcellation of the white matter and to quantify MR parameters. First, DTI data, including FA images, were transformed to the template. Then, the probabilistic maps of the white matter tracts were superimposed on the patient data to calculate the FA intensities and Trace/3 (mean diffusivity) using the following equation:

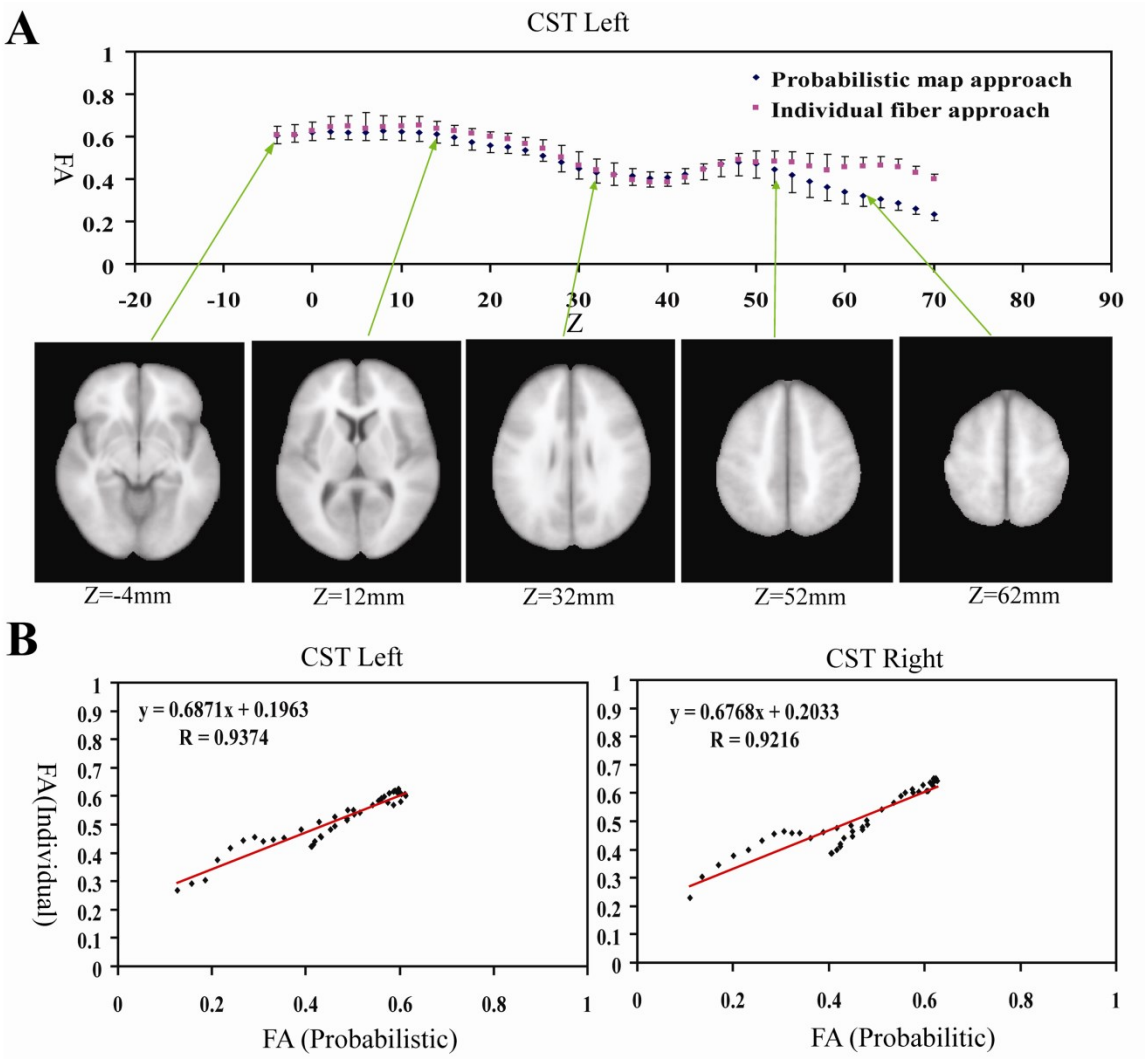

Fig. 4.5: Comparison of FA measurements by individual and probabilistic methods for the corticospinal tract (CST) at each z-coordinate of the MNI template (A) and correlation plots of the left (B) and right (C) CST. Each point in (B) and (C) corresponds to data points at each z-coordinate. The origin of the z-coordinate (z=0) is placed on the anterior commissure level. The averages and standard deviations were obtained from the 10 normal subjects.

$$\overline{FA} = \frac{\sum Pr_i \times FA_i}{\sum Pr_i} \tag{4.1}$$

$$\overline{Trace/3} = \frac{\sum Pr_i \times \frac{Trace}{3}}{\sum Pr_i} \tag{4.2}$$

where Pr_i is the probability of the ith voxel occupied by the reconstructed tract, empirically decided by the number of subjects with the tract occupying the ith voxel divided by the total number of subjects. FA_i and $Trace_i/3$ are the FA and Trace/3 values of the ith voxel, respectively.

4.2.7 Comparison with results from individual fiber tracking

The atlas-based automated parcellation method was compared with individual tracking results to evaluate the accuracy of the probabilistic approach. For this purpose, DTI data from 10 normal subjects, which were not included to generate the 28-subject probabilistic maps, were used. For the "individual tracking results," the tractography protocols in Fig. 4.2 were applied to the 10 normal data and the FA of each tract was measured. For the FA measurements, the tractography results were first converted to 1/0 binary maps (1: pixels that contained the fiber, 0: pixels that did not contain the fiber) and the maps were applied to FA maps as a masking. In this case, the tract coordinates and FA maps were both from the same subject. For "probabilistic results," the tract probability maps obtained from the 28-subject data were applied to the 10 normal subjects. For FA measurements, Eq. (4.1) was used. In this case, the tract coordinates and FA maps were from different subjects. Results of these two approaches were then compared by Pearson correlation analysis.

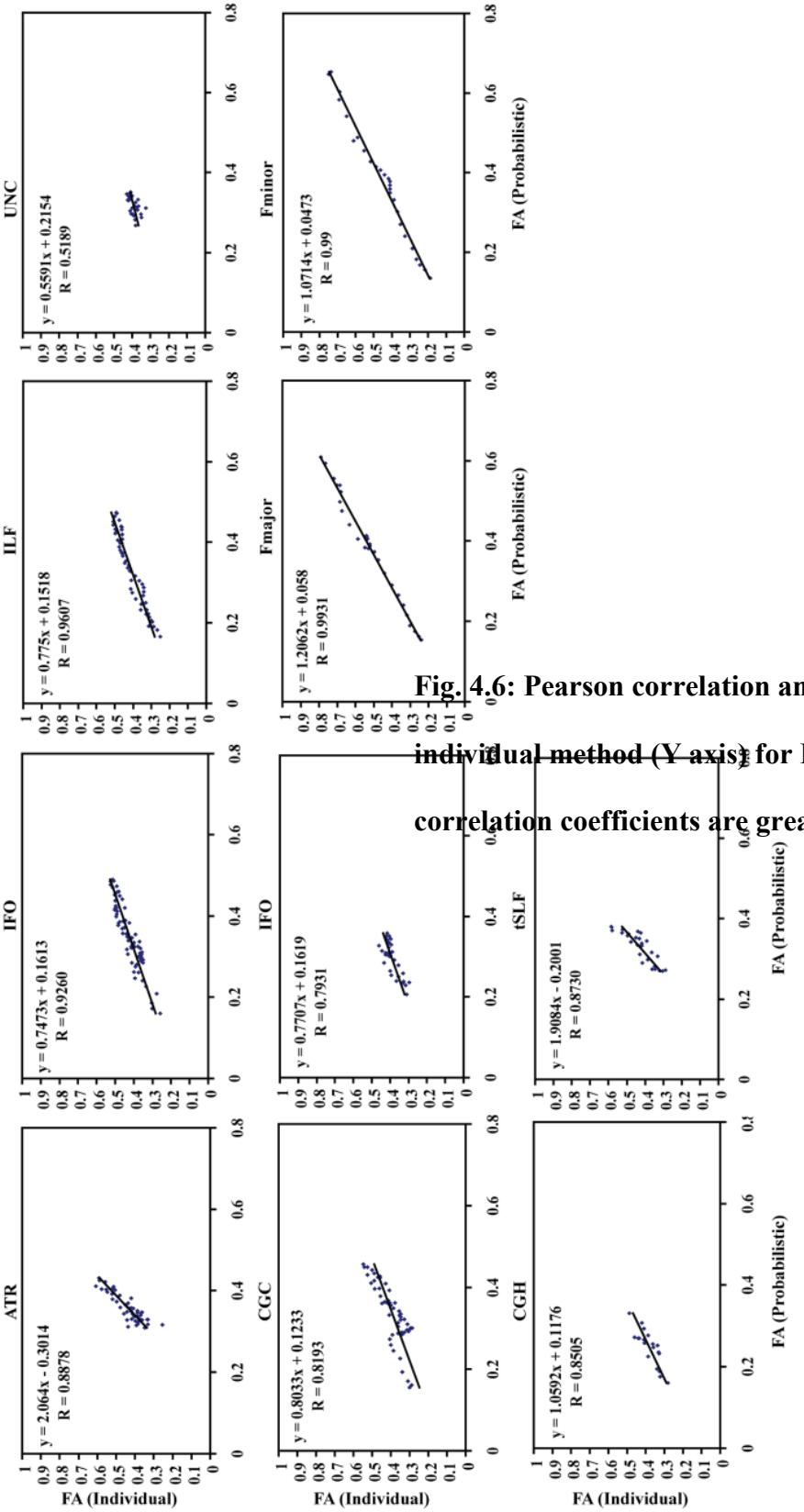

Fig. 4.6: Pearson correlation analysis of probabilistic method (X a

individual method (Y axis) for FA measurements of 10 fiber tract

correlation coefficients are greater than 0.82, except for UNC and

4.2.8 Software for automated tract-specific parcellation

The atlas-based automated parcellation method introduced in this work was implemented in our DtiStudio:RoiEditor module (lbam.med.jhmi.edu, godzilla.kennedykrieger.org, or www.MriStudio.org), which provides a user interface for this automated tract-specific quantification. The software reports the quantification results for the entire pathways or for each image slice in the three orthogonal planes.

4.3 Result

Fig. 4.3 shows the results of probabilistic maps of 11 white matter tracts reconstructed in the template coordinates. These tracts are well-defined at the core with higher probabilities, while they become more dispersed and have lower probabilities as they approach target cortical regions. In Fig. 4.4, individual and probabilistic methods were compared for the 11 tracts. For each tract, averages and the standard deviations among the subjects are plotted for both methods. The correlation constant for all the tracts is 0.88. The average coefficient of variation (=standard deviation/average) of the individual approach is 5.7% and the probabilistic approach is 8.0% for the 11 tracts, which may suggest a slightly higher precision for the individual approach. The slope is close to unity (0.82), but, for all tracts, the average values for the individual approach are higher, leading to the intercept of 0.14. To evaluate test-retest reproducibility, we scanned the same person three times (more than 24 hours apart for each session) and measured FA of the 11 tracts using both approaches. The coefficient of variation (standard deviation/average) indicated comparable reproducibility (probabilistic: 1.8±0.9% vs individual: 2.5±2.0% for the 11 tracts).

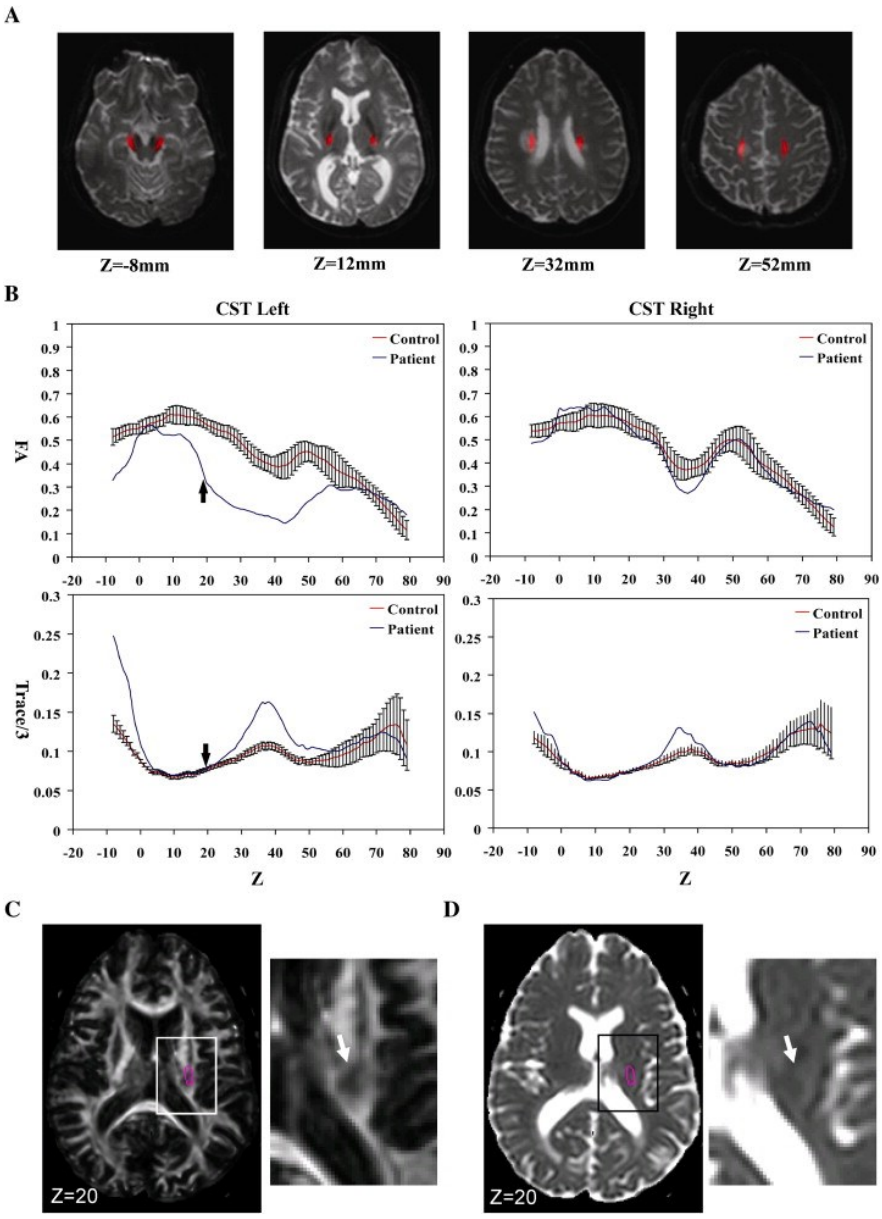

Fig. 4.7: Probabilistic FA quantification of the corticospinal tract (CST) of a MS patient in the MNI coordinates. As shown in Fig. 3.1, a low FA region in the central semiovale interferes with CST reconstruction of this patient. The probabilistic approach is not influenced by this type of lesions in individuals. The probabilistic CST coordinates are superimposed on the MS patient data (A) and FA and Trace/3 are measured for the left and right hemisphere (B).

For the corticospinal tract, the FA values of pixels within an axial slice are measured and plotted slice-by-slice to inspect individual probabilistic correlations along the tract pathway (Fig. 4.5A). The correlation is excellent in the core region (midbrain-corona radiata), but deteriorates in peripheral regions (subcortical white matter). The correlation coefficients are 0.94 and 0.92 for the left and right hemisphere (Figs. 4.5B and C), respectively, for the entire length in the hemisphere (−8 to 78 mm) and 0.99 for the core region (−8 to 52 mm). Fig. 4.6 shows the slice-by-slice correlation of the other 10 tracts (the entire length). The correlation coefficient was at least 0.82, except for UNC and SLF, which do not have enough dispersion in FA values, and all points are clustered in a confined region.

Fig. 4.7A shows the result of the automated white matter parcellation applied to a patient with relapsing-remitting MS. The probabilistic map of the corticospinal tract is superimposed on the normalized patient brain. The relative positions of the corticospinal tract and the T2-hyperintense lesion are visible in the normalized slice coordinates, z=32 mm–52 mm. The FA and Trace/3 value of the tract at each axial slice level are shown in Fig. 4.7B. The location and the spatial extent of the lesion along the tract are clearly identifiable. Although the lesion as seen on the trace map is not obvious at z<24 mm, the FA results suggest that the lesion extends beyond z=12 mm toward the midbrain. By visually inspecting these maps at z=20 mm, this observation can be readily confirmed (Figs. 4.7C and D).

4.4 Discussion

4.4.1 Probabilistic maps of tractography

In this work, probability maps of tractography results were created from our DTI database of 28 normal subjects. The results are registered to two standard coordinates – JHU-DTI and MNI coordinates – and are available for download from our website. Previously, probabilistic maps of white matter tracts [12, 31, 32], or tractography using averaged tensor fields [33], have been reported. This work proposes to use this approach for white matter parcellation in stereotaxic coordinates and for automated tract-specific quantification.

The validity of tractography has always been a subject of debate. All tracts described in this paper were reconstructed based on existing anatomical knowledge. Through the use of multiple ROIs, the reconstruction is designed to obtain tract trajectories that are faithful to existing anatomic knowledge to the extent possible [14, 25]. The trajectories between the multiple ROIs should reflect the macroscopic architecture of the white matter. One of the well known limitations of DTI-based tractography is that it cannot properly handle crossing fibers within a pixel [34, 35]. Tractography also contains errors due to noise and partial volume effects. Although these problems were ameliorated by adopting a multiple ROI approach, tractography results from a single subject could still contain false negatives and false positives, especially in the subcortical white matter regions. In our probabilistic approach, contributions of random errors should have been diminished through the group-averaging process. Nonetheless, it is reasonable to consider that the probabilistic maps contain erroneous white matter regions. Therefore, the obtained coordinates should be treated as an approximation of macroscopic organization of the white matter tracts.

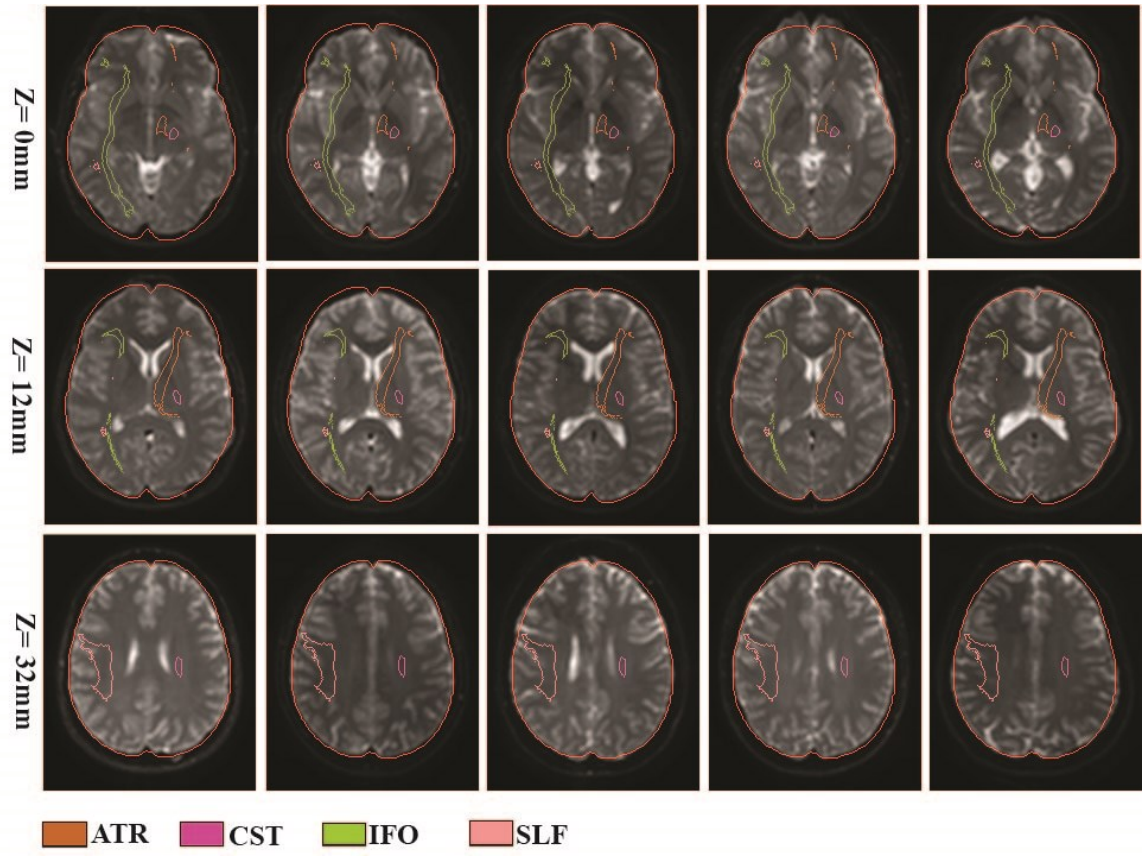

Fig. 4.8 Normalized images of subject #1, 3, 5, 7, and 9 used in Figs. 4, 5, and 6 to demonstrate registration quality. Three axial slices at z=0, 12, and 32 are shown, which reveal the probabilistic locations of the IFO (green), the SLF (peach), the ATR (orange), and the CST (pink). The outer boundary defines the shape of the ICBM-152 template.

4.4.2 Use of the probabilistic map as an anatomical template

There are two major usages for the tract probability maps. First, the maps can be generated for control and patient groups using the same template space and then can be superimposed. This would highlight and quantify the extent of regions in which tract

shape is different. This type of approach could be used as a screening tool to discover sensitive brain regions in which the core of the white matter anatomy is altered. Second, the maps can be used as templates for the parcellation of the white matter and tract-specific monitoring of MR parameters. In the past, tractography results have been used as ROI to perform tract-specific quantification of MR parameters [7, 19-24, 36-38]. The probabilistic approach described in this work can be considered as an extension of this idea. This probabilistic approach can be used for an MRI dataset without DTI (e.g., tract-specific quantification of T2 and magnetization transfer ratio). If high-quality DTI is available, this probabilistic approach may not be the ideal replacement for individual tractography or manual ROI-based analyses, which should provide better accuracy in localizing tracts of interest in each subject (see Fig. 4.5 and a recent publication that evaluates the reproducibility of tractography-based measurements [39]). However, there are two reasons the proposed method is useful. First, it can quickly screen the status of multiple tracts. For example, reporting of the FA of the 11 tracts is automated in DtiStudio:RoiEditor and takes less than 5 min. If any changes in patient populations are suspected in one of these tracts, it could efficiently direct the more time-consuming analyses to such regions. Second, when patients exhibit significant changes in pixel intensities, such as decreased FA, the results from the probability-based and individual-based methods may have significant differences, which would provide a new dimension in interpreting the status of the patient. This point is demonstrated in Figs. 4.1 and 4.7, in which the severe loss of FA prevented tract reconstruction.

In the probabilistic approach, pixels that belong to core regions of tracts, which are reproducible in the normal population, have larger weighting for tract-specific

quantification based on Eq. (4.1). The less reproducible regions are mostly at peripheral regions close to the cortex (Fig. 4.3B) and the quantification results are less accurate as seen in Fig. 4.5. Although these regions have lower weighting in Eq. (4.1), their contributions to the tract-specific FA and trace quantification (e.g., Fig. 4.4) could be non-negligible. This issue can be ameliorated by measuring slice-by-slice values, spatially separating the core and peripheral regions as shown in Figs. 4.5 and 4.7. In this work, we used simple probability-weighted averages for FA and trace quantification (Eqs. (4.1) and (4.2)). Several causes of inaccuracies in the probabilistic approach, such as inclusion of the gray matter and CSF, could be reduced by employing more elaborated methods such as histogram and outlier rejection.

One limitation of the atlas-based method is that the result depends on the quality of registration. The registration quality affects the analysis at two levels: (1) generation of the probabilistic map; and (2) application of the map to individual cases. In this study, we used a 12-mode affine transformation, which cannot remove non-linear differences. This leads to less-than-perfect anatomical registration in the resultant probabilistic maps. To demonstrate quality of the registration, the brain contour of the ICBM-152 and locations of several probabilistic tract maps are superimposed on the 5 normal subjects used in this study after affine transformation and shown in Fig. 4.8. To test the accuracy of the probabilistic approach, we compared individual and probabilistic results using the 10 normal subjects. We found excellent correlation between the two methods, but the probabilistic approach tended to yield a lower FA, mostly attributable to the peripheral white matter regions. This is understandable because slight misregistration in the

subcortical areas leads to inclusion of the cortex or even CSF. Interpretation of the absolute FA values from the probabilistic approach, thus, requires great care.

In our demonstration (Fig. 4.7), abnormally low FA and high Trace/3 are found in the midbrain region ($z<0$ mm), which is beyond the normal range of variation. Close inspection of the tract coordinates reveals that the probabilistic tract coordinates are not well registered to the normalized patient brain in the midbrain area because the patient has a noticeably smaller midbrain, which leads to partial inclusion of CSF. In this case, it is anatomical change, but not the actual FA or trace changes, that caused the abnormal values in the midbrain regions of Fig. 4.7. This is a good example that both anatomical ($z=-4$-0 mm) and intensity abnormalities ($z=10$-50 mm) would be detected by similar intensity changes in this type of normalization-based approach; we cannot immediately conclude changes are due to intensity or anatomical abnormality based solely on intensity change. Similarly, care must be taken when the probabilistic maps from an adult population are applied to pediatric or aged populations. Because different age groups are likely to have consistent anatomical differences, results of the probabilistic approach would be affected not only by real intensity changes such as decreased FA but also anatomical differences. This is an important limitation of this approach and, thus, our probabilistic maps should be used as an initial screening tool rather than for definitive conclusions. In other words, the role of this automated method is to bring our attention to areas with probable abnormalities. When an abnormal region is found, careful inspections and further analyses, such as manual ROI drawing or anatomical examinations, should follow (e.g., see Figs. 4.7D and E). In the future, adoption of non-linear transformation to

improve registration quality (thus minimizing the contributions of anatomical differences) will be an important research effort.

Another important limitation of the proposed approach is that our current atlas contains only selected white matter tracts. The 11 tracts were selected based on reproducibility measurements we performed prior to this study [13]. There could be many other important tracts for which we could not establish reproducible tracking protocols. Once the imaging resolution and SNR of DTI data improve, we expect that statistical maps of more tracts will be added to the atlas.

4.5 Conclusion

In this paper, we introduced a human brain white matter parcellation atlas based on probabilistic tract maps. We generated probabilistic maps of 11 major white matter tracts in two different templates. The probabilistic coordinates were superimposed on FA and trace maps of normal subjects for automated quantification of these parameters on a tract-by-tract basis. There was an excellent correlation between the probabilistic and individual tractography approaches. The data from an MS patient were used as an example to demonstrate how the atlas could be used to detect tract-specific abnormalities. The proposed method is an effective approach to initial evaluation of the status of major white matter tracts.

4.6 References

1. Douek, P., et al., *MR color mapping of myelin fiber orientation.* J.Comput.Assist.Tomogr., 1991. **15**: p. 923-929.

2. Basser, P.J., J. Mattiello, and D. Le Bihan, *MR diffusion tensor spectroscopy and imaging.* Biophys. J., 1994. **66**: p. 259-267.

3. Nakada, T. and H. Matsuzawa, *3-DIMENSIONAL ANISOTROPY CONTRAST MAGNETIC-RESONANCE-IMAGING OF THE RAT NERVOUS-SYSTEM - MR AXONOGRAPHY.* Neuroscience Research, 1995. **22**(4): p. 389-398.

4. Pierpaoli, C. and P.J. Basser, *Toward a quantitative assessment of diffusion anisotropy.* Magn.Reson.Med., 1996. **36**: p. 893-906.

5. Makris, N., et al., *Morphometry of in vivo human white matter association pathways with diffusion-weighted magnetic resonance imaging.* Annals of Neurology, 1997. **42**(6): p. 951-962.

6. Pajevic, S. and C. Pierpaoli, *Color schemes to represent the orientation of anisotropic tissues from diffusion tensor data: Application to white matter fiber tract mapping in the human brain.* Magnetic Resonance in Medicine, 1999. **42**(3): p. 526-540.

7. Stieltjes, B., et al., *Diffusion tensor imaging and axonal tracking in the human brainstem.* Neuroimage, 2001. **14**(3): p. 723-735.

8. Catani, M., et al., *Virtual in vivo interactive dissection of white matter fasciculi in the human brain.* Neuroimage, 2002. **17**(1): p. 77-94.

9. Jellison, B.J., et al., *Diffusion tensor imaging of cerebral white matter: A pictorial review of physics, fiber tract anatomy, and tumor imaging patterns.* American Journal of Neuroradiology, 2004. **25**(3): p. 356-369.

10. Wakana, S., et al., *Fiber Tract-based Atlas of Human White Matter Anatomy.* Radiology, 2004. **230**: p. 77-87.

11. Mori, S., et al., *MRI atlas of human white matter*. 2005, Amsterdam, The Netherlands: Elsevier.

12. Mori, S., et al., *Imaging cortical association using diffusion-tensor-based tracts in the human brain axonal tracking.* Magnetic Resonance in Medicine, 2002. **47**(2): p. 215-223.

13. Wakana, S., et al. *Reproducible protocol for human white matter fiber tracking and quantitative analysis of their status*. in *International Society of Magnetic Resonance in Medicine*. 2005. Miami.

14. Conturo, T.E., et al., *Tracking neuronal fiber pathways in the living human brain.* Proceedings of the National Academy of Sciences of the United States of America, 1999. **96**(18): p. 10422-10427.

15. Mori, S., et al., *Three-dimensional tracking of axonal projections in the brain by magnetic resonance imaging.* Annals of Neurology, 1999. **45**(2): p. 265-269.

16. Basser, P.J., et al., *In vivo fiber tractography using DT-MRI data.* Magnetic Resonance in Medicine, 2000. **44**(4): p. 625-632.

17. Poupon, C., et al., *Regularization of diffusion-based direction maps for the tracking of brain white matter fascicles.* Neuroimage, 2000. **12**(2): p. 184-195.

18. Parker, G.J.M., et al., *Initial demonstration of in vivo tracing of axonal projections in the macaque brain and comparison with the human brain using diffusion tensor Imaging and fast marching tractography.* Neuroimage, 2002. **15**(4): p. 797-809.

19. Virta, A., A.L. Barnett, and C. Pierpaoli, *Visualizing and characterizing white matter fiber structure and architecture in the human pyramidal tract using diffusion tensor MRI.* Magnetic Resonance Imaging, 1999. **17**(8): p. 1121-1133.

20. Xue, R., et al., *In vivo three-dimensional reconstruction of rat brain axonal projections by diffusion tensor imaging.* Magn. Reson. Med, 1999. **42**: p. 1123-1127.

21. Glenn, O.A., et al., *DTI-based three-dimensional tractography detects differences in the pyramidal tracts of infants and children with congenital hemiparesis.* Journal of Magnetic Resonance Imaging, 2003. **18**(6): p. 641-648.

22. Wilson, M., et al., *Pyramidal tract mapping by diffusion tensor magnetic resonance imaging in multiple sclerosis: improving correlations with disability.* Journal of Neurology Neurosurgery and Psychiatry, 2003. **74**(2): p. 203-207.

23. Partridge, S.C., et al., *Diffusion tensor imaging: serial quantitation of white matter tract maturity in premature newborns.* Neuroimage, 2004. **22**(3): p. 1302-1314.

24. Pagani, E., et al., *A method for obtaining tract-specific diffusion tensor MRI measurements in the presence of disease: Application to patients with clinically isolated syndromes suggestive of multiple sclerosis.* Neuroimage, 2005. **26**(1): p. 258-265.

25. Huang, H., et al., *Analysis of noise effects on DTI-based tractography using the brute-force and multi-ROI approach.* Magnetic Resonance in Medicine, 2004. **52**(3): p. 559-565.

26. Mazziotta, J., et al., *A probabilistic atlas and reference system for the human brain: International Consortium for Brain Mapping (ICBM).* Philos Trans R Soc Lond B Biol Sci, 2001. **356**(1412): p. 1293-322.

27. Pruessmann, K.P., et al., *SENSE: sensitivity encoding for fast MRI.* Magn Reson Med, 1999. **42**(5): p. 952-62.

28. Jones, D.K., M.A. Horsfield, and A. Simmons, *Optimal strategies for measuring diffusion in anisotropic systems by magnetic resonance imaging.* Magn. Reson. Med., 1999. **42**: p. 515-525.

29. Jiang, H.Y., et al., *DtiStudio: Resource program for diffusion tensor computation and fiber bundle tracking.* Computer Methods and Programs in Biomedicine, 2006. **81**(2): p. 106-116.

30. Woods, R.P., et al., *Automated image registration: I. General methods and intrasubject, intramodality validation.* J Comput Assist Tomogr, 1998. **22**(1): p. 139-52.

31. Xu, D., et al., *A framework for callosal fiber distribution analysis.* Neuroimage, 2002. **17**(3): p. 1131-43.

32. Ciccarelli, O., et al., *Diffusion tractography based group mapping of major white-matter pathways in the human brain.* Neuroimage, 2003. **19**(4): p. 1545-55.

33. Jones, D.K., et al., *Spatial normalization and averaging of diffusion tensor MRI data sets.* Neuroimage, 2002. **17**(2): p. 592-617.

34. Wiegell, M., H. Larsson, and V. Wedeen, *Fiber crossing in human brain depicted with diffusion tensor MR imaging.* Radiology, 2000. **217**: p. 897-903.

35. Tuch, D.S., et al., *Diffusion MRI of complex neural architecture.* Neuron, 2003. **40**(5): p. 885-95.

36. Berman, J.I., et al., *Quantitative diffusion tensor MRI fiber tractography of sensorimotor white matter development in premature infants.* Neuroimage, 2005. **27**(4): p. 862-871.

37. Jones, D.K., et al., *Age effects on diffusion tensor magnetic resonance imaging tractography measures of frontal cortex connections in schizophrenia.* Human Brain Mapping, 2006. **27**(3): p. 230-238.

38. Kanaan, R.A., et al., *Tract-specific anisotropy measurements in diffusion tensor imaging.* Psychiatry Research-Neuroimaging, 2006. **146**(1): p. 73-82.

39. Heiervang, E., et al., *Between session reproducibility and between subject variability of diffusion MR and tractography measures.* Neuroimage, 2006. **33**(3): p. 867-877.

Chapter 5

Mapping of Functional Areas in Human Cortex based on connectivity through Association Fibers

5.1 Introduction

It has been shown that diffusion tensor imaging (DTI) provides orientational information about white matter structures [1-7]. This has led to the technique of DTI tractography [8-13], which can faithfully reconstruct cores of prominent white matter tracts by using existing anatomical knowledge as anatomical constraints. The possibility of reconstructing these well-described white matter tracts leads to an interesting question: ‘‘Can we identify cortical regions associated with a white matter bundle?’’ Animal studies using neuroanatomical tracers and targeted lesions provide a fair amount of knowledge about white matter tracts that connect functional brain regions [14-16]. These include various projection fibers (connecting the cortex and other regions of the brains), such as thalamocortical and corticothalamic fibers, corticospinal fibers, and corticopontine fibers, to name a few [17, 18]. The connectivity of fibers associated with the limbic system, such as the fornix, the cingulum, and the stria terminalis, has also been well documented (see e.g., [19-22]. The connectivity information obtained from these animal studies has been a valuable resource from which to infer human brain connectivity.

One of the unique features of the human brain is the existence of prominent association fiber tracts that interconnect various regions of the cortex. These include the superior and inferior longitudinal fasciculus (SLF and ILF), the superior and inferior fronto-occipital fasciculus (SFO and IFO), and the uncinate fasciculus (UNC). These

tracts cannot be identified as discrete fiber bundles in rodent brains and are not well developed in nonhuman primate brains or in human fetal brains [23-25]. Consequently, the connected cortical regions and functions of these tracts have not been well characterized. It is, thus, of great interest to use noninvasive DTI tractography to estimate cortical regions that are related to these association fibers.

To use DTI tractography for this purpose, however, there are several difficulties. First, tracking data in individual brains are known to have errors due to noise and partial volume effects. Second, the tracking results are not accurate when image pixels contain complex axonal structures, such as crossing fibers [26]. This problem can be reduced by reconstructing only the core of white matter tracts with known trajectories. However, to identify associated cortical regions, the tracking results must be extended to subcortical white matter areas, which most likely consist of a mixture of axons with different destinations.

The purpose of this paper is to map cortical regions related to specific association fibers. These maps are expected to provide a quantitative way to estimate the relationship between the functional regions in the cortex and white matter tracts. To tackle the limitations of tractography, we adopted 2 strategies. First, we normalized tractography results from 28 healthy volunteers and created probabilistic maps to reduce the contribution of random errors due to noise and partial volume effects. Second, a sphere of uncertainty was defined to describe the effect of extrapolating tractography results to cortical regions, based on an assumption that the associated cortex is close to the terminal point of tractography. We used Talairach coordinates as a template [27], which allowed us to relate the identified cortical regions to Brodmann's map. In this study, associated

Brodmann's areas for the SLF, the ILF, the IFO, and the UNC are reported. In addition to these major association fibers, we also mapped the connectivity of the corticospinal tract (CST) and the corpus callosum.

5.2 Method

5.2.1 Subjects

Institutional Review Board approval was obtained for the study, and written, informed consent, including Health Insurance Portability and Accountability Act (HIPAA) compliance, was obtained from all subjects. Twenty-eight healthy adults (mean 29 ± 7.9 years old; male 17, female 11; all right handed) participated in our study.

5.2.2 Imaging

A 1.5T MR unit (Gyroscan NT, Philips Medical Systems) was used. DTI data were acquired using single-shot echo-planar imaging with sensitivity encoding (SENSE), parallel imaging factor, 2.5 [28]. The imaging matrix was 96×96 with a field of view of 240×240 mm (nominal in-plane resolution = 2.5 mm), zero-filled to 256×256 pixels. Transverse sections of 2.5 mm thickness were acquired parallel to the anterior commissure (AC)--posterior commissure (PC) line. A total of 50--55 sections covered the entire hemisphere and brain stem without gaps. Diffusion weighting was encoded along 30 independent orientations [29], and the b value was 700 mm^2/s. Five additional images with minimal diffusion weighting (b = 33 mm^2/s) were also acquired. The scanning time per dataset was approximately 6 min. To enhance the signal-to-noise ratio, imaging was repeated 3 times.

5.2.3 Data processing

The DTI datasets were transferred to a PC running a Windows platform and were processed using the custom-made software, DtiStudio (H. Jiang and S. Mori, Johns Hopkins University, http://lbam.med.jhmi.edu, and Kennedy Krieger Institute http://mri.kennedykrieger.org) [30]. All diffusion-weighted and non-diffusion-weighted images were first realigned by affine transformation using the automated image registration (AIR) program [31], in order to minimize Eddy current and potential small bulk motions that occurred during the scans. The 6 elements of the diffusion tensor were calculated for each pixel using multivariate linear fitting [2, 3]. After diagonalization, 3 eigenvalues and 3 eigenvectors were obtained. For the anisotropy map, fractional anisotropy (FA) was used [32]. The eigenvector associated with the largest eigenvalue was used as an indicator of fiber orientation. We also created averaged diffusion-weighted images (aDWI) by adding all diffusion-weighted images. This image was used to drive image registration.

5.2.4 Fiber-Tracking and ROI drawing strategy

For the 3D tract reconstruction, the fiber assignment by the Fiber Assignment by Continuous Tracking (FACT) method [9, 33] was used with an FA threshold of 0.2 and fiber angles of less than 40° between 2 connected pixels. The fiber tracking was also performed by DtiStudio. A multi-ROI approach was used to reconstruct tracts of interest [8, 34], which exploits existing anatomical knowledge of tract trajectories. Tracking was performed from all pixels inside the brain (brute-force approach), and results that

penetrated the manually defined ROIs were assigned to the specific tracts associated with the ROIs. The ROI placement followed the protocols described in our previous paper [35]. In this study, we reconstructed and studied 7 white matter tracts: the forceps major (FMa), the forceps minor (FMi), the medial corticospinal tract (mCST), the IFO, the ILF, the SLF, and the UNC.

5.2.5 Normalization

We used our stereotaxic white matter atlas in Talairach coordinates (JHU-Talairach atlas) as a template (downloadable from http://lbam.med.jhmi.edu/ or http://mri.kennedykrieger.org/). This template was created by transforming the JHU white matter atlas [7, 13] into the Talairach coordinate. For the transformation, the brain dimensions (width, height, and length) and the following 5 landmarks were used: 2 landmarks at the AC and PC at the midsagittal level and an additional 3 landmarks at the anterior, superior, and posterior edge of the genu, body, and splenium of the corpus callosum, respectively. These dimensions were transformed to those of the Talairach brain using trilinear interpolation. The atlas contains various DT images, including a non-diffusion-weighted image (b0 image), aDWI (average of all diffusion-weighted images), an FA map, color maps, and a T1-weighted image. For the normalization of the data from 28 volunteers, a 12-mode affine transformation was used between the 2 aDWIs; one from the JHU-Talairach atlas and the other from the subject. The tractography was performed in the native subject space, and the affine transformation matrix was applied to the tract coordinates.

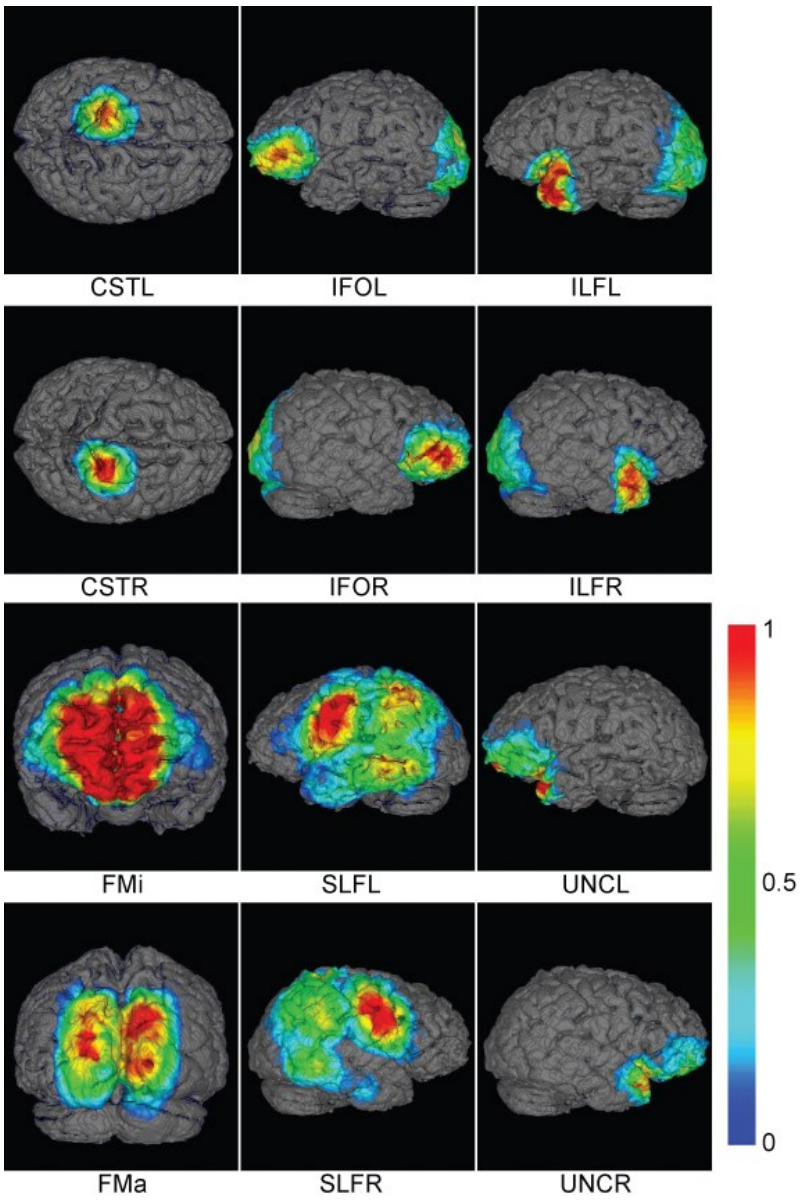

Fig. 5.1: Probability mapping of cortical areas associated with the CST, IFO, ILF, FMa, FMi, SLF, and UNC. The color represents probability as indicated by the color bar, where ‘‘1’’indicates 100% reproducibility (all 28 subjects have a connection to the pixel). L and R attached to the abbreviated tract names indicate left and right hemisphere. Abbreviations are: CST: cortitospinal tract; FMa: forceps major; FMi: forceps minor; IFO: inferior fronto-occipital fasciculus; SLF: superior longitudinal fasciculus; and UNC: uncinate fasciculus.

5.2.6 Cortical mapping

The brain surface was generated from the aDWI of the JHU-Talairach brain using a marching cube algorithm [36]. To determine which cortical areas were associated with a specific fiber bundle, a 10-mm diameter sphere was added at the end of each individual tracking result (the end of the tracking served as the center of the sphere). The intersection of the sphere and the brain surface was determined, and the coordinates were recorded as a binary mask (1: within the sphere/0: outside the sphere) in the Talairach coordinates. The binary masks, which are 3D matrices with the same dimension as the JHU-Talairach atlas (246×246×121), were obtained from the 28 normal subjects, and probabilistic maps were calculated for each tract by simply superimposing the 28 binary masks. In this probabilistic map, a pixel with, for example, a value of 0.5 means: 1) this pixel locates at the surface of the brain defined in the JHU-Talairach atlas and 2) 50% of the normal population (i.e., in 14 subjects out of 28) this pixel would be associated with the tract of interest.

5.3 Result

Figure 5.1 shows the results of cortical connectivity maps of white matter tracts, including 4 major association tracts (IFO, ILF, SLF, and UNC), the mCST, and commissural fibers (the FMa and FMi). The data indicate that the 4 association tracts connect all 4 cortical lobes namely, frontal-parietal (SLF), frontal-occipital (IFO), frontal-temporal (UNC), parietal-occipital (SLF), parietal-temporal (SLF, ILF), and occipital-temporal (ILF). The mCST clearly labels the motor cortex, although connectivity of the lateral regions could not be detected. As expected, the symmetric

regions of the brain are connected by the FMa and FMi that penetrate the splenium and genu of the corpus callosum, respectively. Figure 5.2 shows the Talairach coordinates of 3 cortical regions connected with high probability by the SLF. These regions are identified as areas 22 (Wernicke's area), 44 (Broca's area), and 40 (supramarginal gyrus). Table 5.1 lists the cortical regions associated with the 4 association fibers with high probability, together with Brodmann's areas as read from the Talairach atlas. For the SLF, UNC, and ILF, which are related to the temporal lobe, the left hemisphere consistently shows a higher probability than the right hemisphere, whereas the IFO is more symmetric. This result agrees with our previous report, in which the volumes of reconstructed fibers are significantly higher in the left hemisphere for these 3 association fibers [35]. For the SLF, the cortical areas with the highest probability are the areas 3 and 4, which are a part of the somatosensory cortex and motor cortex, respectively. Interestingly, probability in this area is highly symmetric. The rest of the areas are dominated by the language-related areas (areas 20, 21, 40, and 44) with significant dominance in the left hemisphere.

5.4 Discussion

Because of the imaging resolution of DTI (currently 2.5 mm), tract reconstruction does not reveal cellular-level connectivity information for the brain. However, it is of great interest to investigate cortical areas that are proximal to the terminal of well-known large axonal bundles assuming that these areas are associated with these bundles (tracts). To address the issue that tracking often terminates before reaching the cortex, we used a sphere of uncertainty and determined the intercept between the sphere and the cortex. Because results in individual subjects may be influenced differently by noise, and

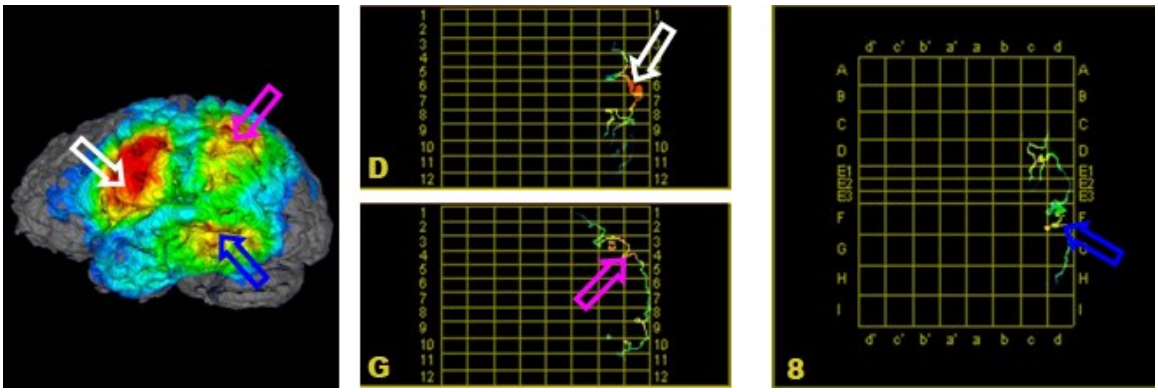

Fig. 5.2: Probabilistic connectivity map of the SLF in Talairach coordinates. Two coronal slices (Talairach coordinate coronal slices D and G) and 1 axial slice (Talairach coordinate axial slice 8) are extracted at the locations indicated by white, pink, and blue arrows, respectively. The high probability regions correspond to Brodmann's areas 44 (white arrow: Broca's area), 40 (pink arrow: supramarginal gyrus), and 22 (blue arrow: Wernicke's area).

especially partial volume effects, we created a population average. The resultant probability maps represent group-averaged coordinates of the cortices reached by fiber tracking, which are influenced by measurement reproducibility, anatomical variability, and registration quality. It is widely known that the cortical areas cannot be accurately registered by affine transformation used in this study. Therefore, the degree of probability strongly reflects variability of cortical anatomy among individuals, and it should not be confused as "connectivity strength." Tractography results also contain false positives and negatives depending on the complexity of tract architecture. Nonetheless, it is encouraging that our tractography-based cortical mapping of the SLF could identify the 3 major language areas: Wernicke's area, Broca's area, and the supramarginal gyrus. Our group-based quantitative results are in line with previous publications [6, 37-39], in

which the SLF was found to have several major branches associated with these cortical areas.

The neuroanatomical tracer-based studies have provided a wealth of information on the connectivity between different regions in the monkey brain [40-43]. In the human brain, however, connectivity has been examined by gross dissection, lesion-degeneration, and myelin histology of the postmortem tissues [44]. With these methods, there is no certainty in identifying one-to-one neural connectivity, and comparisons with animal neuranatomy provide the best model to illustrate the observations made in the human brain. Whereas a large body of such evidence suggests that there are more similarities than dissimilarities in the brain connectivity between different species, other studies indicate that certain tracts may be somewhat different [44, 45].

One example is the IFO that connects the frontal lobe and occipital lobe. The precise trajectory or even the existence of IFO has been questioned in the human brain because of the erroneous characterization of this tract in earlier studies due to the inclusion of subcallosal fibers (for its history, see [44]). The majority of the DTI studies support the traditional view of the connectivity pattern between the frontal lobe and the occipital lobe in humans [13, 43, 46]. Using the probability mapping of cortical areas associated with the IFO, the current study also suggests the presumed extremities of the IFO in the occipital lobe and frontal lobe (Fig. 5.1).

The SLF, historically regarded as a single bundle and synonymous to arcuate fasciculus (AF) in the human [47, 48], has been found to be a collection of 4 tracts comprising SLF-I, SLF-II, SLF-III, and AF [38]. The latter conceptualization of SLF and AF in humans is in agreement with isotope studies in monkeys [49-51]. These tracts are

bidirectional, and the connectivity patterns are similar between the human [38] and the monkey [52]. SLF-I connects the superior parietal lobe (area PE) with the superior frontal lobe (areas 6, SMA, and 9) corresponding to the premotor/supplementary motor cortex and prefrontal cortex. SLF-II, considered the major part of SLF, connects the parietal cortex (areas PG and PO) with the frontal eye field (area 8), premotor cortex (area 6), and prefrontal cortex (area 46). SLF-III situates ventrally connecting the inferior parietal lobe (areas PF and PFG) with the premotor and dorsolateral prefrontal cortex (Brodmann's areas 6, 44, and 46). AF connects the superior temporal gyrus with the frontal eye field (area 8) and dorsal prefrontal cortex (area 46).

In the monkey study, area 9 (prefrontal cortex) has been included in addition to area 46 (prefrontal cortex) as the connection site for SLF, and this subtle difference with the human study appears to arise from the differences in spatial resolution in the methodologies employed in the 2 studies. Makris et al. [38] have further subgrouped the vertical portion of AF as AFV, interpreting AF more distinct from the rest of the SLF in the human. Future improvements in spatial resolution and cross-fiber separability in DTI images may increase the body of evidence for specific connecting patterns in the human brain.

One unexpected finding is that the SLF has strong and symmetric association with area 4, the motor cortex. Several previous studies have demonstrated that there is a strong connection between the parietal lobe and the premotor cortex [15, 38, 48, 52]. This SLF-II component may account for the result. It also could be an artifact due to the close proximity of the mCST; this could be a region where the mCST and the SLF are

considerably intertwined and a part of the mCST could be mislabeled as the SLF in tractography.

For the rest of the cortical regions associated with the SLF, a strong asymmetry was observed. This could be related to the dominant hemisphere and agrees with previous studies that reported an asymmetry of the SLF [38, 53, 54]. This left dominance was also found in the tracts related to the temporal lobe; namely, the UNC and the ILF. These findings are also in line with previous publications [35, 55, 56]. This asymmetry, seen particularly in the area related to the temporal lobe, could be relevant to functional lateralization [57, 58]. The IFO, which is not related to the temporal lobe, as well as nonassociation fibers (mCST), shows a high degree of symmetry.

Although the probabilistic approach is expected to reduce the contribution of errors by partial volume effects, it is reasonable to assume that the connectivity maps presented in this study still contain systematic errors. The most apparent example is the result for the mCST, in which only connectivity to the medial regions of the motor cortex is indicated (thus, why we named mCST in this paper). This is attributed to problematic reconstruction areas where the CST and major association bundles cross; in such regions, our tractography map terminates prematurely before the trajectories reach the target cortices. Even if the reconstructed fibers could reach cortical areas, their trajectories could still contain errors due to crossing fibers along the pathways. If there are reproducible contributions of the crossing fibers, systematic shifts of target cortical areas may occur. Therefore, it is difficult to establish ground truth from this type of tractography-based connectivity study. In this respect, the tract-cortical association results shown in this work are mostly confirmatory based on the knowledge-based

tractography. If reproducible patterns of the cortical association are found, such results could be used to detect consistent differences between control and patient groups and bring our attention to relevant brain regions. The proposed approach could provide a quantitative means for such initial screening studies. In this respect, we would like to stress that this study is based on our previous multicenter efforts to setup robust protocols for tractography [35]. Given the nature of tracgraphy, which is based on pixel-by-pixel water diffusion properties, the results have dependency on adopted algorithms, threshold values, and seed pixel locations. Rigorous and robust tractography protocols are, thus, an essential first step for group-based quantitative studies. The technical framework and the stereotaxic coordinates reported in this work can be used as a guidance for such studies.

In this study, B0-susceptibility distortion of the DTI images was not corrected, which often plagues the DTI studies based on echo-planar imaging (EPI). Although the distortion was drastically reduced by the employment of the parallel data acquisition, comparison between the anatomical T2-weighted images and b0 images revealed 5-8 mm of distortion along the phase-encoding (anterior-posterior) direction at the temporal pole and the inferior frontal lobe [59]. The Talairach coordinates of fibers that involve these regions (i.e., UNC and IFO), therefore, contain this level of inaccuracy in our study.

In conclusion, we demonstrate DTI-based cortical connectivity studies for cortical regions associated with 4 major association fiber tracts, the medial part of the CST and the forcipes of the corpus callosum, which were mapped by 3D tract reconstructions. The coordinates of the associated cortical regions were obtained from 28 healthy volunteers and normalized into the Talairach coordinates to generate probabilistic maps. Results from the SLF and the CST agree with previous anatomical studies. This tool may provide

a means to quantitatively analyze abnormalities in specific white matter tracts and associated cortical regions.

Table 5.1: Table of brain regions associated with specific white matter tract[1]:

SLF					
	Left		Right		
	Mean[2]	Std[2]	Mean[2]	Std[2]	Brodmann's Area
d(d')-E2-5#	0.94	0.07	0.96	0.07	area 3, 4
d(d')-D-6*	0.90	0.11	0.69	0.20	area 44,6
d(d')-D-5*	0.87	0.13	0.71	0.21	area 44
d(d')-D-7*	0.81	0.09	0.51	0.17	area 44,6
d(d')-G-4*	0.81	0.06	0.60	0.07	area 40
c(c')-G-4*	0.81	0.13	0.61	0.00	area 40
c(c')-G-3*	0.81	0.11	0.57	0.06	area 40,7
d(d')-G-9*	0.77	0.09	0.55	0.10	area 21,37
d(d')-F-9*	0.73	0.10	0.22	0.13	area 21
d(d')-G-5*	0.69	0.11	0.62	0.08	area 40
d(d')-E2-7*	0.68	0.13	0.43	0.13	area 42
c(c')-D-8*	0.67	0.08	0.19	0.07	area 44
d(d')-G-8*	0.64	0.12	0.50	0.08	area 21
d(d')-F-8*	0.62	0.16	0.18	0.13	area 22
d(d')-D-8*	0.60	0.13	0.26	0.11	area 44
d(d')-G-6*	0.60	0.15	0.56	0.12	area 40,39
d(d')-F-5*	0.59	0.20	0.51	0.15	area 40
d(d')-G-10*	0.59	0.13	0.26	0.08	area 37
d(d')-F-6*	0.58	0.15	0.44	0.16	area 40,2
c(c')-D-5*	0.58	0.24	0.39	0.13	area 44
d(d')-F-10*	0.58	0.12	0.20	0.06	area 20
c(c')-E2-7*	0.58	0.11	0.21	0.04	area 41
c(c')-F-3*	0.53	0.19	0.26	0.09	area 40
d(d')-F-4*	0.52	0.20	0.44	0.09	area 40
d(d')-E3-9*	0.51	0.07	0.09	0.04	area 21
d(d')-E3-7*	0.50	0.13	0.25	0.06	area 42
d(d')-G-7*	0.46	0.14	0.36	0.08	area 22, 39
c(c')-H-3*	0.46	0.17	0.37	0.09	area 7
d(d')-F-7*	0.45	0.09	0.24	0.14	area 22
c(c')-H-4*	0.43	0.11	0.35	0.09	area 40, 19
d(d')-F-3*	0.43	0.14	0.40	0.11	area 40
d(d')-E3-10*	0.43	0.06	0.14	0.05	area 21
c(c')-H-5*	0.41	0.07	0.35	0.13	area 19,39
c(c')-D-4°	0.41	0.22	0.39	0.17	area 9
d(d')-H-9*	0.36	0.20	0.32	0.15	area 37

Note: *, #, o indicate left-side, right-side, and no dominance, respectively.

[1]Talairach coordinates that contain more than 200 pixels with probability higher than 35% on left hemisphere are listed. The Table entry is sorted base on mean probability value on left hemisphere.

[2]Numbers indicate mean, and standard deviation of probabilities which are calculated for the entire pixels within each Talairach coordinates.

ILF					
	Left		Right		
	Mean	Std	Mean	Std	Brodmann's area
c(c')-D-10*	0.94	0.10	0.71	0.21	area 38
c(c')-D-11*	0.91	0.06	0.77	0.11	area 38
d(d')-D-9*	0.90	0.05	0.86	0.07	area 38
c(c')-D-9*	0.78	0.22	0.64	0.22	area 38
c(c')-D-12*	0.71	0.12	0.51	0.19	area 38
b(b')-H-10	0.66	0.16	N/A	N/A	area 19
c(c')-C-10*	0.66	0.31	0.33	0.21	area 47
d(d')-D-8*	0.64	0.21	0.42	0.22	area 44
b(b')-I-10*	0.62	0.17	0.48	0.06	area 18
b(b')-I-6*	0.59	0.07	0.54	0.06	area 19
c(c')-E1-9*	0.58	0.25	0.45	0.20	N/A
c(c')-D-8*	0.58	0.28	0.27	0.15	area 44
c(c')-I-10*	0.55	0.18	0.42	0.08	N/A
c(c')-I-6*	0.53	0.12	0.28	0.07	area 19
c(c')-I-7*	0.52	0.09	0.35	0.08	area 19
d(d')-E1-9°	0.49	0.27	0.48	0.21	area 21
b(b')-I-5°	0.45	0.11	0.43	0.08	area 19
a(a')-I-9#	0.45	0.12	0.54	0.13	area 18, 17
c(c')-H-10*	0.44	0.15	0.24	0.07	area 19
b(b')-D-11*	0.44	0.18	0.18	0.10	area 38
c(c')-I-9*	0.43	0.14	0.37	0.06	area 18
c(c')-I-5*	0.40	0.13	0.20	0.06	area 19
c(c')-I-8*	0.39	0.09	0.36	0.08	area 18
c(c')-C-9*	0.39	0.26	0.18	0.12	area 47
a(a')-I-10#	0.37	0.15	0.45	0.15	area 18
b(b')-D-12*	0.36	0.15	0.15	0.10	area 38

IFO					
	Left		Right		
	Mean	Std	Mean	Std	Brodmann's area
c(c')-B-8#	0.84	0.05	0.93	0.05	area 46
c(c')-C-8#	0.77	0.10	0.88	0.06	area 45
a(a')-A-9*	0.75	0.13	0.35	0.21	area 10
b(b')-A-9*	0.70	0.08	0.58	0.10	area 10
c(c')-B-9#	0.69	0.13	0.81	0.08	area 10
b(b')-A-8*	0.66	0.09	0.48	0.11	area 10
b(b')-I-10*	0.65	0.15	0.46	0.17	area 18
b(b')-I-6°	0.63	0.09	0.64	0.11	area 19
c(c')-B-7#	0.61	0.18	0.69	0.21	area 46
a(a')-I-9#	0.54	0.11	0.78	0.09	area 18
c(c')-C-9#	0.52	0.18	0.66	0.12	N/A
b(b')-B-9#	0.52	0.22	0.62	0.08	N/A
a(a')-I-10#	0.52	0.19	0.64	0.16	area 18
a(a')-A-8*	0.51	0.20	0.14	0.08	area 10
c(c')-I-7*	0.50	0.16	0.27	0.12	area 18
b(b')-I-5#	0.46	0.12	0.63	0.10	area 19
c(c')-I-6*	0.45	0.16	0.28	0.12	area 19
c(c')-I-10*	0.44	0.11	0.27	0.09	N/A
b(b')-H-10	0.41	0.20	N/A	N/A	area 18

UNC					
	Left		Right		
	Mean	Std	Mean	Std	Brodmann's area
c(c')-D-10#	0.81	0.19	0.85	0.11	area 38
c(c')-C-10*	0.79	0.18	0.64	0.21	area 38
a(a')-A-9*	0.73	0.16	0.30	0.14	area 10
c(c')-D-9#	0.54	0.19	0.63	0.26	area 38
c(c')-C-9*	0.53	0.13	0.33	0.19	area 47
b(b')-A-9*	0.53	0.16	0.27	0.13	area 10
c(c')-B-8*	0.50	0.05	0.19	0.07	area 10
b(b')-D-10*	0.48	0.32	0.42	0.27	area 38
c(c')-B-9*	0.46	0.08	0.25	0.08	area 10
b(b')-B-9°	0.44	0.17	0.43	0.15	N/A
c(c')-C-8*	0.42	0.07	0.11	0.07	area 45
c(c')-D-11*	0.42	0.34	0.34	0.26	area 38
b(b')-A-8*	0.41	0.09	0.12	0.06	area 10
a(a')-A-8*	0.41	0.15	0.11	0.04	area 10
b(b')-C-10*	0.40	0.31	0.33	0.15	area 47

5.5 References

1. Moseley, M.E., et al., *DIFFUSION-WEIGHTED MR IMAGING OF ANISOTROPIC WATER DIFFUSION IN CAT CENTRAL-NERVOUS-SYSTEM.* Radiology, 1990. **176**(2): p. 439-445.

2. Basser, P.J., J. Mattiello, and D. LeBihan, *Estimation of the effective self-diffusion tensor from the NMR spin echo.* J. Magn. Reson. B, 1994. **103**: p. 247-254.

3. Basser, P.J., J. Mattiello, and D. Le Bihan, *MR diffusion tensor spectroscopy and imaging.* Biophys. J., 1994. **66**: p. 259-267.

4. Makris, N., et al., *Morphometry of in vivo human white matter association pathways with diffusion-weighted magnetic resonance imaging.* Annals of Neurology, 1997. **42**(6): p. 951-962.

5. Pajevic, S. and C. Pierpaoli, *Color schemes to represent the orientation of anisotropic tissues from diffusion tensor data: Application to white matter fiber tract mapping in the human brain.* Magnetic Resonance in Medicine, 1999. **42**(3): p. 526-540.

6. Catani, M., et al., *Virtual in vivo interactive dissection of white matter fasciculi in the human brain.* Neuroimage, 2002. **17**(1): p. 77-94.

7. Mori, S., et al., *MRI atlas of human white matter*. 2005, Amsterdam, The Netherlands: Elsevier.

8. Conturo, T.E., et al., *Tracking neuronal fiber pathways in the living human brain.* Proceedings of the National Academy of Sciences of the United States of America, 1999. **96**(18): p. 10422-10427.

9. Mori, S., et al., *Three-dimensional tracking of axonal projections in the brain by magnetic resonance imaging.* Annals of Neurology, 1999. **45**(2): p. 265-269.

10. Basser, P.J., et al., *In vivo fiber tractography using DT-MRI data.* Magnetic Resonance in Medicine, 2000. **44**(4): p. 625-632.

11. Poupon, C., et al., *Regularization of diffusion-based direction maps for the tracking of brain white matter fascicles.* Neuroimage, 2000. **12**(2): p. 184-195.

12. Parker, G.J.M., et al., *Initial demonstration of in vivo tracing of axonal projections in the macaque brain and comparison with the human brain using diffusion tensor Imaging and fast marching tractography.* Neuroimage, 2002. **15**(4): p. 797-809.

13. Wakana, S., et al., *Fiber Tract-based Atlas of Human White Matter Anatomy.* Radiology, 2004. **230**: p. 77-87.

14. Carpenter, M., *Human neuroanatomy*. 1976, Baltimore: Williams & Wilkins.

15. Nieuwenhuys, R., J. Voogd, and C. van Huijzen, *The human central nervous system*. 1983: Springer-Verlag.

16. Nolte, J. and J.B. Angevine, *The human brain: In photographs and Diagrams*. 2000, St. Louis: Mosby.

17. Friedman, D.P. and E.A. Murray, *THALAMIC CONNECTIVITY OF THE 2ND SOMATOSENSORY AREA AND NEIGHBORING SOMATOSENSORY FIELDS OF THE LATERAL SULCUS OF THE MACAQUE.* Journal of Comparative Neurology, 1986. **252**(3): p. 348-373.

18. Jones, E.G., et al., *MIDBRAIN, DIENCEPHALIC AND CORTICAL RELATIONSHIPS OF BASAL NUCLEUS OF MEYNERT AND ASSOCIATED STRUCTURES IN PRIMATES.* Journal of Comparative Neurology, 1976. **167**(4): p. 385-&.

19. Mesulam, M.M., et al., *LIMBIC AND SENSORY CONNECTIONS OF INFERIOR PARIETAL LOBULE (AREA PG) IN RHESUS-MONKEY - STUDY WITH A NEW METHOD FOR HORSERADISH-PEROXIDASE HISTOCHEMISTRY.* Brain Research, 1977. **136**(3): p. 393-414.

20. Cavada, C. and P.S. Goldmanrakic, *POSTERIOR PARIETAL CORTEX IN RHESUS-MONKEY .1. PARCELLATION OF AREAS BASED ON DISTINCTIVE LIMBIC AND SENSORY CORTICOCORTICAL CONNECTIONS.* Journal of Comparative Neurology, 1989. **287**(4): p. 393-421.

21. Newman, H.M., R.T. Stevens, and A.V. Apkarian, *Direct spinal projections to limbic and striatal areas: Anterograde transport studies from the upper cervical spinal cord and the cervical enlargement in squirrel monkey and rat.* Journal of Comparative Neurology, 1996. **365**(4): p. 640-658.

22. Paxinos, G., *The rat nervous system*. 3rd ed. 2004, Amsterdam ; Boston: Elsevier Academic Press. xvii, 1309 p.

23. Hermoye, L., et al., *Pediatric diffusion tensor imaging: Normal database and observation of the white matter maturation in early childhood.* Neuroimage, 2006. **29**(2): p. 493-504.

24. Huang, H., et al., *White and gray matter development in human fetal, newborn and pediatric brains.* Neuroimage, 2006. **33**(1): p. 27-38.

25. Mori, S. and J.Y. Zhang, *Principles of diffusion tensor imaging and its applications to basic neuroscience research.* Neuron, 2006. **51**(5): p. 527-539.

26. Tuch, D.S., et al., *Diffusion MRI of complex neural architecture.* Neuron, 2003. **40**(5): p. 885-95.

27. Talairach, J. and P. Tournoux, *Co-planar stereotaxic atlas of the human brain. 3-Dimensional proportional system: An approach to cerebral imaging*. 1988, New York, NY: Thieme Medical.

28. Pruessmann, K.P., et al., *SENSE: sensitivity encoding for fast MRI.* Magn Reson Med, 1999. **42**(5): p. 952-62.

29. Jones, D.K., M.A. Horsfield, and A. Simmons, *Optimal strategies for measuring diffusion in anisotropic systems by magnetic resonance imaging.* Magn. Reson. Med., 1999. **42**: p. 515-525.

30. Jiang, H.Y., et al., *DtiStudio: Resource program for diffusion tensor computation and fiber bundle tracking.* Computer Methods and Programs in Biomedicine, 2006. **81**(2): p. 106-116.

31. Woods, R.P., et al., *Automated image registration: I. General methods and intrasubject, intramodality validation.* J Comput Assist Tomogr, 1998. **22**(1): p. 139-52.

32. Pierpaoli, C. and P.J. Basser, *Toward a quantitative assessment of diffusion anisotropy.* Magn.Reson.Med., 1996. **36**: p. 893-906.

33. Xue, R., et al., *In vivo three-dimensional reconstruction of rat brain axonal projections by diffusion tensor imaging.* Magn. Reson. Med, 1999. **42**: p. 1123-1127.

34. Huang, H., et al., *Analysis of noise effects on DTI-based tractography using the brute-force and multi-ROI approach.* Magnetic Resonance in Medicine, 2004. **52**(3): p. 559-565.

35. Wakana, S., et al., *Reproducibility of quantitative tractography methods applied to cerebral white matter.* Neuroimage, 2007. **36**(3): p. 630-44.

36. Schroeder, W., K. Martin, and B. Lorensen, *The visualization toolkit*. 2nd ed. 1998, Upper Saddle River, NJ: Prentice Hall PTR. xx, 645 p.

37. Mori, S., et al., *Imaging cortical association using diffusion-tensor-based tracts in the human brain axonal tracking.* Magnetic Resonance in Medicine, 2002. **47**(2): p. 215-223.

38. Makris, N., et al., *Segmentation of subcomponents within the superior longitudinal fascicle in humans: a quantitative, in vivo, DT-MRI study.* Cereb Cortex, 2005. **15**(6): p. 854-69.

39. Parker, G.J., et al., *Lateralization of ventral and dorsal auditory-language pathways in the human brain.* Neuroimage, 2005. **24**(3): p. 656-66.

40. Jones, E.G. and R.Y. Leavitt, *DEMONSTRATION OF THALAMO-CORTICAL CONNECTIVITY IN CAT SOMATO-SENSORY SYSTEM BY RETROGRADE AXONAL TRANSPORT OF HORSERADISH-PEROXIDASE.* Brain Research, 1973. **63**(DEC7): p. 414-418.

41. Jones, E.G., *POSSIBLE DETERMINANTS OF DEGREE OF RETROGRADE NEURONAL LABELING WITH HORSERADISH-PEROXIDASE.* Brain Research, 1975. **85**: p. 249-253.

42. Coulter, J.D. and E.G. Jones, *DIFFERENTIAL DISTRIBUTION OF CORTICOSPINAL PROJECTIONS FROM INDIVIDUAL CYTOARCHITECTONIC FIELDS IN MONKEY.* Brain Research, 1977. **129**(2): p. 335-340.

43. Kaas, J.H., A. Schüz, and R. Miller, *Cortical areas and patterns of cortico-cortical connections.* Cortical Areas: Unity and Diversity, 2002: p. 179-191.

44. Schmahmann, J.D. and D.N. Pandya, *The complex history of the fronto-occipital fasciculus.* Journal of the History of the Neurosciences, 2007. **16**(4): p. 362-377.

45. Petrides, M. and D.N. Pandya, *Dorsolateral prefrontal cortex: comparative cytoarchitectonic analysis in the human and the macaque brain and corticocortical connection patterns.* European Journal of Neuroscience, 1999. **11**(3): p. 1011-1036.

46. Duffau, H., et al., *New insights into the anatomo-functional connectivity of the semantic system: a study using cortico-subcortical electrostimulations.* Brain, 2005. **128**: p. 797-810.

47. Dejerine, J.J., *Anatomie des centres nerveux*. Vol. 1. 1895: Rueff.

48. Catani, M., D.K. Jones, and D.H. ffytche, *Perisylvian language networks of the human brain.* Ann Neurol, 2005. **57**(1): p. 8-16.

49. Petrides, M. and D.N. Pandya, *PROJECTIONS TO THE FRONTAL-CORTEX FROM THE POSTERIOR PARIETAL REGION IN THE RHESUS-MONKEY.* Journal of Comparative Neurology, 1984. **228**(1): p. 105-116.

50. Petrides, M. and D.N. Pandya, *ASSOCIATION FIBER PATHWAYS TO THE FRONTAL-CORTEX FROM THE SUPERIOR TEMPORAL REGION IN THE RHESUS-MONKEY.* Journal of Comparative Neurology, 1988. **273**(1): p. 52-66.

51. Schmahmann, J.D. and D.N. Pandya, *Fiber pathways of the brain*. 2006, Oxford ; New York: Oxford University Press. xviii, 654 p.

52. Schmahmann, J.D., et al., *Association fibre pathways of the brain: parallel observations from diffusion spectrum imaging and autoradiography.* Brain, 2007. **130**: p. 630-653.

53. Park, H.J., et al., *White matter hemisphere asymmetries in healthy subjects and in schizophrenia: a diffusion tensor MRI study.* Neuroimage, 2004. **23**(1): p. 213-23.

54. Nucifora, P.G., et al., *Leftward asymmetry in relative fiber density of the arcuate fasciculus.* Neuroreport, 2005. **16**(8): p. 791-4.

55. Kubicki, M., et al., *Uncinate fasciculus findings in schizophrenia: A magnetic resonance diffusion tensor imaging study.* American Journal of Psychiatry, 2002. **159**(5): p. 813-820.

56. Eluvathingal, T.J., et al., *Quantitative diffusion tensor tractography of association and projection fibers in normally developing children and adolescents.* Cerebral Cortex, 2007. **17**(12): p. 2760-2768.

57. Silani, G., et al., *Brain abnormalities underlying altered activation in dyslexia: a voxel based morphometry study.* Brain, 2005. **128**: p. 2453-2461.

58. Dorsaint-Pierre, R., et al., *Asymmetries of the planum temporale and Heschl's gyrus: relationship to language lateralization.* Brain, 2006. **129**: p. 1164-1176.

59. Huang, H., et al., *Correction of B0 susceptibility induced distortion in diffusion-weighted images using large-deformation diffeomorphic metric mapping.* Magnetic Resonance Imaging, 2008. **26**(9): p. 1294-1302.

Chapter 6

Automated Tract-Specific Quantification Using Probabilistic Atlas Based on Large Deformation Diffeomorphic Metric Mapping

6.1 Introduction

In Chapter 4, tract-specific quantification based on population-averaged tract coordinates was proposed. By performing tractography in a large number of normal subjects and normalizing the tract locations to a template space, a probabilistic map can be created and incorporated in the template brain. Patient images, such as fractional anisotropy (FA) maps can then be normalized to the template brain and the pre-defined probabilistic tract coordinates are superimposed on the FA map for automated measurements of the tract-specific FA values. The advantages of this approach are; 1) tractography is no longer necessary for each data, effectively eliminating reproducibility issues and 2) tract reconstruction is not affected by pathological conditions. The disadvantages are; 1) the pre-defined probabilistic tract coordinates do not reflect patient-specific alteration of the morphology and they are merely tools to probe the status of pixels in specific locations and 2) the results are dependent on brain registration accuracy.

The first disadvantage is an inherent limitation of this approach. In this Chapter, we attempted to enhance the usefulness of this approach by adopting a state-of-the-art non-linear registration called Large Deformation Differmorphic Metric Mapping (LDDMM). There are two stages in this approach where the accurate registration would improves the outcome. The first one is when we create the population-averaged probabilistic maps and the second one is when patient data are registered to the maps. We

first created probabilistic maps of 11 major white matter tracts. We then incorporated the probabilistic map to our white matter atlas (single-subject JHU DTI atlas, also known as Eve Atlas). The accuracy of the tools are demonstrated for normal and patient brains with severe atrophy. All tools described in this work are readily accessible by our program called DiffeoMap and RoiEditor (www.mristudo.org).

6.2 Method

6.2.1 Subjects and data acquisition

DTI scan data of Twenty-nine healthy adults (mean 29 ± 7.9 years old; male 14, female 15, all right-handed) was retrieved from the International Consortium of Brain Mapping (ICBM) DTI database. The data acquisition protocol was described in a previous publication [1].

We arbitrary selected ten AD patient data and ten normal control participant data from the AD database and the normal database, respectively. Both databases were provided by the Johns Hopkins Alzheimer's Disease Center. The database contains brains from 55 to 85 years old and was de-identified. The DTI acquisition protocol can be found in Oishi et al. [1]. Co-registered T2 weighted images were acquired along with diffusion-weighted images using a double spin echo sequence with a first echo time of 10.1ms and a second echo time of 96.0ms. The repetition time is 3,000ms.

6.2.2 Data processing

The raw diffusion-weighted images(DWIs) acquired by scanner were first transferred to a personal computer and were registered to one of the b0 images using a

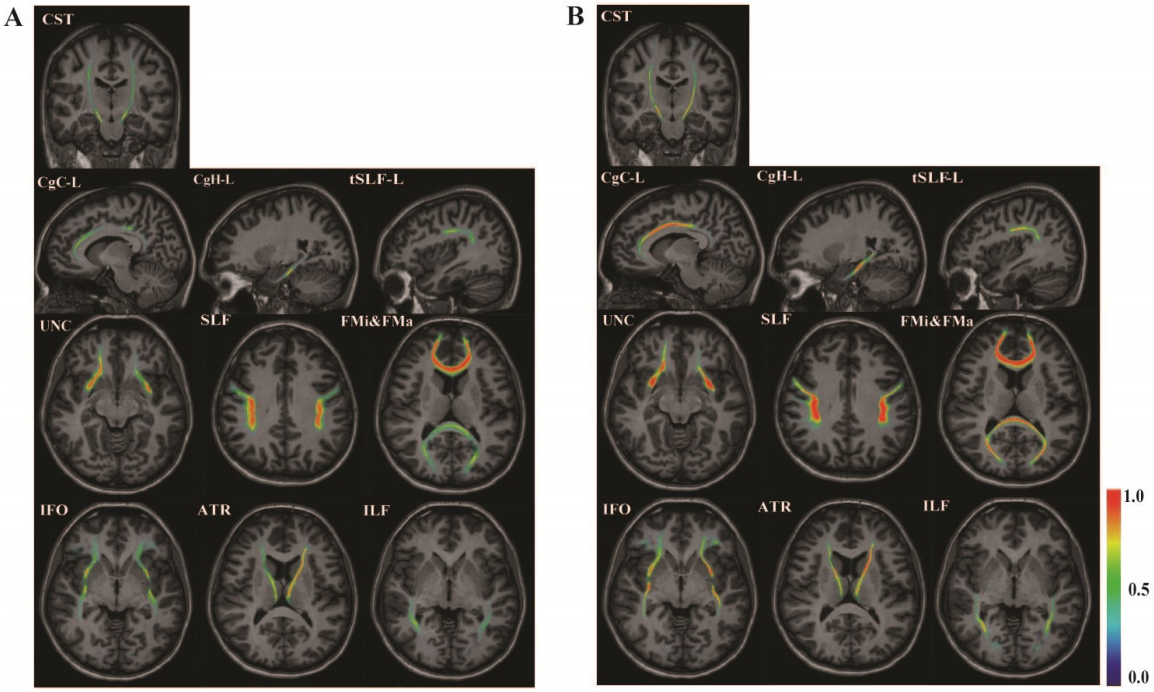

Fig. 6.1: Affine (A) and LDDMM (B) based probability map superimposed on JHU-DTI-MNI template.

12-mode affine transformation [2] to correct for bulk motion and eddy current distortion. The images were then re-sliced to 1mm isotropic resolution (181x217x181 matrix).

To correct B0-susceptibility distortion, we used LDDMM [3] to nonlinearly transformed skull-stripped b0 image to the skull-stripped T2-weighted image and the transformation was then applied to all raw DWIs. The six elements of the diffusion tensor were calculated for each pixel with multivariate linear fitting using DtiStudio [4].

6.2.3 Nonlinear normalization of subject images using LDDMM

We used the LDDMM (large-deformation diffeomorphic metric mapping) algorithm throughout this work to normalize subject images, as well as correct B0 susceptibility induced distortion. LDDMM is a state of art nonlinear normalization

algorithm that generates topology-preserving deformation, i.e. after deformation connected structures remains connected and disjoint structures remains disjoint.

Namely, for any two images $\boldsymbol{I}_0, \boldsymbol{I}_1 : \Omega \subset \mathrm{R}^3 \rightarrow R$, the LDDMM algorithm calculates the diffeomorphic transformation, $\varphi : \Omega \rightarrow \Omega$, registering the images such that $\boldsymbol{I}_1 = \boldsymbol{I}_0 \circ \varphi^{-1}$, $\Omega \subseteq R^3$ is the 3D cube on which the data are defined. The computed transformation is the end point, $\varphi = \phi_1$ of a flow of velocity fields, $v_t \in V, t \in [0,1]$, given by the ordinary differential equation:

$$\dot{\phi}_t = v_t(\phi_t) \tag{6.1}$$

where ϕ_0 is the identity transformation such that $\phi_0(x) = x, \forall x \in \Omega$. As shown by [5], enforcing a sufficient amount of smoothness on the elements in the space of allowable vector fields, V, ensures that the solution to the differential equation $\dot{\phi}_t = v_t(\phi_t), t \in [0,1]$ is in the space of diffeomorphisms. The required smoothness is enforced by defining the norm on V as $|f|_V = |Lf|_{L^2}$. L is a differential operator defined as $L = -\alpha\nabla^2 + \gamma \boldsymbol{I}_{3\times3}$, where $\boldsymbol{I}_{3\times3}$ is the identity operator and ∇^2 is the Laplacian operator. $|\cdot|_{L^2}$ is the L^2 norm for the square integrable functions defined on Ω.

Before nonlinear normalization of individual images, we applied 12-mode affine [2] transformation to bring individual image to the ICBM coordinate-based JHU-DTI-MNI atlas [1]. Each individual's Trace image was registered to JHU-T2w-MNI image using 12-mode affine and the transformation matrix was applied to individual's calculated diffusion tensor field using the method described by [6, 7]. Three eigenvalues and eigenvectors were obtained from the normalized tensor field to calculate the anisotropy, mean diffusivity (MD), etc. For the anisotropy map, fractional anisotropy (FA) was used [8]. The eigenvector associated with the largest eigenvalue was used as an indicator of

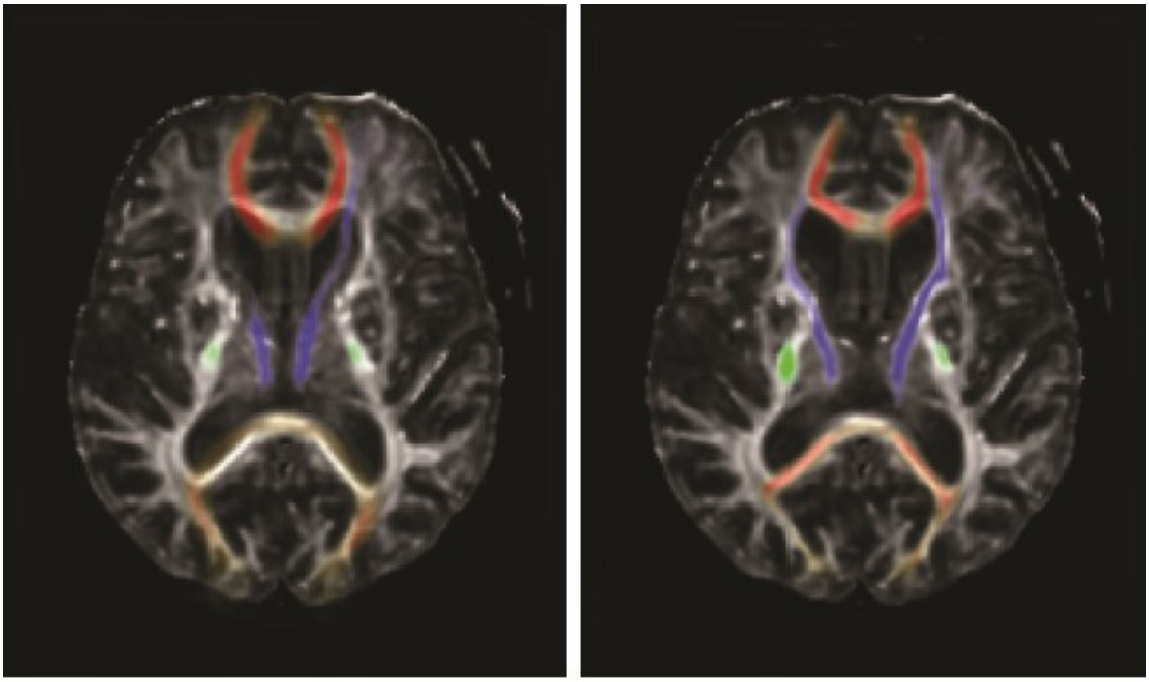

Fig 6.2: Probability maps of ATR (Blue), CST (Green), and Fmajor & Fminor(Red) transformed to a 71 years old AD patient FA image using Affine and LDDMM. The color intensity represents the probability. The abbreviations are; CST: corticospinal tract, ATR: anterior thalamic tract, Fmajor: forceps major, Fminor: forceps minor.

the fiber orientation. Tractography was performed on this normalized tensor field in ICBM coordinate.

Dual-channel LDDMM [9] was used to nonlinearly normalize each individual's data to the JHU-DTI-MNI template using linear normalized FA and B0 images simultaneously. For normal ICBM datasets, α/γ ratio of 0.005 was used. For normal aging and AD datasets, cascading α/γ ratio of 0.01, 0.002 and 0.005 was used sequentially [9]. Combined linear and nonlinear transformation was used to transform

individual's tensor field in order to minimize interpolation steps. Fractional anisotrop (FA) and mean diffusivity (MD) images, etc was calculated from the normalized tensor field.

6.1.1. Fiber tracking and ROI drawing strategy

In this study, we reconstructed the following 11 white matter tracts: forceps major (FMa); forceps minor (FMi); anterior thalamic radiation (ATR); cingulum of the cingulate cortex (CgC) and hippocampus (CgH); corticospinal tract (CST); inferior fronto-occipital fasciculus (IFO); inferior longitudinal fasciculus (ILF); superior longitudinal fasciculus (SLF); and uncinate fasciculus (Unc). There were two protocols for the SLF reconstruction – one to reveal trajectories to the frontal, parietal, and temporal lobes, and the other to select only the projections to the temporal lobe (tSLF). The Fiber Assignment by Continuous Tractography (FACT) method [10, 11] was used with a fractional anisotropy threshold of 0.2 and a principal eigenvector turning angle threshold of 40° between two connected pixels. The fiber tracking based on FACT was performed by DtiStudio [4] on the affine transformed tensor field. A multi-ROI approach was used to reconstruct tracts of interest [12, 13], exploiting existing anatomical knowledge of tract trajectories. Tracking was performed from all pixels inside the brain and fibers penetrating manually defined ROIs were assigned to the specific tracts associated with those ROIs. A description of the tracking protocol is provided in our previous papers [14-17].

6.2.4 Tract probabilistic map

Nonlinear transformation vector field obtained by LDDMM was applied to the individual's fiber tracts to transform them to the JHU-DTI-MNI template. The binarized

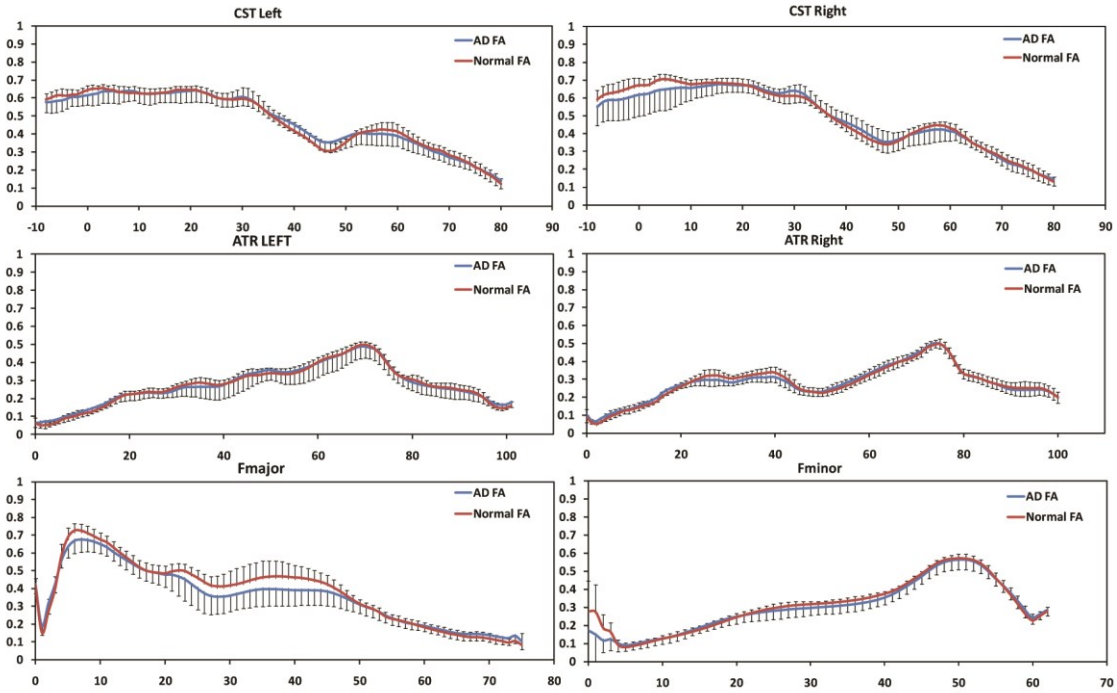

Fig 6.3: Results of tract-specific automated FA measurements along 4 major white matter tracts.

masks reporting on tract locations in the standard coordinates were averaged to generate probabilistic maps. Each voxel in the probabilistic map therefore has an assigned probability for the specific fiber tract. The JHU-DTI-MNI template and averaged fiber probability maps are available at http://lbam.med.jhmi.edu.

6.2.5 Atlas-based automated parcellation for tract-specific MR parameter quantification

The probability maps were used as template for automated white matter parcellation and to quantify MR parameters. The method was described in our previous publication [18]. Specifically, after been transformed to the standard coordinate using LDDMM as described previously, the patient data were superimposed on the probability

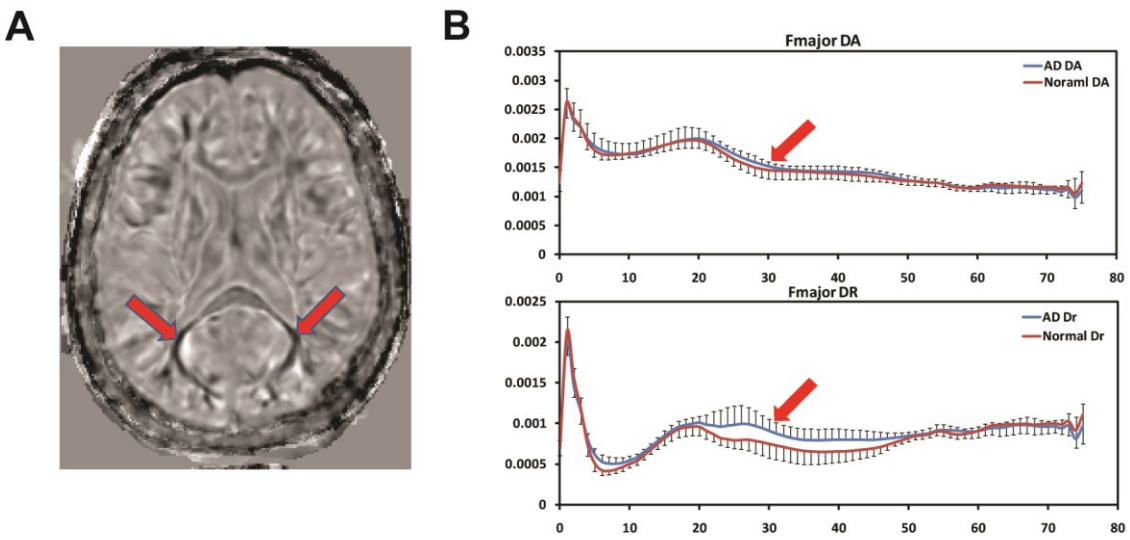

Fig 6.4: Difference between averaged FA image of AD patients and normal aging controls (A) shows hypo-intensity along Fmajor. Analysis of Axial diffusivity (DA) and radial diffusivity (DR) shows FA change is caused by increase in radial diffusivity (B).

map and the mean value of MR quantity is calculated as following:

$$\overline{\boldsymbol{M}} = \frac{\sum Pr_i \times \boldsymbol{M}_i}{\sum Pr_i} \qquad (6.2)$$

where $\boldsymbol{M}$ stands for a specific MR quantity, such as FA and Trace/3, etc. Pr_i is the probability of the ith voxel occupied by the reconstructed tract. It is empirically decided by the number of subjects with the tract occupying the ith voxel divided by the total number of subjects.

6.2.6 Automated tract-specific parcellation

The atlas-based automated parcellation method introduced in this paper was implemented in our DtiStudio:RoiEditor module (lbam.med.jhmi.edu,

godzilla.kennedykrieger.org or www.MriStudio.org), which provides a user interface for this automated tract-specific quantification. The software reports the quantification results for the entire pathways or for each image slice in the three orthogonal planes.

6.3 Result

Fig. 6.1 shows probabilistic maps of major fiber tracks, based on affine and LDDMM, respectively. The probabilistic maps are superimposed on JHU-DTI-MNI template T1 image. The probabilistic maps based on LDDMM have more hot areas (regions with high probability). Histogram (not shown) of the voxels' probability values shows that the number increases for high probability voxels and decreases for low probability voxels.

Fig 6.2 compares registration accuracy of affine and LDDMM transformation, in which several probabilistic tract maps are superimposed on a FA image of a subject with severe brain atrophy. For a subject with this amount of atrophy, normalization based on LDDMM is necessary to accurately map the pre-defined tract maps. Fig. 6.3 shows results of automated tract-specific FA quantification of CST, ATR, Fmajor, and Fminor after LDDMM transformation. The blue and red lines compare FA values of the control and AD patients along the tracts. The FA values of the two groups agree almost perfectly for each tract, except for Fmajor. Further analysis shows that the lower FA is caused by increase in radial diffusivity as shown in Fig. 6.4.

6.4 Discussion

As shown in Fig. 6.1 and Fig. 6.2, the introduction of LDDMM algorithm greatly improved our atlas-based tract-specific analysis. Firstly, it improved the quality of the probabilistic maps, especially for some association fibers, e.g. SLF and UNC. The increase in high probability areas in Fig. 6.1 indicates better correspondence between voxels after registration. Secondly, as shown in Fig. 6.2, LDDMM method showed superior power in processing brain images with severe anatomical alterations. This makes our tract-specific analysis of Alzheimer's disease data possible. All in all, this new analyzing tool is expected to be a powerful automated method to quantify the status of the white matter.

Alzheimer's disease is one of the costliest maladies in the US. The current cost for this disease in the State is well above $100 billion. The cost is expected to be tripled in the next 20 years, which might put a drag on the economy. Hence, there are currently considerable efforts to improve Alzheimer's treatment and diagnosis. Clinical studies have shown that MRI can facilitate the diagnosis of Alzheimer's and evaluate treatment efficacy [19]. The most well-known features in MR image of dementia patient is the atrophy in the medial temporal lobe, especially the hippocampus and entorhinal cortex [20]. However, recent studies suggested that the development of this disease involves much complex structures than simply the gray matters in the temporal lobe. Both structural MRI (sMRI) and functional MRI (FMRI) studies have indicated that the Alzheimer's disease affects the human brain networks [21, 22].

Our results showed that, for majorities of the fiber pathways (except Fmajor) reconstructed so far, Alzheimer's patient group and normal aging group display similar averaged mean and variability in fractional anisotropy. Our current fiber tracking method

limits our ability to go further to study the connectivity networks of Alzheimer's patient and normal population. One limiting factor is that our tractography methods are based on manual delineation, which means that, to analyze thousands of connection of the human brain, the labor work of fiber tracking would be prohibitive. Furthermore, we need to define tracking protocols for each specific brain connection. These protocols are also not available and require extensive amount of work. In the next Chapter, we propose an automated fiber tracking protocol. Using this protocol, the brain network of Alzheimer's patient can be studied without a lot of labor.

6.5 References

1. Oishi, K., et al., *Atlas-based whole brain white matter analysis using large deformation diffeomorphic metric mapping: Application to normal elderly and Alzheimer's disease participants.* Neuroimage, 2009. **46**(2): p. 486-499.

2. Woods, R.P., et al., *Automated image registration: I. General methods and intrasubject, intramodality validation.* J Comput Assist Tomogr, 1998. **22**(1): p. 139-52.

3. Huang, H., et al., *Correction of B0 susceptibility induced distortion in diffusion-weighted images using large-deformation diffeomorphic metric mapping.* Magnetic Resonance Imaging, 2008. **26**(9): p. 1294-1302.

4. Jiang, H.Y., et al., *DtiStudio: Resource program for diffusion tensor computation and fiber bundle tracking.* Computer Methods and Programs in Biomedicine, 2006. **81**(2): p. 106-116.

5. Dupuis, P., U. Grenander, and M.I. Miller, *Variational problems on flows of diffeomorphisms for image matching.* Quarterly of Applied Mathematics, 1998. **56**(3): p. 587-600.

6. Alexander, D.C., et al., *Spatial transformations of diffusion tensor magnetic resonance images.* IEEE Trans Med Imaging, 2001. **20**(11): p. 1131-9.

7. Xu, D., et al., *Spatial normalization of diffusion tensor fields.* Magn Reson Med, 2003. **50**(1): p. 175-82.

8. Pierpaoli, C. and P.J. Basser, *Toward a quantitative assessment of diffusion anisotropy.* Magn.Reson.Med., 1996. **36**: p. 893-906.

9. Ceritoglu, C., et al., *Multi-contrast large deformation diffeomorphic metric mapping for diffusion tensor imaging.* Neuroimage, 2009. **47**(2): p. 618-627.

10. Mori, S., et al., *Three-dimensional tracking of axonal projections in the brain by magnetic resonance imaging.* Annals of Neurology, 1999. **45**(2): p. 265-269.

11. Xue, R., et al., *In vivo three-dimensional reconstruction of rat brain axonal projections by diffusion tensor imaging.* Magn. Reson. Med, 1999. **42**: p. 1123-1127.

12. Conturo, T.E., et al., *Tracking neuronal fiber pathways in the living human brain.* Proceedings of the National Academy of Sciences of the United States of America, 1999. **96**(18): p. 10422-10427.

13. Huang, H., et al., *Analysis of noise effects on DTI-based tractography using the brute-force and multi-ROI approach.* Magn Reson Med, 2004. **52**(3): p. 559-65.

14. Mori, S., et al., *Imaging cortical association using diffusion-tensor-based tracts in the human brain axonal tracking.* Magnetic Resonance in Medicine, 2002. **47**(2): p. 215-223.

15. Stieltjes, B., et al., *Diffusion tensor imaging and axonal tracking in the human brainstem.* Neuroimage, 2001. **14**(3): p. 723-735.

16. Wakana, S., et al. *Reproducible protocol for human white matter fiber tracking and quantitative analysis of their status*. in *International Society of Magnetic Resonance in Medicine*. 2005. Miami.

17. Wakana, S., et al., *Fiber Tract-based Atlas of Human White Matter Anatomy.* Radiology, 2004. **230**: p. 77-87.

18. Hua, K., et al., *Tract probability maps in stereotaxic spaces: Analyses of white matter anatomy and tract-specific quantification.* Neuroimage, 2008. **39**(1): p. 336-347.

19. Mueller, S.G., et al., *The Alzheimer's disease neuroimaging initiative.* Neuroimaging Clinics of North America, 2005. **15**(4): p. 869-+.

20. Seab, J.P., et al., *QUANTITATIVE NMR MEASUREMENTS OF HIPPOCAMPAL ATROPHY IN ALZHEIMER-DISEASE.* Magnetic Resonance in Medicine, 1988. **8**(2): p. 200-208.

21. He, Y., Z. Chen, and A. Evans, *Structural insights into aberrant topological patterns of large-scale cortical networks in Alzheimer's Disease.* Journal of Neuroscience, 2008. **28**(18): p. 4756-4766.

22. Buckner, R.L., et al., *Cortical hubs revealed by intrinsic functional connectivity: mapping, assessment of stability, and relation to Alzheimer's disease.* J Neurosci, 2009. **29**(6): p. 1860-73.

Chapter 7

Automated cortical-cortical tractography using White Matter Parcellation Map (WMPM) and analysis of Alzheimer's disease's structural connectivity networks

7.1 Introduction

Advances in structure and functional magnetic resonance imaging have enabled us to analyze the underline brain network non-invasively [1, 2]. Technology developments was accelerated in last few years [3]. Currently, brain white matter connectivity was investigated using both deterministic [4, 5] and probabilistic [6] tractography; consistent functional connectivity patterns were observed in resting-state functional MRI [1, 7]. Importantly, there are recent evidences suggesting that the functional connectivity patterns may coincide with the spatial distribution of some pathological conditions [8-10]. These advancements warrant the development of network-based analysis of human brain connectivity, in which white matter connectivity study may play a crucial role.

White matter connectivity network can be investigated using fiber assignment by continuous tracking (FACT) based multiple ROI approach [2, 11], which has produced consistent results on normal subjects [12]. However, ROI placement needs trained personnel with expert anatomical knowledge. Moreover, drawing multiple ROIs is labor intensive, thus rendering it difficult to systematically investigate the brain network. Automatic methods to place ROIs using a common template ROI sets have been

proposed [13, 14]. These methods avoid manually placing ROIs and are more suitable for automated computational analysis of connectivity.

Currently, many white matter network analysis methods were proposed. Some group fibers by its proximity to the automatic segmented human brain parcellation map [5, 15]. In these approaches, the human brain parcellation map is created using a high-resolution T1 image. The parcellation map is inversely transformed to the diffusion-weighted image by using transformation matrix that co-registers T1 image with diffusion-weighted image. Fiber pathways that end within a pre-defined distance from the parcellation map are identified as connective pathway. Similar approaches [16, 17] are applied on Diffusion Spectrum Imaging (DSI). Multiple numbers of fibers are initiated from voxels in the human brain. A connection is determined if a fiber is ended in a pair of ROIs. Using these approaches people have shown that the complex human brain network has small-world topology, which consists of highly connected hubs [16, 18-20]. Notably, Alzheimer's patients was found to have disrupted brain white matter network topology [21].

In this study, we use white matter parcellation map [22] and Large Deformation Diffeomorphic Metric Mapping (LDDMM) [23, 24] to automatically build the cortico-cortical connectivity map. The subject image was first co-registered to the JHU white matter atlas template space [22] using multi-contrast Large Deformation Diffeomorphic Metric Mapping (LDDMM) [23]. The white matter parcellation map is then transformed to the subjects' space using inversed transformation matrix. Because the LDDMM transformation is diffeomorphic, the topological relationships between the parcels are preserved, i.e. connected parcels remain connected after transformation. The current

white matter atlas [22] includes twenty-four cortical ROIs on each side of the brain. For the forty eight cortical ROIs, 1128 potential connections are investigated simultaneously. Brute-force tractography [25, 26], which is less sensitive to partial volume effect, is employed for whole brain fiber tractography. Connections between cortical areas are exhaustively searched. This tracking protocol is tested on a balanced data set of AD patients and age-matched controls. Statistical significant differences are found on several connective pathways.

As in many neuroimage studies, the automated cortical-cortical tracking pipeline creates datasets in high dimensional space (thousands of potential connections for each subject). To reveal the information underline these multivariate datasets, dimension reduction and pattern classification methods could be employed. Lately, machine learning methods are increasingly adopted in neuroimaging research [27-31]. Support vector machine [32, 33] is one of the most employed multivariate pattern analysis methods for disease pattern classification [29, 30, 34-37]. Particularly, support vector machine has been used to classify dementia patient using gray matter features derived from high-resolution T1 images [29, 34, 36]. This study implemented the support vector machine classifier (SVC), using integrated fractional anisotropy (FA) along the connective pathway as the classifier input. Gaussian radial basis function was chosen as the kernel function to map the data to higher dimensional feature space for classification. Furthermore, since feature selection step has proven can improve classification performance [38], a hybrid method of feature filtering and SVC was employed to select most discriminative subset of features.

Compared to thousands of potential connective pathways, the number of subjects included in this study is limited. Leave-one-out cross-validation (LOOCV) was employed to estimate the classifier's generalization ability. Furthermore, the classifier's performance was assessed by permutation test. In permutation test, the class labels were randomly assigned to subjects, under the null hypothesis that the feature and class labels are independent. If the classifier can perform better-than-random classification on subjects with true labels, it is likely the classifier indeed captures the structure differences among the two populations.

7.2 Method

7.2.1 Participants

The image datasets were drawn from our existing database of normal control and AD patients. The images were acquired for a study conducted by the Johns Hopkins Alzheimer's Disease Research Center (ADRC). Every individual enrolled in this study has given written informed consent in accordance with the requirements of the Johns Hopkins Institutional Review Board and the guidelines endorsed by the Alzheimer's Association (2004). Seventeen patients (mean age: 73.24, Male: 14, Female: 3), who met NINCDS/ADRDA criteria for AD [39], and eighteen normal age-matched controls (mean age: 76.16, Male: 8, Female: 10) were included in this study. The detailed demographic, health and clinical information for this cohort were described in previous report [40].

7.2.2 Clinical evaluations

Several clinical evaluations were performed at the time of baseline MRI scan by trained ADRC staff, and include CDR, the Alzheimer's Disease Assessment Scale (cognitive portion-ADAS-cog) [41], the Mini Mental State Examination (MMSE) [42], and the Wechsler Memory Scale, third edition (WMS-III) [43].

7.2.3 MRI Acquisition

DTI were acquired using single-shot echo-planar imaging sequences with sensitivity encoding and a parallel imaging factor of 2.0 [44]. The imaging matrix is 96x96x96, with a field of view of 212x212mm, zero-filled to 256x256mm. Transverse sections of 2.2mm thickness were acquired parallel to the anterior commissure-posterior commissure line. A total of 50-60 sections covered the entire hemisphere and brainstem without gaps. Diffusion weighting was encoded along 30 independent orientations [45], and the b-value is 700 s/mm^2. Five additional images with minimal diffusion weighting (b=33mm^2/sec) (b0 images) were also acquired. The scanning time per dataset is approximately four minutes. Co-registered double-echo fast spin echo (DE-FSE) images were acquired using a double spin echo sequence with a first echo time of 10.1ms, a second echo time of 96.0ms, and a repetition time of 3,000ms. The image matrix is 256x247, with a field of view of 240x210mm, zero-filled to 256x256mm. Axial slices of 3mm thickness were acquired parallel to the anterior-posterior commissure line. A total of 48 slices covered the entire brain and brainstem without gaps.

All the above images were acquired on a 3.0 Tesla (3T) scanner (Philips Medical Systems, Best, The Netherlands) at the F.M. Kirby Research Center for Functional Brain

Imaging at the Kennedy Krieger Institute. A Magnetization Prepared Rapid Gradient Recalled Echo (MPRAGE) scan was also acquired according to the protocol of the Alzheimer's Disease Neuroimaging Initiative (ADNI) [46]. However, the detailed description is not included here.

7.2.4 DTI Image Processing

The diffusion-weighted images (DWI) were first co-registered to one of the b0 images to correct for subject motion and eddy-current distortion using a 12-mode affine transformation with the Automated Image Registration (AIR) [47]. The images were then re-sliced to 1mm isotropic resolution (181x217x181 matrix). The b0 image was co-register to the T_2-weighted image acquired by DE-FSE [48], using Large Deformation Diffeomorphic Metric Mapping (LDDMM). The transformation map was subsequently applied to all diffusion-weighted images.

7.2.5 DTI Image Normalization and Automated Tractography using Large Deformation Diffeomorphic Metric Mapping (LDDMM)

The T2-weighted image was first skull stripped and then co-registered with the JHU template T2-weighted image using 12-mode affine transformation with Automated Image Registration (AIR). The transformation matrix was applied on the DTI image such that the brain volumes are grossly adjusted. The fractional anisotropy (FA), mean diffusivity (MD) and the principal eigenvectors were obtained from the transformed DTI image using DTIStudio (www.Dtistudio.com) [49]. The fractional anisotropy (FA) image and mean diffusivity (MD) image were used to drive the co-registration of DTI image to

the JHU White Matter Atlas, using dual-channel LDDMM [23]. The deformation map was inversed and applied on the white matter parcellation map defined on the Atlas space. For each subject, brute-force white matter tractograpy [25, 26] was employed. After the white matter parcellation map was transformed to the subject space, the fiber pathways that connecting cortical parcels are exhaustively searched. For each pair of parcels, the connective fiber pathways are chosen according to the following criteria.

1) The fiber either last exits from or ends in these two parcels.
2) The FA value for fiber extremities is less than 0.3.

7.2.6 Feature Ranking

In this study, the integrated fractional anisotropy (FA) value along the connective pathways was used as input for the classifier. Since there are 1128 potential connections, subjects were represented as vectors contain 1128 entries. Each entry corresponds to the integrated FA value of one connection. In the feature ranking process, the input values were ranked according to its contribution to the subject classification. There are few measures that can rank and select features [50]. T-test and Fisher criterion are examples of the often used measures.

Here, we choose F-score proposed by Chen et. al. [51], which is defined as following:

$$F(j) = \frac{\left(\bar{x}_j^{AD} - \bar{x}_j\right)^2 + \left(\bar{x}_j^{NC} - \bar{x}_j\right)^2}{\frac{1}{n^{AD}-1}\sum_{i=1}^{n^{AD}}\left(x_{i,j}^{AD} - \bar{x}_j^{AD}\right)^2 + \frac{1}{n^{NC}-1}\sum_{i=1}^{n^{NC}}\left(x_{i,j}^{NC} - \bar{x}_j^{NC}\right)^2} \qquad (7.1)$$

where $\bar{x}_j$, $\bar{x}_j^{AD}$, $\bar{x}_j^{NC}$ are the average of the jth feature of the total subjects, AD subjects, normal subjects, respectively. $x_{i,j}^{AD}$ and $x_{i,j}^{NC}$ are jth feature of the ith AD and normal subject respectively. n^{AD} and n^{NC} are number of AD and normal subjects, respectively. The nominator and denominator of the F-score are the sum of inter-class variance and the sum of within-class variance for the jth feature, respectively. The larger the F-score is, the better these two populations are discriminated by this feature.

7.2.7 Support Vector Classification

Suppose each subject is represented as a multi-dimensional vector x_i and y_i is the corresponding class label (1 for Normal Control and -1 for AD patient, for example). The support vector machine is to minimize the following problem [32, 52]:

Minimize

$$\Phi = \frac{1}{2} w \cdot w + C \sum_{i=1}^{l} \xi_i \tag{7.2}$$

Subject to constraints

$$y_i(x_i \cdot w + b) \geq 1 - \xi_i, \; i = 1, \ldots, l \tag{7.3}$$

$$\xi_i \geq 0, \; i = 1, \; \ldots, l. \tag{7.4}$$

Where w is the weight vector and C is the regularization paramter. ξ is a measure of misclassification error and b is a constant.

For the simple problem of linear separable data sets, support vector machine finds the hyperplane that uniquely separate the data points with the maximum margin. A margin can be geometrically interpreted as the distance of the data point from the hyperplane. For real-life applications, dataset for classification are often not linear

separable in the input space. A non-negative slack variable $\boldsymbol{\xi}$ is introduced so that we can separate the dataset with minimum error. Furthermore, the optimal hyperplane can be sought in higher dimensional space by mapping the linear non-separable dataset to a high dimensional space using a kernel function. In our study, Gaussian radial basis function was chosen as the kernel function, which is of the following form [53]:

$$\boldsymbol{K(x_i, x_j) = exp\left(-\gamma \|x_i - x_j\|^2\right)} \tag{7.5}$$

where $\boldsymbol{x_i, x_j}$ represent data point $\boldsymbol{i, j}$, respectively, and $\boldsymbol{\gamma}$ controls the size of Gaussian kernel.

The support vector classifier is implemented using the LIBSVM toolbox [54]. Parameter $\boldsymbol{C}$ and $\boldsymbol{\gamma}$ were determined by leave-one-out cross validation (LOOCV) using training data. The leave-one-out cross validation was also employed for estimating generalization error. The detailed description of leave-one-out cross validation is described below.

7.2.8 Leave-one-out Cross-Validation (LOOCV)

In supervised learning, dataset is often divided into two subsets, namely training set and testing set. The training set is used to build the decision model. The testing set is used to estimate the generalization ability of the decision model. However, for clinical applications, the size of the datasets is typically small since it is often expensive or difficult to acquire clinical data. For such problems, the model generalizability is usually evaluated by K-fold cross validation. In K-fold cross validation, the data set is randomly split into K subsets. Each time one subset is held out as the testing set. The samples from the rest K-1 subsets are used to build the decision model and the hold-out subset is used

to estimate the model generalization ability. The process repeats for K times, until all the K subsets have been the hold-out set once. The average of the performance of the K decision models gives an estimate of the overall generalization ability. One form of K-fold cross-validation is leave-one-out cross-validation (LOOCV), where only one sample is held out as the testing set.

Fig. 7.1 illustrates the leave-one-out cross-validation (LOOCV) implementation. Namely, each time one sample is selected from a total of N samples and it is used as the testing set. Features are ranked according to F-score based on the N-1 samples. The ranked features are sequentially added into an empty set. Using the sequentially added feature subset, the support vector classifier is trained on the N-1 samples. The hold-out sample is used to evaluate the generalization error. This procedure is repeated N times until all the samples have been chosen once. The generalization ability is evaluated by averaging the error rate for decision models using feature set of same size. The optimal number of features is the one that gives lowest error rate.

7.2.9 Permutation Test

It has been suggested that permutation test can be used to measure the significance of classifier result [55, 56]. In permutation test, the class labels are randomly assigned (10000 times in our study) to subjects. The classifier is trained on the subjects with permutated labels using the same number of features as for subjects with true labels. The test statistics is defined as the cross validation accuracy. A better than chance statistics implies the rejection of the null hypothesis that the class labels and the features are independent.

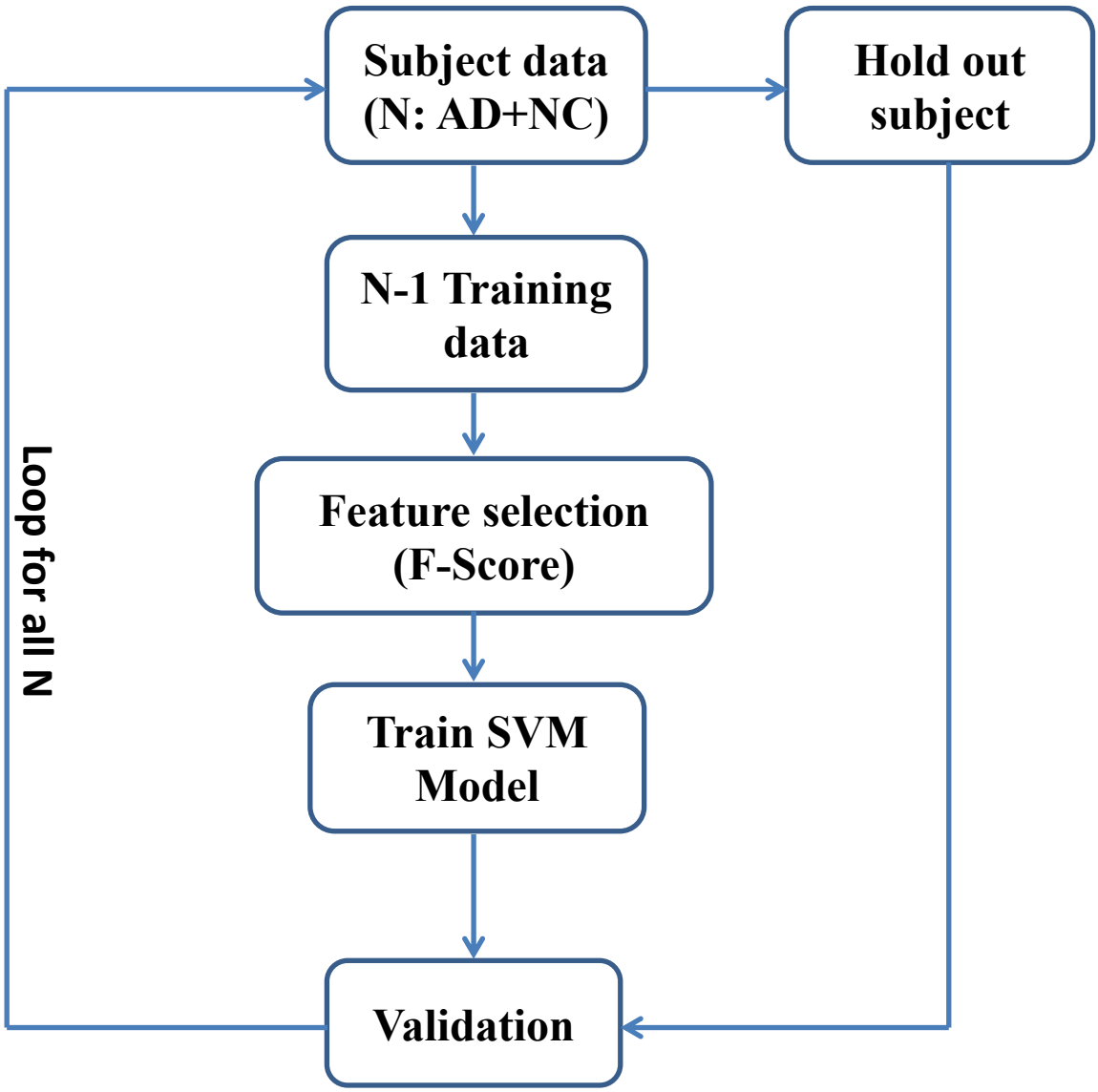

Fig. 7.1: Leave-One-Out-Cross-Validation (LOOCV).

7.3 Result

7.3.1 Fiber Tracking

For the 17 Alzheimer's dementia (AD) and 18 Normal Control subjects, 1128 potential cortical-cortical connections were simultaneously investigated on every subject.

In total, we found about 510 pathways that exist in at least one of the subjects. Between AD group and NC group, no significant differences were found in total fiber count ($p=0.57$, student-t test, two tail and equal variance).

Tracking results of AD group and NC group on the 510 connections were compared using Wilcoxon rank-sum test using fractional anisotropy (FA) value integrated along the pathways. A pixel map, where each pixel corresponds to the significance of the rank-sum test on corresponding connection, is shown in Figure 6.2. Because of the reciprocity of the connections, the pixel map is symmetric. Blue color in the pixel map represents little or no statistical significance. The color gradually changes to red as the statistical significance increases. If there is no fiber found in any of the subjects, the pixels are rendered gray. In this study, the connectivity within the parcel itself is ignored. Hence, the diagonal pixels are rendered blue.

Further analyses of the results found significant differences exist among several fiber pathways, mainly related to the temporal lobe. It is also noted that a number of pixels in the first and third quadrant are rendered gray, indicating an "under-representation" of inter-hemisphere connections. This may due to the limitations of deterministic tracking method, which is affected by the crossing fibers at places like corona radiate.

7.3.2 Classification Result

Feature selection and support vector classification method was applied to subjects with true class labels. The results indicate that using six features the support vector

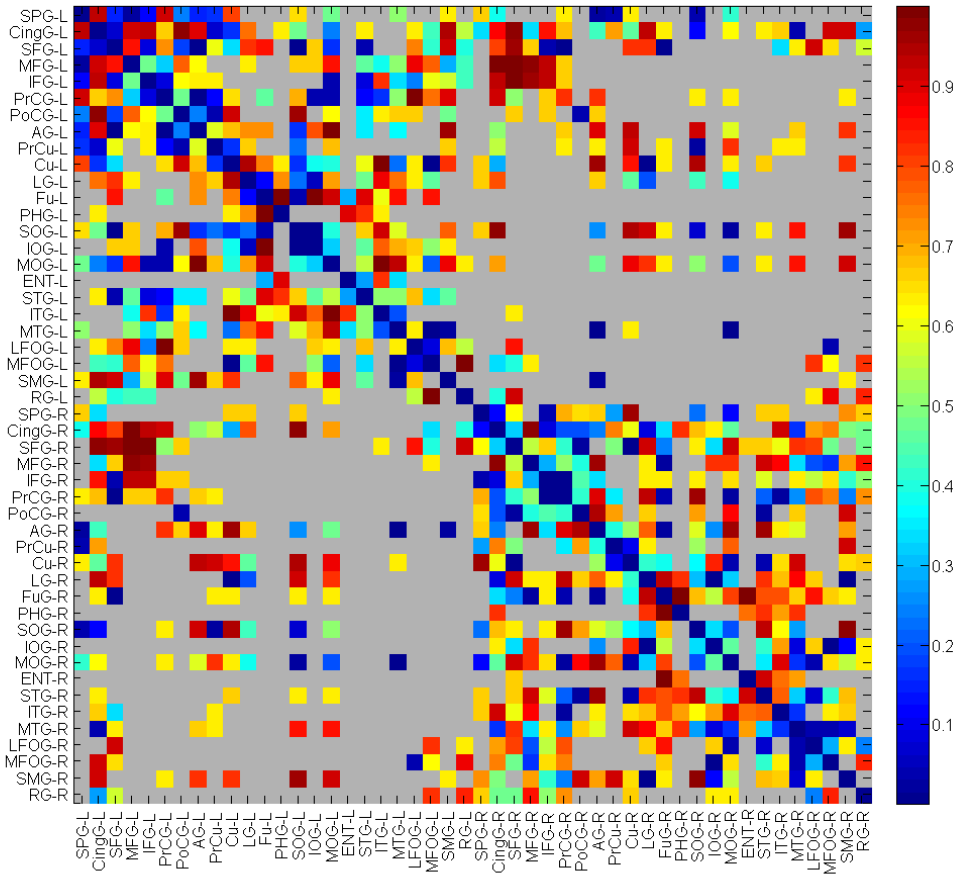

Fig. 7.2: Connectivity statistical difference map between AD and Normal. Blue represents little or no differences. The statistical difference increases with the color gradually changes to red. Gray color represents no connections in all the subjects.

machine with Gaussian kernel gives best leave-one-out cross-validation accuracy of 89%. The six features with highest F-score are shown in Figure 6.3.

7.3.3 Permutation Test

The class labels were randomly permutated for 10,000 times. The same leave-one-out cross-validation and classification pipeline was applied on subjects with

permutated labels. The generalization ability was assessed each time using six most discriminative features. The result is shown in Figure 7.4. The figure reveals that the classifier learned the structural differences between the two groups with the probability of been wrong of $p<0.0003$.

7.4 Discussion

The automated cortical to cortical fiber tracking pipeline discussed in this study employs the JHU white matter parcellation map and Large Deformation Diffeomorphic Metric Mapping (LDDMM). The Johns Hopkins white matter parcellation map is based on well-defined anatomical structure and it covers the whole brain. Almost every fiber pathway is accounted for using this set of parcels. By applying diffeomorphic transformation LDDMM, the parcels can be accurately brought to the subject space and the topology of the parcellation map is preserved. It is noted that, after transformation of the whole parcellation map to the subject space, fibers connecting two cortical ROIs are either end in or last exit (in case of mis-registration) from these two cortical ROIs. Therefore, the fiber tracking algorithm is designed to recursively check both ends of the fibers. This algorithm is easy to implement and fully automated. In order to include only fibers connecting cortical areas, a fractional anisotropy threshold was imposed such that only fibers whose ends are close to the cortex were selected.

Although the proposed cortical tracking method is pretty straight forward and fully automated, it is still subject to registration error and tracking artifacts. The purpose of this automatic pipeline is to efficiently exam and compare large cohort of datasets. Statistical significant differences found using this pipeline are evidences for further

investigation. In the end, hand segmentation is needed to validate the result, as it is still the golden standard.

The capabilities for the tracking protocol to reveal connectivity patterns are limited by image resolution, partial volume effect and the diffusion tensor model. For instance, as shown in Figure 7.2, the inter-hemisphere cortical connections are "under-represented" in the tracking result. As we tracking fibers, we also integrate errors, which may due to image noise and partial volume effect, along the pathways. Thus, long-range connective pathway tracking is more likely to give false negative result than short-range tracking. This shows the limitation of our current technology. As an alternative, probabilistic tractography [6, 57] may be able to give more information about long-range connections.

Same as other structure and resting-state FMRI connectivity studies [58-60], the parcellation strategy can play important role in the outcome of tractography and classification. The JHU white matter parcellation map contains forty-eight cortical ROIs, which are all defined based on anatomical structures. In the automated tractography, the connective fibers are grouped using the "a priori" defined groups of voxels. Thus, as in the FMRI study [60], the cortical ROIs reduce the dimensionality of the complex structure network. Instead of probably millions of voxel to voxel connections, we only study a network with little more than a thousand potential connections. Moreover, the SNR and reproducibility of the tractography results should increase as well. All in all, different parcellation strategies should lead to different degree of dimension reduction and should have distinct characteristic of SNR and reproducibility.

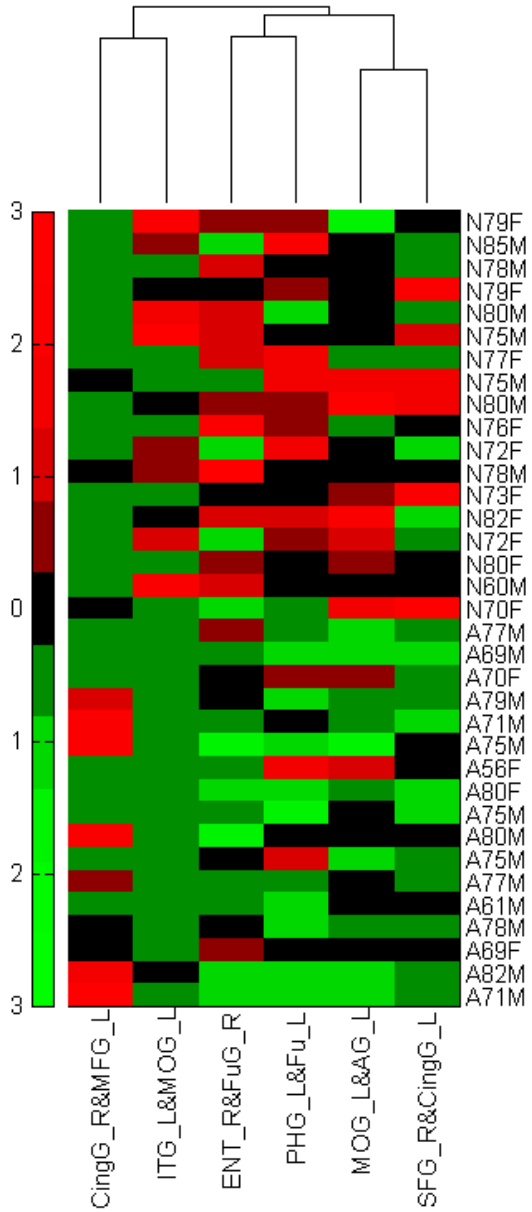

Fig. 7.3: Six selected features.

There are currently several cortical parcellation strategies available, for example the Automatic Anatomical Labeling (AAL) [15] and the Eickhoff-Zilles (EZ) atlas [61]. The Johns Hopkins white matter parcellation is unique in that it is a parcellation of the entire 3D brain and automated cortical-cortical tracking can all be realized using the same set of ROIs [13, 14]. Moreover, in this approach, we don't need another T1 scan for automatic segmentation. It is challenging to co-register T1 and diffusion tensor images. Furthermore, functional connectivity [60] and structural connectivity study can be combined in one framework. This could potentially enable us to relate functional connectivity with the structure connectivity. Nevertheless, recent studies [62] have shown that the anatomical parcellation may not be able to well characterize the functional

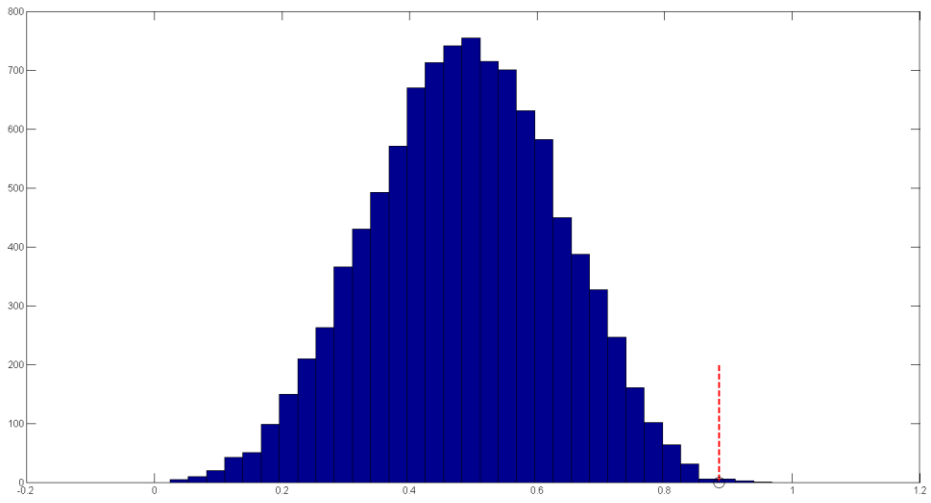

Fig 7.4: The permutation distribution of generalization rate when selecting the six most discriminating features for each repetition (repetition times: 10000). X axis represents generalization rate and Y axis represents occurrence. $p<0.0003$ with generalization rate as the statistic (Red dotted line is the generalization rate obtained with the real class labels).

network. Particularly, two anti-correlated functional networks could exist in one anatomical parcel. Hence, further refinement of the current parcellation map for functional network study may be needed.

The pattern classification analysis and permutation test indicate that the classifier indeed was able to identify structure differences between the AD group and the normal control group, with high cross-validation accuracy 88.9%. However, the classifier decision model is limited by the sample size. Compared with thousands of potential connections, our sample size is relatively small. More datasets are needed to build a more "faithful" model. In the future, it is necessary to create a database with more subjects and, if possible, conduct multi-center cross-scanner study. Including more subjects to the study will not only allow us to have enough datasets to build a more plausible decision model, but also would allow us to examine multi-modality parameters such as volume deformation, mean diffusivity, axial and radial diffusivity, etc [35].

7.5 Conclusion

This study proposes a fully automated tracking method so that the white matter cortical connectivity network can be efficiently reconstructed. Like that exemplified in long range connections, as shown in Figure 7.2, anatomical connectivity is not always evident by tractography because of limitation of our current technology. Higher resolution imaging and probabilistic tracking method may be needed to improve connectivity inference. Moreover, single subject structure connectivity study is likely contaminated by false-positive and false-negative results. By comparing normal subject group with neuro-degenerative disease group, like Alzheimer's, we are able to infer how

connectivity is affected by the disease progression. Combined it with functional connectivity studies, we could potentially obtain wealth of information about underline connectivity of the human brain and its role in neurological disease diagnosis and prognosis.

7.6 Reference

1. Greicius, M.D., et al., *Functional connectivity in the resting brain: a network analysis of the default mode hypothesis.* Proc Natl Acad Sci U S A, 2003. **100**(1): p. 253-8.
2. Mori, S., et al., *Imaging cortical association using diffusion-tensor-based tracts in the human brain axonal tracking.* Magnetic Resonance in Medicine, 2002. **47**(2): p. 215-223.
3. Toga, A.W., et al., *Mapping the human connectome.* Neurosurgery, 2012. **71**(1): p. 1-5.
4. Hua, K., et al., *Mapping of functional areas in the human cortex based on connectivity through association fibers.* Cereb Cortex, 2009. **19**(8): p. 1889-95.
5. Gong, G., et al., *Mapping anatomical connectivity patterns of human cerebral cortex using in vivo diffusion tensor imaging tractography.* Cereb Cortex, 2009. **19**(3): p. 524-36.
6. Behrens, T.E., et al., *Non-invasive mapping of connections between human thalamus and cortex using diffusion imaging.* Nat Neurosci, 2003. **6**(7): p. 750-7.
7. Fox, M.D., et al., *The human brain is intrinsically organized into dynamic, anticorrelated functional networks.* Proceedings of the National Academy of Sciences of the United States of America, 2005. **102**(27): p. 9673-9678.
8. Greicius, M.D., et al., *Default-mode network activity distinguishes Alzheimer's disease from healthy aging: evidence from functional MRI.* Proc Natl Acad Sci U S A, 2004. **101**(13): p. 4637-42.

9. Seeley, W.W., et al., *Neurodegenerative diseases target large-scale human brain networks.* Neuron, 2009. **62**(1): p. 42-52.

10. Buckner, R.L., et al., *Cortical hubs revealed by intrinsic functional connectivity: mapping, assessment of stability, and relation to Alzheimer's disease.* J Neurosci, 2009. **29**(6): p. 1860-73.

11. Mori, S., et al., *Three-dimensional tracking of axonal projections in the brain by magnetic resonance imaging.* Annals of Neurology, 1999. **45**(2): p. 265-269.

12. Wakana, S., et al., *Reproducibility of quantitative tractography methods applied to cerebral white matter.* Neuroimage, 2007. **36**(3): p. 630-44.

13. Zhang, W., et al., *Automated fiber tracking of human brain white matter using diffusion tensor imaging.* Neuroimage, 2008. **42**(2): p. 771-7.

14. Zhang, Y., et al., *Atlas-guided tract reconstruction for automated and comprehensive examination of the white matter anatomy.* Neuroimage, 2010. **52**(4): p. 1289-301.

15. Tzourio-Mazoyer, N., et al., *Automated anatomical labeling of activations in SPM using a macroscopic anatomical parcellation of the MNI MRI single-subject brain.* Neuroimage, 2002. **15**(1): p. 273-89.

16. Hagmann, P., et al., *Mapping the structural core of human cerebral cortex.* PLoS Biol, 2008. **6**(7): p. e159.

17. Hagmann, P., et al., *Mapping Human Whole-Brain Structural Networks with Diffusion MRI.* PLoS One, 2007. **2**(7).

18. Bullmore, E. and O. Sporns, *Complex brain networks: graph theoretical analysis of structural and functional systems.* Nat Rev Neurosci, 2009. **10**(3): p. 186-98.

19. Watts, D.J. and S.H. Strogatz, *Collective dynamics of 'small-world' networks.* Nature, 1998. **393**(6684): p. 440-2.

20. Barabasi, A.L. and R. Albert, *Emergence of scaling in random networks.* Science, 1999. **286**(5439): p. 509-12.

21. Lo, C.Y., et al., *Diffusion tensor tractography reveals abnormal topological organization in structural cortical networks in Alzheimer's disease.* J Neurosci, 2010. **30**(50): p. 16876-85.

22. Mori, S., et al., *Stereotaxic white matter atlas based on diffusion tensor imaging in an ICBM template.* Neuroimage, 2008. **40**(2): p. 570-82.

23. Ceritoglu, C., et al., *Multi-contrast large deformation diffeomorphic metric mapping for diffusion tensor imaging.* Neuroimage, 2009. **47**(2): p. 618-627.

24. Beg, M.F., et al., *Computing Large Deformation Metric Mappings via Geodesic Flows of Diffeomorphisms.* International Journal of Computer Vision, 2005. **61**(2): p. 139-157.

25. Huang, H., et al., *Analysis of noise effects on DTI-based tractography using the brute-force and multi-ROI approach.* Magnetic Resonance in Medicine, 2004. **52**(3): p. 559-565.

26. Mori, S. and P.C.M. van Zijl, *Fiber tracking: principles and strategies - a technical review.* Nmr in Biomedicine, 2002. **15**(7-8): p. 468-480.

27. Miller, M.I., et al., *Collaborative computational anatomy: an MRI morphometry study of the human brain via diffeomorphic metric mapping.* Hum Brain Mapp, 2009. **30**(7): p. 2132-41.

28. Caan, M.W., et al., *Shaving diffusion tensor images in discriminant analysis: a study into schizophrenia.* Med Image Anal, 2006. **10**(6): p. 841-9.

29. Fan, Y., et al., *COMPARE: classification of morphological patterns using adaptive regional elements.* IEEE Trans Med Imaging, 2007. **26**(1): p. 93-105.

30. Ingalhalikar, M., et al., *Diffusion based abnormality markers of pathology: toward learned diagnostic prediction of ASD.* Neuroimage, 2011. **57**(3): p. 918-27.

31. Pereira, F., T. Mitchell, and M. Botvinick, *Machine learning classifiers and fMRI: a tutorial overview.* Neuroimage, 2009. **45**(1 Suppl): p. S199-209.

32. Cortes, C. and V. Vapnik, *Support-Vector Networks.* Machine Learning, 1995. **20**(3): p. 273-297.

33. Burges, C.J.C., *A tutorial on Support Vector Machines for pattern recognition.* Data Mining and Knowledge Discovery, 1998. **2**(2): p. 121-167.

34. Kloppel, S., et al., *Automatic classification of MR scans in Alzheimer's disease.* Brain, 2008. **131**(Pt 3): p. 681-9.

35. Wee, C.Y., et al., *Enriched white matter connectivity networks for accurate identification of MCI patients.* Neuroimage, 2011. **54**(3): p. 1812-22.

36. Cuingnet, R., et al., *Automatic classification of patients with Alzheimer's disease from structural MRI: a comparison of ten methods using the ADNI database.* Neuroimage, 2011. **56**(2): p. 766-81.

37. Cui, Y., et al., *Automated detection of amnestic mild cognitive impairment in community-dwelling elderly adults: A combined spatial atrophy and white matter alteration approach.* Neuroimage, 2012. **59**(2): p. 1209-1217.

38. Guyon, I., et al., *An introduction to variable and feature selection.* J. Mach. Learn. Res., 2003. **3**: p. 1157-1182.

39. Mckhann, G., et al., *Clinical-Diagnosis of Alzheimers-Disease - Report of the Nincds-Adrda Work Group under the Auspices of Department-of-Health-and-Human-Services Task-Force on Alzheimers-Disease.* Neurology, 1984. **34**(7): p. 939-944.

40. Mielke, M.M., et al., *Regionally-specific diffusion tensor imaging in mild cognitive impairment and Alzheimer's disease.* Neuroimage, 2009. **46**(1): p. 47-55.

41. Mohs, R.C., et al., *Development of cognitive instruments for use in clinical trials of antidementia drugs: Additions to the Alzheimer's disease assessment scale that broaden its scope.* Alzheimer Disease & Associated Disorders, 1997. **11**: p. S13-S21.

42. Folstein, M.F., S.E. Folstein, and P.R. Mchugh, *Mini-Mental State - Practical Method for Grading Cognitive State of Patients for Clinician.* Journal of Psychiatric Research, 1975. **12**(3): p. 189-198.

43. Wechsler, D., *Wechsler Memory Scale*. Third Edition ed. 1997, San Antonio, TX: The Psychological Corporation.

44. Pruessmann, K.P., et al., *SENSE: Sensitivity encoding for fast MRI.* Magnetic Resonance in Medicine, 1999. **42**(5): p. 952-962.

45. Jones, D.K., M.A. Horsfield, and A. Simmons, *Optimal strategies for measuring diffusion in anisotropic systems by magnetic resonance imaging.* Magnetic Resonance in Medicine, 1999. **42**(3): p. 515-525.

46. Jack, C.R., et al., *The Alzheimer's Disease Neuroimaging Initiative (ADNI): MRI methods.* Journal of Magnetic Resonance Imaging, 2008. **27**(4): p. 685-691.

47. Woods, R.P., et al., *Automated image registration: I. General methods and intrasubject, intramodality validation.* Journal of Computer Assisted Tomography, 1998. **22**(1): p. 139-152.

48. Huang, H., et al., *Correction of B0 susceptibility induced distortion in diffusion-weighted images using large-deformation diffeomorphic metric mapping.* Magnetic Resonance Imaging, 2008. **26**(9): p. 1294-1302.

49. Jiang, H.Y., et al., *DtiStudio: Resource program for diffusion tensor computation and fiber bundle tracking.* Computer Methods and Programs in Biomedicine, 2006. **81**(2): p. 106-116.

50. Guyon, I., *Feature extraction : foundations and applications*. Studies in fuzziness and soft computing,. 2006, Berlin ; New York: Springer-Verlag. xxiv, 778 p.

51. Chen, Y.-W. and C.-J. Lin, *Combining SVMs with Various Feature Selection Strategies*, in *Feature Extraction*, I. Guyon, et al., Editors. 2006, Springer Berlin Heidelberg. p. 315-324.

52. Cristianini, N. and J. Shawe-Taylor, *An introduction to support vector machines : and other kernel-based learning methods*. 2000, Cambridge ; New York: Cambridge University Press. xiii, 189 p.

53. Hsu, C.W., C.C. Chang, and C.J. Lin, *A practical guide to support vector classification*. 2003.

54. Chang, C.-C. and C.-J. Lin, *LIBSVM: A library for support vector machines.* ACM Trans. Intell. Syst. Technol., 2011. **2**(3): p. 1-27.

55. Golland, P. and B. Fischl, *Permutation tests for classification: towards statistical significance in image-based studies.* Inf Process Med Imaging, 2003. **18**: p. 330-41.

56. Ojala, M. and G.C. Garriga, *Permutation Tests for Studying Classifier Performance.* Journal of Machine Learning Research, 2010. **11**: p. 1833-1863.

57. Parker, G.J.M., H.A. Haroon, and C.A.M. Wheeler-Kingshott, *A framework for a streamline-based probabilistic index of connectivity (PICo) using a structural interpretation of MRI diffusion measurements.* Journal of Magnetic Resonance Imaging, 2003. **18**(2): p. 242-254.

58. Wang, J.H., et al., *Parcellation-Dependent Small-World Brain Functional Networks: A Resting-State fMRI Study.* Human Brain Mapping, 2009. **30**(5): p. 1511-1523.

59. Zalesky, A., et al., *Whole-brain anatomical networks: Does the choice of nodes matter?* Neuroimage, 2010. **50**(3): p. 970-983.

60. Faria, A.V., et al., *Atlas-based analysis of resting-state functional connectivity: Evaluation for reproducibility and multi-modal anatomy-function correlation studies.* Neuroimage, 2012. **61**(3): p. 613-621.

61. Eickhoff, S.B., et al., *A new SPM toolbox for combining probabilistic cytoarchitectonic maps and functional imaging data.* Neuroimage, 2005. **25**(4): p. 1325-1335.

62. Craddock, R.C., et al., *A whole brain fMRI atlas generated via spatially constrained spectral clustering.* Human Brain Mapping, 2012. **33**(8): p. 1914-1928.

Vita

KEGANG (Luke) HUA

EDUCATION

- **PH.D., Electrical and Computer Engineering**

  Johns Hopkins University

- **MS, Biomedical Engineering (Concurrent with Computer Science)**

  University of Kentucky

- **BS, Biomedical Engineering,**

  Jiangnan University, JiangSu, China

JOURNAL PUBLICATIONS:

Hua K, Zhang JY, Wakana S, Zhang WH, Huang H, Jiang HY, van Zijl PC, Mori S. Mapping of Cortical Areas Associated with Association Fibers of The Human Brain Using Diffusion Tensor Imaging and Tractography. Cereb. Cortex, 2009. 19(8):1889-95

Hua K, Zhang JY, Wakana S, Jiang HY, Reich DS, Calabresi PA, Pekar J, van Zijl PC, Mori S. *Tract Probability Maps in Stereotaxic Spaces: Analyses of White Matter Anatomy and Tract-Specific Quantification.* Neuroimage, 2008. **39**(1):336-47

Oishi K, Zilles K, Amunts K, Jiang H, Li X, Akhter K, **Hua K**, Woods R, Toga A, Pike B, Neto P, Evans A, Zhang JY, Huang H, Miller M, van Zijl PC, Mazziotta J, Mori S.

Human Brain White Matter Atlas: Identification and Assignment of Common Anatomical Structures in the Subcortical White Matter. Neuroimage, 2008 Nov 15;43(3):447-57

Mori S, Oishi K, Jiang H, Jiang L, Li X, Akhter K, **Hua K**, Faria A, Mahmood A, Woods R, Toga A, Pike B, Neto P, Evans A, Zhang JY, Huang H, Miller M, van Zijl PC, Mazziotta J. *Stereotaxic White Matter Atlas Based on Diffusion Tensor Imaging in an ICBM Template.* Neuroimage. 2008 Apr 1;**40**(2):570-82

Wakana S, Caprihan A, Panzenboeck MM, Fallon JH, Perry M, Gollub RL, **Hua K**, Zhang JY, Jiang HY, Dubey P, Blitz A, van Zijl PC, Mori S. *Reproducibility of Quantitative Tractography Methods Applied to Cerebral White Matter*. Neuroimage, 2007. **36**(3):630-44.

Hermoye L, Saint-Martin C, Cosnard G, Lee SK, Kim J, Nassogne MC, Menten R, Clapuyt P, Donohue PK, **Hua K**, Wakana S, Jiang H, van Zijl PC, Mori S. *Pediatric diffusion tensor imaging: normal database and observation of the white matter maturation in early childhood.* Neuroimage, 2006. **29**(2): p. 493-504.

CONFERENCE PROCEEDINGS:

Hua K, Oishi K, Jiang H, Li X, Zhang J, Akhter K, Miller MI, van Zijl PC, Albert M, Lyketsos C, Mielke M, Mori S. *Automated Tract-Specific Quantification Using Probabilistic Atlas Based on Large Deformation Diffeomorphic Metric Mapping and Its*

Application to Alzheimer's Disease. ISMRM 17th annual scientific meeting, Hawaii, USA, April 18-24, 2009

Hua K, Zhang JY, Wakana S, Huang H, Jiang HY, van Zijl PC, Mori S. *Cortical Mapping Inside Out: Mapping of Cortical Areas Associated with Specific White Matter Tracts Using Diffusion Tensor Imaging and Tractography.* ISMRM 14th annual scientific meeting, Seattle, Washington, USA, May 6-12, 2006

Hua K, Zhang JY, Wakana S, Jiang HY, van Zijl PC, Mori S. *Tract Probability Map in Stereotaxic Spaces and Analysis of Asymmetry.* ISMRM 14th annual scientific meeting, Seattle, Washington, USA, May 6-12, 2006

Hua K, Zhang JY, Jiang HY, Wakana S, van Zijl PC, Miller MI, Mori S. *Cortex mapping based on white matter connectivity using diffusion tensor imaging.* ISMRM 13th annual scientific meeting, South Beach, Miami, Florida, USA, May 7-13, 2005

Huang H, **Hua K**, Jiang H, van Zijl PC, Mori S. *Characterization and Correction of B0-Susceptibility Distortion in SENSE Single-Shot EPI-based DWI Using Manual Landmark Placement.* ISMRM 13th annual scientific meeting, South Beach, Miami, Florida, USA, May 7-13, 2005

Wakana S, Jiang HY, **Hua K**, Zhang JY, Dubey P, Blite A, van Zijl PC, Mori S. *Reproducible Protocol for Human White Matter Fiber Tracking and Quantitative*

Analysis of Their Status. ISMRM 13th annual scientific meeting, South Beach, Miami, Florida, USA, May 7-13, 2005

Kumagai M, Kim YH, Inoue N, Genda A, **Hua K**, Liong B, Koo T, Chao EYS. *3-D Dynamic Hip Contact Pressure Distribution In Daily Activities.* 2003 Summer Bioengineering Conference, Key Biscayne, FL June 25-29, 2003

Kim YH, Kang TS, Koo T, Liong B, **Hua K**, Inoue N, Chao EYS. *Simulation Of Tibial Osteotomy Execution Under Unilateral External Fixation.* 2003 Summer Bioengineering Conference, Key Biscayne, FL June 25-29, 2003

Koo I, Kim YH, Choi DB, **Hua K**, Lim J, Inoue N, Chao EYS. *Stiffness Analysis Of Dynafix External Fixator System.* 2003 Summer Bioengineering Conference, Key Biscayne, FL June 25-29, 2003

PATENT:

Mori S, Zhang JY, **Hua K** AUTOMATE WHITE MATTER PARCELLATION BASED ON DIFFUSION TENSOR IMAGING,